A Novel Multistatic SAR for Subsurface Imaging: Detection and Localization of Buried Pipelines and Leaks

by

Abdulrahman Aljurbua

A dissertation submitted in partial fulfillment
of the requirements for the degree of
Doctor of Philosophy
(Electrical and Computer Engineering)
in the University of Michigan
2022

Doctoral Committee:

Professor Kamal Sarabandi, Chair
Associate Professor Branko Kerkez
Professor Eric Michielssen
Associate Research Scientist Adib Y. Nashashibi
Professor Fawwaz Ulaby

Abdulrahman Aljurbua
aaljurbu@umich.edu
ORCID iD: 0000-0002-0529-0970

© Abdulrahman Aljurbua 2022

DEDICATION

To my high school biology teacher

مُحَمَّدْ الحبْس

who made me believe that I have what it takes to excel in higher education.

ACKNOWLEDGMENTS

I would like to start by expressing my sincerest gratitude and appreciation toward my PhD advisor Professor Kamal Sarabandi for his valuable mentorship and guidance, I feel very privileged to get the chance to work with a scientist of his caliber and I am deeply inspired by his seemingly endless knowledge, dedication and excitement about research. I would like also to thank Professor Fawwaz Ulaby for honoring me by being a member of my PhD committee and for his detailed review of my dissertation. I also would like to thank my committee members Dr. Adib Nashashibi, Professor Eric Michielssen and Professor Branko Kerkez for their insightful suggestions in the completion of this work.

I would like to express my appreciation to the wonderful people I met in the University of Michigan, starting with Dr. Behzad Yektakhah from whom I learned so much about radar imaging and clear scientific communication. I would like also to give special thanks to my seniors, Dr. Mostafa Zaky, Dr. Nasser Aldaghri, Dr. Faris Alsolamy, Dr. Abdulrahman Alaqeel, Dr. Maryam Salim, Dr. Navid Barani and Abdelhamid Nasr for all the tips they have given me on how to navigate the rough PhD road. I am very grateful for my wonderful friends in the US, Abdulhamed Alothaimen, Abdulaziz Alghamdi, Hamad Alotaibi, Abdulkarim Hariri, Zainulabideen Khalifa, Turki Bin Mohaya, Abdullah Alothman, Malik Almunif and Abdullah Alburadi for all the lovely memories we created together. I can not talk about friends without thinking of my dear friends back home, Sara, Mona, Hana, Lama , my dear cousin Abdulaziz and the lovely, frequent online conversations and correspondences we had easing the long, exhausting and lonely PhD journey, I am really grateful for that.

I feel deeply thankful and blessed to have my lovely family, my mother Khadijah and her never-ending sacrifices to provide for us, my wonderful siblings, Saleh, Omar, Sara, Anas and Rehab, my beloved friend Ibrahim and their unconditional love, support and belief in me. I would not be able to persevere in my PhD without thinking about thier love and pride

I would like to thank the Saudi Arabian Cultural Mission (SACM) for providing me a full-scholarship to finish my PhD and my employer King Abdulaziz City for Science and Technology (KACST) for funding the project on which this dissertation is based. I also would like to express my gratitude toward the staff of Silver Lake Recreation in Pinckney, Michigan for their welcoming attitude and accommodation during all the conducted experiments for this dissertation. Last but not least, I would like to acknowledge the most underrated factor of any accomplishment, that is utter, random, luck.

Abdulrahman Aljurbua

October 31, 2022

Ann Arbor

TABLE OF CONTENTS

DEDICATION ii

ACKNOWLEDGMENTS iii

LIST OF FIGURES viii

LIST OF TABLES xiv

LIST OF APPENDICES xv

LIST OF ACRONYMS xvi

ABSTRACT xvii

CHAPTER

1 Introduction 1

1.1 Background and Motivation 1
1.2 Related Work 6
1.2.1 Raw SAR Data Generation Using Simulation 6
1.2.2 Buried Pipelines Detection and Localization 7
1.2.3 Pipeline Leak Detection and Localization 13
1.2.4 Direct and Ground Reflection Signals Cancellation 16
1.3 Dissertation Overview 18

2 Fast Full-Wave Simulation Method for Multistatic SAR 23

2.1 Introduction 23
2.2 Fast Simulation Method 24
2.3 Simulation and Imaging Results 31
2.4 Conclusion 38

3 Detection and Localization of Buried Pipelines 39

3.1 Introduction 39
3.2 Pipeline Detection and Localization Algorithm 40
3.2.1 Forward Problem 40
3.2.2 Inversion Algorithm 41
3.3 Analytical and Numerical Analysis 44

3.3.1 The Accuracy of Far-field Assumption . . . 45
3.3.2 Conical Phase Front Assumption . . . 48
3.3.3 Single Medium Assumption . . . 49
3.3.4 Soil Dielectric Estimation . . . 50
3.3.5 Time Domain Responses for Different Tx-Rx Arrangements . 53
3.4 Simulation and Measurement Results . . . 55
3.4.1 Simulation . . . 55
3.4.2 Measurements . . . 56
3.5 Conclusion . . . 64

4 Detection and Localization of Closely-Spaced Buried Pipelines . . 65

4.1 Introduction . . . 65
4.2 Closely-Spaced Buried Pipelines Detection and Localization Algorithm 66
4.2.1 Forward Scattering of A Single Pipeline . . . 67
4.2.2 Forward Scattering of Multiple Pipelines . . . 70
4.2.3 Inversion Algorithms . . . 71
4.3 Numerical Analysis . . . 73
4.3.1 Uniform Medium Assumption . . . 75
4.3.2 Efficacy of The First Order Scattering Assumption . . . 76
4.4 Performance Evaluation for The inversion Algorithms . . . 80
4.4.1 Performance Evaluation Using Full-Wave Simulation . . . 80
4.4.2 Performance Evaluation Including Tx-Rx Signal Leakage . . 81
4.4.3 Performance Evaluation Including Noise . . . 84
4.4.4 Performance Evaluation Using Experimental Data . . . 85
4.5 Conclusion . . . 90

5 Detection and Localization of Buried Pipeline Leaks . . . 91

5.1 Introduction . . . 91
5.2 Leak Detection and Localization Technique . . . 92
5.2.1 Received Signal Model . . . 92
5.2.2 GPOF Method . . . 95
5.2.3 BP Algorithm for Leak Detection . . . 96
5.2.4 Radar Resolution and Rx Array Configuration . . . 98
5.3 Oil leak Model . . . 99
5.3.1 Modeling Leak Spread . . . 99
5.3.2 Oil Contaminated Soil Permittivity . . . 102
5.4 Simulation and Measurement Results . . . 106
5.4.1 Simulation . . . 106
5.4.2 Measurements . . . 112
5.5 Conclusion . . . 118

6 A Method for Signal Leakage Cancellation in Multistatic SAR . . 119

6.1 Introduction . . . 119
6.2 Signal Leakage Elimination . . . 120
6.3 Imaging Algorithm . . . 123

6.4 Simulation and Measurement Results 124
6.4.1 Simulation 125
6.4.2 Measurements 128
6.5 Conclusion 133

7 Conclusions and Future Work 134

7.1 Summary and Conclusions 134
7.2 Dissertation Contributions 135
7.2.1 Development of Fast Full-Wave Simulation Method for Deeply Buried Targets in 3D Multistatic SAR 136
7.2.2 Development of a Dynamic Focusing Algorithm for Buried Pipelines Detection and Localization in 3D Multistatic SAR 136
7.2.3 Development of an Optimization-Based Inversion Algorithm for Closely-Spaced Buried Pipelines Detection and Localization in 3D Multistatic SAR 137
7.2.4 Development of Buried Pipelines Leaks Detection and Localization Technique in 3D Multistatic SAR 138
7.2.5 Development of Array Null-synthesis Based Tx-Rx Signal Leakage Suppression Technique for 3D Multistatic SAR . . . 139
7.3 Future Work 139
7.3.1 Applying Machine Learning Based Classifiers to the Fast Full-Wave Simulation Data 139
7.3.2 Generalizing the Pipelines Detection and Localization Algorithm for Stratified Media 140
7.3.3 Detection and Localization of Closely-Spaced Pipelines Leaks 140

APPENDICES 141

BIBLIOGRAPHY 150

LIST OF FIGURES

FIGURE

1.1 (a) GPR use in land mine detection for security missions (courtesy of [1]) (b) GPR use in infrastructure maintenance (courtesy of [2]) (c) GPR use in archaeological explorations (courtesy of [3]). 2
1.2 (a) Traditional GPR system that uses a monostatic transceiver (Tx-Rx) and records the target signal as a function of range (B-Scan) along a uniform grid (courtesy of [4]) (b) the newly suggested multistatic subsurface SAR that has a fixed Tx and a moving Rx that samples the target signal at arbitrary spatial locations (courtesy of [5]). 4
1.3 Side view of multistatic subsurface SAR scattering mechanism of a point target with a single scattering phase center for all Rx positions (a) and a pipeline with unique scattering phase center for each Rx position (b). . 12
1.4 Dissertation flow chart. 22

2.1 Multistatic subsurface SAR imaging system. 24
2.2 The original (a) and the equivalent (b) problems. 25
2.3 First scenario with Rx excited (a) and second scenario with Rx in receiving mode (b). 26
2.4 Tx above half-space, the scattered field from the targets can be computed along a hypothetical plane. Then, the scattered electric ($\boldsymbol{E_T}$) and magnetic ($\boldsymbol{H_T}$) fields can be converted to equivalent currents representing the scattered field due to all the dielectric and metallic targets below the plane. 30
2.5 Parallel geometry ENVELOP antenna array used in simulation. 32
2.6 The real (a) and imaginary (b) parts of V_{oc} due to a PEC sphere obtained using the conventional (brute force) and the proposed (fast) methods. . . 33
2.7 The real (a) and imaginary (b) parts of V_{oc} due to a PEC Cylinder obtained using the conventional (brute force) and the proposed (fast) methods. 34
2.8 PEC Landmine geometry (a), the real (b) and imaginary (c) parts of V_{oc} due to the Landmine obtained using the conventional (brute force) and the proposed (fast) methods. 36
2.9 Complex PEC target geometry (a), the real (b) and imaginary (c) parts of V_{oc} due to the Complex target obtained using the conventional (brute force) and the proposed (fast) methods. 37
2.10 Two-planes cut of a reconstructed 3-D image of a 15 cm radius PEC sphere buried at 1 meter depth Tx is indicated by triangle and sampling points are indicated by circles. 38

3.1 Side view of multistatic subsurface SAR scattering mechanism of a point target with a single scattering phase center for all Rx (a) and a pipeline with unique scattering phase center for each Rx (b). 40
3.2 (a) Top view of the coordinates showing the pipe and the subsurface SAR system and (b) the primed local coordinates along the pipe axis and (c) a colored illustration of the pipeline scattering mechanism as seen by the primed coordinates. 43
3.3 Algorithm for pipelines detection and localization in multistatic subsurface SAR. 45
3.4 Mean value of the phase introduced by the antenna over the main lobe at various distances. 47
3.5 Phase error due to far-field approximation of Hankel function. 48
3.6 Mean phase error across all Rxs and frequencies Vs pipe diameter. . . . 50
3.7 Mean value of the scattered field phase error between the forward model and FEKO simulation data. 51
3.8 Parameters estimation versus background permittivity error. 52
3.9 Peak of the search space Vs error in real background permittivity. . . . 53
3.10 Rx paths used (a) and the resulting range as a function of Rx positions (b), the pipe is buried at 0.5 m depth. 54
3.11 The search space of the algorithm when applied to simulation data of a metallic and dielectric pipes. 56
3.12 Measurement place near Silver Lake in Pinckney, Michigan. 57
3.13 (a) The ring resonator used at different depths (b) the resulting sand dielectric profile. 57
3.14 The VNA based multistatic subsurface SAR Setup A used in the two experiments. 58
3.15 The VNA based multistatic subsurface SAR Setup B used in the two experiments. Compared to Setup A in Fig. 3.14, there is a metallic plate inserted between the Tx and Rx to reduce Tx-Rx coupling and ground reflections. 59
3.16 The buried pipes used in the experiment. 60
3.17 The magnitude of the search space obtained from the metallic and PVC pipes measurements using Setup A. A strong peak is shown near zero depth indicating the direct Tx-Rx coupling signal. 60
3.18 The magnitude of the search space obtained from the metallic pipe measurements using Setup B. The use of the metallic plate repressed the direct coupling and ground reflections allowing for the detection and localization of the buried metallic pipe. 62
3.19 The magnitude of the search space obtained from the water filled PVC pipe measurements using Setup B. The use of the metallic plate repressed the direct coupling and ground reflections allowing for the detection and localization of the buried water filled PVC pipe. 63

4.1 Multistatic subsurface SAR system. There is a fixed transmitter (Tx) illuminating the underground and a moving receiver (Rx) that samples the scattered field around the Tx. It is noted that unlike point targets that have a fixed scattering phase center, pipelines have dynamic scattering phase centers that depend on the Rx position relative to the Tx. 66
4.2 Top view of the coordinate systems (the global and the primed one along one of the pipes) and the subsurface SAR configuration. The pipes have the same depth h_c with varying displacements determined by the spacing s. For vertically buried pipes the displacement will be d_c and the depths will be varying. Displacement direction is from the Tx location to a specific pipes' center. 67
4.3 The primed local coordinates along an arbitrary pipe p of depth h and displacement d from the Tx. Only two cones are shown for illustration. Each Rx has a unique cone and SPC (the cone tip). The same applies for the other pipes. 68
4.4 Basic phase compensation (focusing) algorithm for finding single pipeline or widely spaced pipelines parameters proposed in Chapter 3. 72
4.5 Novel dynamic grid search algorithm for finding multiple closely spaced pipelines parameters. 74
4.6 Received voltage values for different Rx locations obtained by full-wave simulation as well as using the forward model in (4.3) where the radiation patterns are calculated one time for a single medium - FM - and another time for half-space scenario - FM (Half-space). The data are for two 10 cm diameter PEC pipelines with $d_1 = -0.5m, d_2 = -1m, \alpha = 0, h_c = -1m$ (See Fig. 4.2). 77
4.7 Received voltage values for different Rx locations obtained by full-wave simulation as well as using the forward model (4.3) at 300 MHz frequency. The data are for four PEC pipelines with $d_1 = -0.13m, d_2 = -0.44m, d_3 = -0.75m, d_4 = -1.06m, \alpha = 0, h_c = -0.8m$ (See Fig. 4.2) inside loam medium. 78
4.8 Received voltage values for different Rx locations obtained by full-wave simulation as well as using the forward model (4.3) at 300 MHz frequency. The data are for 3 dielectric pipelines arranged vertically with $h_1 = -0.75m, h_2 = -1m, h_3 = -1.25m, \alpha = 0, d_c = -1.25m$ (See Fig. 4.2) inside loam. 79
4.9 An h-d cut of the Search space of Algorithm I (Fig. 4.4) (a) and the detection results of Algorithm II (Fig. 4.5) (b) when applied to full-wave simulation data. The data is for four PEC pipelines of 21.9-cm diameter and 10-cm edge-to-edge spacing inside Loam medium from Table 4.1. . . 81
4.10 An h-d cut of the Search space of Algorithm I (Fig. 4.4) (a) and the detection results of Algorithm II (Fig. 4.5) (b) when applied to full-wave simulation data. The data is for three water-filled PVC pipelines of 10.2-cm diameter and 15-cm edge-to-edge spacing inside Loam medium from Table 4.1. 82

4.11 Overall detection rates across the 20 pipelines cases in Table 4.2 buried in Sand medium (Table 4.1) for varying levels of leakage signal. 83
4.12 Overall detection rates across the 20 pipelines cases in Table 4.2 buried in sand and clay media (Table 4.1) for varying levels of noise. 85
4.13 Experiments location near Silver Lake, Pinckney, MI, USA along with the ring resonator probe and the resulting dielectric profile 86
4.14 Buried metallic (a) and water-filled PVC (b) pipelines used in the two experiments 86
4.15 VNA-based multistatic SAR setup for both experiments. The Rx is moved along a square of 3.6-m edge length, collecting S_{21} data at 40 different locations while the Tx is fixed in the middle. 87
4.16 An h-d cut (at the actual α) of the Search space of Algorithm I (Fig. 4.4) (a) and the detection results of Algorithm II (Fig. 4.5) (b) when applied to metallic pipelines experiment (Fig. 4.14a). The data is for 2 metallic pipelines of 5cm diameter and $d_1 = -0.225, d_2 = 0.025, \alpha = 0, h_c = -0.35$ (See Fig. 4.2). 88
4.17 An h-d cut of the Search space of Algorithm I (Fig. 4.4) (a) and the detection results of Algorithm II (Fig. 4.5) (b) when applied to water-filled PVC pipelines experiment (Fig. 4.14b). The data is for 2 water-filled PVC pipelines of 9cm diameter and $d_1 = -0.245, d_2 = 0.045, \alpha = 0, h_c = -0.35$ (See Fig. 4.2). 89

5.1 Multi-static subsurface SAR imaging arrangement, the pipeline signal (soild) takes a different path compared to the leak signal (dashed). . . . 92
5.2 Perspective view for the scattering scene with the coordinate system along the pipeline used for analysis. The incident wave making an angle θ_i with the pipeline axis generates a scattered field cone with θ_i as generating angle. 93
5.3 Steps followed in applying BP algorithm and obtaining the leak indicator. 97
5.4 Rx array configuration with the volumetric resolution cell along the three orthogonal directions. 98
5.5 A cross-sectional 2D cut visual illustration for the actual 3D structure of soil pores model. The equivalent circuit extends in 3D but only a side view of the circuit is shown for better visibility. 101
5.6 Leak samples generated using the outlined procedure. 103
5.7 (a) Oil samples used (b) ring resonator probe mounted on sand-oil mixture for dielectric measurements. 104
5.8 Measured and fitted ($\alpha = 0.045$) dielectric constant for sand mixed with (a) light and (b) medium oil. 105
5.9 Real (a) and imaginary (b) parts of measured and fitted ($\alpha = 0.045$) dielectric constant for 10% wet sand mixed with light oil. 105
5.10 Tx-Rx scans arrangement used in all simulations, three scans are obtained where the Tx is advanced by 0.5 m relative the the previous scan while the Rx path is a circle centered around the Tx. 107

5.11 Percentage error between pipe signal obtained by simulating pipe alone and GPOF estimated pipe signal obtained from the pipe simulation in the presence of the leak, the frequency is fixed at 350 MHz and the Tx-Rx arrangement is that of the Scan1 in Fig 5.10. 108
5.12 Overall leak indicator for (a) oil leak out of a 10 cm diameter PEC pipe in sand and (b) oil leak out of a 5 cm diameter oil-filled PVC pipe in clay. The leak detection technique is applied to simulation data for the pipe alone (dashed) and the pipe in addition to the leak (solid) to provide proper comparison. 110
5.13 Log scale plot of FOM versus different cases of simulation. 112
5.14 (a) Experiments location near Silver Lake (b) plastic containers filled with water saturated sand to represent the leak. 113
5.15 (a) Ring resonator measuring sand and leak dielectric (b) dielectric profile of sand along with the leak. 113
5.16 The buried pipes and the leak used in the experiments. 114
5.17 Experimental setup for VNA based bi-static subsurface SAR used in all experiments. 114
5.18 Tx-Rx scans arrangement used in all experiments. The Tx is fixed in positions 1,2 and 3 for scans 1,2 and 3 respectively while Rx samples are on the same position for each scan. 116
5.19 Overall leak indicator obtain from Scans 1, 2 and 3 for (a) the metallic pipe and (b) the water filled PVC pipe. The leak detection technique is applied to measured data for the pipe alone (dashed) and the pipe in addition to the leak (solid) to provide proper comparison. 117

6.1 Multi-static subsurface SAR used in this work. The direct and ground reflections (solid lines) have similar paths compared to the target signal (dashed) since the Tx and Rx are very close to ground. 120
6.2 Top view of the three configurations used in simulation along with the buried spheres, configuration 1 is at the center of the coordinates while configuration 2 and 3 are shifted 40 and 100 cm respectively along the x direction. It should be noted that the spheres are fixed with respect to the coordinates. 125
6.3 Time domain signals for Rx location numbers 26 and 27 in Configuration 1 in Fig. 6.2 along with the time signal for the array constructed using (6.2). Direct and ground reflections signals are cancelled while the spheres signals are enhanced. 126
6.4 An X-Z (Y=0) cut of the reconstructed 3D image with and without null-steering using Configuration1 in Fig. 6.2 only. The actual spheres locations are indicated by black circles. dB scale is used and both images are normalized to the same maximum. 127
6.5 An X-Z (Y=0) cut of the reconstructed 3D image with and without null-steering using all the configurations in Fig. 6.2. The actual spheres locations are indicated by black circles. dB scale is used and both images are normalized to the same maximum. 128

6.6 Experiments location near Silver Lake (a) and the Tx-Rx arrangement used in the experiment along with the buried pipe (b). 129
6.7 The VNA based subsurface bistatic SAR setup used in the experiment along with the buried metallic pipeline. 130
6.8 Time domain signals for Rx location numbers 11 and 12 in Fig. 6.6b along with the time signal for the array constructed using (6.2). Direct and ground reflections signals are cancelled while the pipe signal is enhanced. 131
6.9 An h-d cut out of the 3D pipeline parameters search space where α is fixed at 90 degrees. The actual pipe parameters are indicated by a black circle. dB scale is used and both searches are normalized to the same maximum. 132

A.1 Main MATLAB code for focusing based pipelines detection and localisation algorithm where Get-Path function is defined at the end. 142

B.1 Main function for optimization based closely-Spaced pipelines detection and localization algorithm. 144
B.2 Associated functions to the main function for optimization based closely-Spaced pipelines detection and localization algorithm. 145
B.3 Associated functions to the main function for optimization based closely-Spaced pipelines detection and localization algorithm. 146

C.1 Main function for signal leakage cancellation and imaging algorithm, the array imaging function is shown in Fig. C.2. 148
C.2 Imaging function for signal leakage cancellation and imaging algorithm. The BP imaging code is adopted from [5] and modified to incorporate array null-steering. 149

LIST OF TABLES

TABLE

4.1 Soil Media Used in Simulations and Numerical Analysis 75
4.2 Benchmark Performance Cases 83
4.3 Computation Time for Algorithm II at Different Search Resolutions . . . 88

5.1 Oil Samples Used in Dielectric Measurements. 103
5.2 Soil Samples Used in All Simulations 107
5.3 The Various Cases Considered in Simulation 111

LIST OF APPENDICES

A MATLAB Code for Focusing Based Pipelines Detection and Localization Algorithm 141

B MATLAB Code for Optimization Based Closely-Spaced Pipelines Detection and Localization Algorithm 143

C MATLAB Code for Signal Leakage Cancellation 147

LIST OF ACRONYMS

BP Back Projection

EM Electromagnetic

FM Forward model

FOM Figure of Merit

GPOF Generalized Pencil Of Function

GPR Ground penetrating radar

PEC Perfect Electric Conductor

PVC Polyvinyl chloride

Rx Receiver

SAR Synthetic Aperture Radar

SPC Scattering Phase Center

Tx Transmitter

VNA Vector Network Analyzer

ABSTRACT

Ground penetrating radar (GPR) is a valuable tool widely used for many tasks in infrastructure development and maintenance, mining and archaeology, as well as in support of construction industries. As opposed to the traditional monostatic GPR system, a multistatic subsurface synthetic aperture radar (SAR) system uses a fixed transmitter to illuminate the underground and a moving receiver to sample the scattered signals around the transmitter which provides major advantages in subsurface imaging and target detection. The most notable advantages are the faster acquisition time, the improved lateral resolution, and the higher gain resulting from coherent processing. Notwithstanding, the complexity of such a subsurface SAR system introduces new challenges which this dissertation aims to address.

The first challenge is encountered in data generation using simulation. In order to evaluate the imaging performance of the subsurface SAR system, a new full-wave simulation is needed each time the receiver moves to a different position, which makes the number of simulations grow with the number of the required samples. By replacing the target with its equivalent current distribution and invoking the reciprocity theorem, this dissertation proposes a method that reduces the number of simulations required by a factor of $N/2$, where N is the number of samples required to form the SAR image.

Another challenge is encountered in regard to the detection and localization of buried pipelines. Since pipelines have an extended geometry, the scattering phase center on a pipeline moves as a function of the transmitter and receiver positions. This renders traditional focusing algorithms, such as the back-projection algorithm,

not applicable for such a target as the scattering phase center does not appear as a fixed point with respect to the positions of the radar's transmitter and receiver. Exploiting the theoretical knowledge for pipeline scattering behavior, this dissertation develops a dynamic focusing algorithm tailored to pipelines, thereby leading to their detection and localization in multistatic SAR mode.

Building on the focusing algorithm for pipelines, which has limited range and cross-range resolutions, the dissertation provides a more general treatment for detection and localization of multiple closely-spaced pipelines. This is accomplished by developing a 3D forward scattering model for multiple pipelines, then inverting the model by minimizing the misfit between measured signals and the forward scattering model using a dynamic grid search algorithm.

The third challenge addressed in the dissertation is related to the detection and localization of buried-pipeline leaks when using the multistatic SAR mode. Due to the multiple scattering-phase-centers phenomena exhibited by pipelines, the scattered signal from the pipelines tends to overwhelm the signal scattered from the leak, making leak detection a difficult task. Utilizing the pipeline detection and localization algorithm devised earlier, the dissertation suggests a technique to identify and eliminate the pipeline contribution of the radar response, leading to better performance in leak detection.

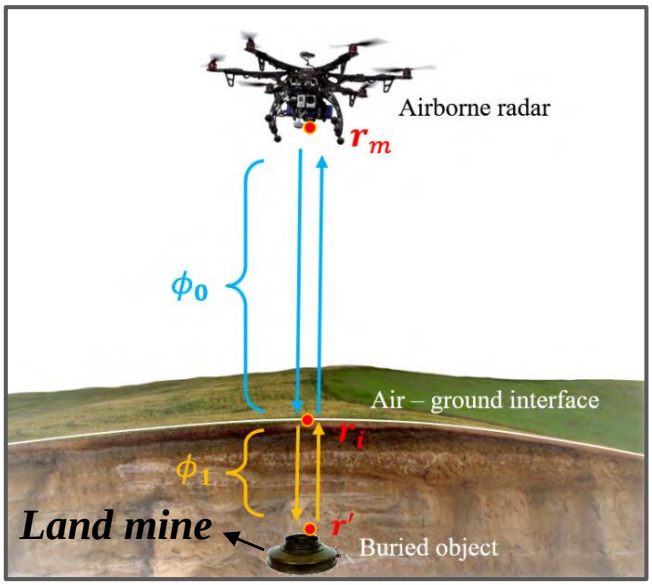
Lastly, the problem of the direct signal leakage from the transmitter to the receiver in multistatic SAR is discussed. The leakage signal tends to be much stronger than the signals from buried targets. By incorporating array null-synthesis in the SAR processing stage, the dissertation proposes a method in which a null is created along the direction of the transmitter, thereby nulling out the leakage signal. This allows the signals from the buried objects to be detected, which ultimately leads to better imaging performance.

CHAPTER 1

Introduction

1.1 Background and Motivation

The fact that electromagnetic (EM) waves can penetrate into the ground medium and reflect back when they encounter inhomogeneities makes them suitable to utilize in sensing the underground. Current technology that uses EM waves to detect and identify underground constituents, such as buried objects, tunnels and soil layers, is referred to as ground penetrating radar (GPR). GPRs are widely used for many tasks in infrastructure development and maintenance (Fig. 1.1b), security missions (Fig. 1.1a), and archaeology (Fig. 1.1c), as well as in support of the construction industries. As outlined in [6], the history of using EM waves to detect and identify underground features goes back to the 1950s when the first attempt was made by the author of [7] to estimate the depth of a water table beneath the ground surface. During the 1960s, applications to GPR systems extended to include investigation of soil and rocks as well as coal mine explorations. By the 1980s, GPR systems were used in utility mapping and roads investigations. In the latter half of the 1990s, the rapid advancement in computers paved the way for 3D EM numerical simulations that allowed researchers to understand wave propagation through the ground and its interaction with underground constituents. Moreover, digital data acquisition, along with the high processing rates of computers, enabled the emergence of 3D GPR sys-



(a)



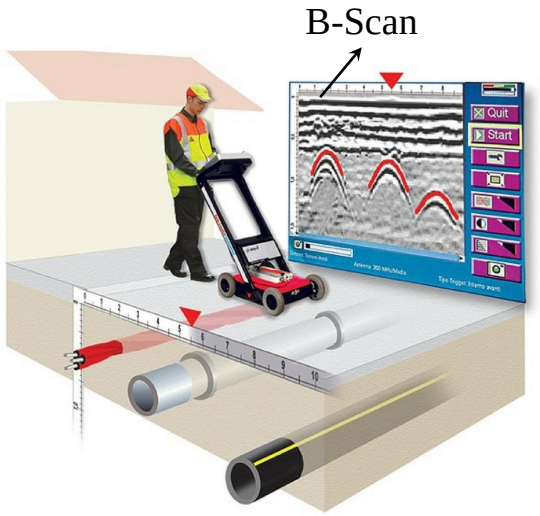
(b)



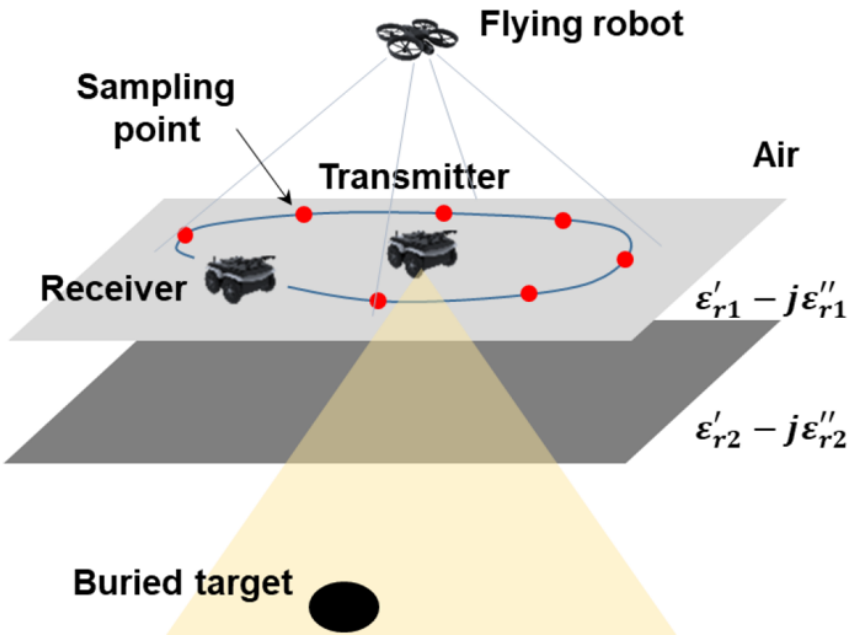
(c)

Figure 1.1: (a) GPR use in land mine detection for security missions (courtesy of [1]) (b) GPR use in infrastructure maintenance (courtesy of [2]) (c) GPR use in archaeological explorations (courtesy of [3]).

tems. Nowadays, GPR is considered a well-developed technology that is used widely by engineers and scientists [8]. Current research efforts in GPR development are focused on signal processing and target classification, as well as various applications in civil engineering [9]. The research effort pertinent to this dissertation is the multistatic subsurface synthetic aperture radar (SAR) suggested earlier in [10] and then improved further in [5]. In contrast to traditional GPR systems that have a monostatic receiver that scans the ground on a uniform grid by moving along straight lines and displaying the recorded signal as a function of range and position (See Fig. 1.2a) [11, 12, 13, 14], the multistatic subsurface SAR proposed in [5] has a fixed transmitter (Tx) that illuminates the underground targets and a moving receiver (Rx) that samples the scattered field as it moves along an arbitrarily defined path as illustrated in Fig. 1.2b. After that, all the collected signals are processed coherently to provide a high resolution image of the underground. Such a multistatic configuration with arbitrary Rx path combined with coherent SAR co-processing, provides three major advantages over traditional GPR systems. First, the acquisition time is much faster since the Rx moves and collects the scattered field at specific points, compared to the uniform grid samples that take a much longer time to acquire without necessarily providing new and independent information at each point, compared to an arbitrary path such as a circular one. Second, the lateral (cross-range) resolution is enhanced significantly since SAR co-processing creates a large effective aperture which plays an essential role in determining lateral resolution of the radar system. Finally, the high processing gain that results from coherent processing of all the signals at different locations and frequencies allows the multistatic SAR to detect and image deep targets compared to the traditional monostatic GPR system where the signals from deep targets might be too attenuated to detect. Nevertheless, the complexity of the multistatic subsurface SAR introduces new challenges. Two of the encountered challenges are the data generation using simulation and the leakage (direct) signal from



(a)



(b)

Figure 1.2: (a) Traditional GPR system that uses a monostatic transceiver (Tx-Rx) and records the target signal as a function of range (B-Scan) along a uniform grid (courtesy of [4]) (b) the newly suggested multistatic subsurface SAR that has a fixed Tx and a moving Rx that samples the target signal at arbitrary spatial locations (courtesy of [5]).

the Tx to the Rx. Data generation is a challenge because the multistatic configuration requires a new simulation each time the Rx moves to a new position around the Tx, making the required number of simulations grow with the number of Rx samples. The leakage-signal challenge arises due to the separation of the Tx and Rx antennas compared to the monostatic arrangement where the same antenna is used for both transmitting and receiving. Because the direct signal travels through air, it suffers less attenuation compared to the signal from the target buried in typically lossy soil making detection more difficult. Two other problems that are encountered are associated with trying to detect pipelines and their leaks using the multistatic radar configuration. Since pipelines are extended objects, their scattering mechanism is different from that of point targets. In the multistatic mode, point targets have fixed scattering phase centers that scatter the incident wave to all receivers. On the other hand, extended targets like pipelines have a dynamic scattering phase center that keeps changing depending on the position of the receiver relative to the transmitter. This unique scattering mechanism renders typical imaging algorithms, such as the back-projection (BP) algorithm [15, 16, 17, 18] not useful because such algorithms assume a point-like scattering mechanism when finding the required phase at each receiver location to focus the collected signals and reconstruct the image. Moreover, this multiple dynamic scattering phase centers phenomena for pipelines creates another challenge when trying to detect pipeline leaks using multistatic SAR. Basically, due to the multiple scattering phase centers, the scattered pipeline signal tends to overwhelm the signal scattered from the leak which usually is more localized, making leak detection a difficult task. The objective of this dissertation is to provide techniques and algorithms to address these four challenges associated with using the multistatic subsurface SAR configuration (long simulation time, direct Tx-Rx coupling, unique pipelines scattering mechanism, and weak leak signal compared to pipeline signal). Before proceeding to the dissertation overview, the next section

discusses related work published in the literature concerning these challenges.

1.2 Related Work

1.2.1 Raw SAR Data Generation Using Simulation

As discussed earlier, one of the challenges faced when adopting the multistatic SAR configuration is the data generation process because subsurface SAR requires a new simulation each time the Rx is moved to a new location. Efforts in the literature dealing with the data-generation problem can be categorized into two broad categories. One category addresses the problem by reducing its complexity and hence reducing the simulation time. An example of this is the work in [19] where an air borne SAR raw data generation problem for forest canopies is treated by generating a forest canopy model, then replacing the actual canopy in the model with a fewer number of virtual scatterers whose collective scattering behavior is equivalent to that of the actual canopy, within some tolerable error. This procedure reduces the simulation time by a factor of M, where M is the number of canopies that are replaced by a single virtual scatterer. Another example is the work in [20] which hybridizes geometric optics (GO) with full-wave simulation. Basically, the electrically large scene is divided into electrically large scatteres that are treatable by GO using a ray tracing simulator and the remaining scatteres that are not electrically large are simulated with full-wave simulation for better accuracy.

The other category addressing the SAR raw data generation problem is focused on improving the computational efficiency rather than reducing the problem complexity. In [21], the authors suggest a parallel computation scheme wherein several graphics processing units (GPUs) are used to simultaneously simulate different parts of the simulated scene, then the results from each GPU are combined at the end to obtain the SAR raw data. A similar parallel strategy was pursued in [22] where the raw

SAR data generation problem for a very complex space-borne SAR system operating in multiple modes is addressed by utilizing several GPUs and combining them in a computationally efficient manner to produce raw SAR data for the different radar modes of operations.

These research efforts that reduce the problem's complexity or improve the computation efficiency are mainly targeting air borne and space-borne SAR systems that cover large areas of land. In the case of the subsurface SAR, the scene under consideration is much smaller and the focus of the problem is on finding the received signal at the receiver terminals in a way that includes the effect of soil on the receiver performance. Here, the data generation problem becomes about reducing the number of simulations required because a single simulation for a receiver, a transmitter, and a target does not take much time, but challenges arise when one tries to generate the data for a large number of Rx positions using a brute force numerical approach (i.e., repeating the full-wave simulation for all Rx positions) wherein the approach becomes impractical. When facing a computational burden of this nature, the reciprocity theorem can be used to simplify many radiation and scattering problems. One example is reported in [23] where reciprocity was used to calculate the far-field antenna gain and pattern from the near field measurements. In another work [24], the authors used reciprocity to simplify the calculation of multiple scattering from a target above a rough surface in a monostatic setting. Adopting similar reciprocity-based reasoning can reduce the number of simulations significantly, as will be shown in Chapter 2 of this dissertation.

1.2.2 Buried Pipelines Detection and Localization

When surveying the literature related to pipeline detection using ground penetrating radar, one finds that the majority of the published work deals with the problem by assuming a traditional GPR scheme like the one shown in Fig. 1.2a. In such a scheme,

the transceiver moves along a straight line over the pipeline and the radar response is plotted as a function of position and range. The position-range plot (called B-Scan) generates a hyperbola shape indicating the presence of a buried object.

One category of research in the GPR literature is concerned with performing simulations of the scattering mechanism for buried pipelines in order to understand the nature of the radar response, so as to help GPR operators interpret the results they obtain. One example is found in [25] where a finite-difference-time-domain (FDTD) simulator is used to examine the scattering mechanisms for three different scenarios with various soil layers and pipelines numbers. Similar works are found in [26] where a fast parallel computational method based on FDTD is proposed and multiple cases of buried PVC and metallic pipelines are investigated. In [27], an FDTD simulator is used to generate data for multiple pipelines buried in concrete and the simulations are validated by comparing them to measured data in a controlled experiment. Another study is reported in [28] where an FDTD-based simulation is carried out for a buried plastic pipeline and a buried plastic pipeline with its surrounding trench to study how the scattering mechanism of the pipeline is influenced by the soil-filled trench.

Another category of research in the GPR literature is focused on interpreting the hyperbolas found in the radar B-Scan and trying to relate the buried pipeline parameters, such as location and radius of the buried pipe, to the hyperbola parameters measured by the radar. One example is found in [29] where the authors proposed a method to estimate the radius of a buried pipeline and the soil dielectric constant simultaneously by using nonlinear least-squares fitting between the GPR B-Scan and a general hyperbola function that depends on the pipeline radius and the soil dielectric constant. Another example is the work in [30] where a combination of two methods is used. At first an electric field localization method is used in which metallic plates are positioned on the ground and the capacitive coupling between them is measured as they are moved over the pipeline, and when a change in the coupling

is observed the lateral pipeline location is estimated. After that, the depth and the radius of the buried pipeline is estimated by interpreting the hyperbolas found in the B-scan. There are also studies [31, 32] that use the Hough transform to interpret the hyperbolas found in the B-Scan. In the Hough transform, a hyperbola function with different parameters is proposed, then a search is done in a parameter space (the set of all possible hyperbolas fitting the B-Scan). After that, the peaks in this parameter search space are correlated with the unknown pipeline parameters, such as its diameter and location.

Continuing in the hyperbolas characterization works, researchers have also been using optimization and machine-learning based techniques to allow for more robust and automatic detection and characterization of the B-Scan hyperbolas. In [33], a fully automated scheme is proposed where the B-scans are processed in three stages. At first, clustering is done by comparing the adjacent columns in the B-scan to identify possible hyperbolas. This is followed by a neural-network based classifier that classifies the hyperbolas into false alarm and actual ones. Finally, the last stage consists of fitting the detected hyperbolas to extract the pipeline-related parameters (depth, diameter, soil dielectric). A similar work is found in [34] where a new B-Scan hyperbola identification approach is proposed wherein the B-Scan are processed for edge detection first, then a drop-flow algorithm is applied to the detected edges to identify which set of edges constitutes an actual hyperbola. The drop flow mimics the movement of a water drop as it descends along the detected edges allowing for automatic identification of the hyperbolas. Other studies like the ones reported in [35, 36, 37, 38] focus on using neural-network classifiers to directly detect the hyperbolas found in the B-Scan. In [39], an automatic detection is achieved by casting the hyperbola search as an optimization problem that is solved using a genetic-algorithm based optimization to detect the pipeline locations, while in [40] a fuzzy clustering algorithm is proposed to solve the same problem.

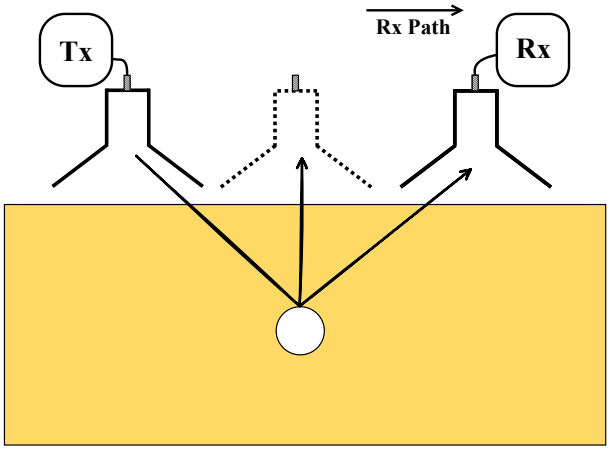
Aside from the simulations and the B-Scans identification categories, there are 2D tomographic shape reconstruction studies like the ones found in [41, 42, 43]. In these type of approaches, a Green's function based full-wave scattering model is simplified to get a linear system of equations. The solution to these equations provides a 2-D contrast function representing the dielectric profile of the underground or the current distribution on the surface of the scatterers. Such a contrast function enables the pipeline edges to be separated from the background, leading to pipeline detection and localization.

The main drawback in the hyperbola recognition and shape reconstruction approaches is that they operate in a 2-D space. This means that they require either a monostatic radar configuration (like the one in Fig. 1.2a) or a special multistatic configuration in which the transmitter and receiver locations are confined to a straight line. This is not an issue in many situations where the pipeline signal is strong enough and the detection is achieved readily. However, in situations where the pipeline is made of plastic or has a small diameter, or where the pipeline is buried in a very lossy medium, the scattered signal from the pipeline might be too weak to detect. To deal with this weak signal problem, a multistatic radar configuration with arbitrary receiver locations like the one shown in Fig. 1.2b might be used to collect the pipeline signal over multiple incidence and scattering angles. After that, the collected signals are processed coherently with a back-projection (BP) algorithm [15, 16, 17, 18] to significantly improve the detection. The basic idea of BP relies on the fact that the scattered field signals are emitted from a single point on the scatterer in all directions and the phase shift due to the signals' bistatic path can be calculated. Compensating for the phase shifts due to each possible spatial target location at each receiver and summing the compensated signals coherently leads to peaks at the scatterers' locations. The BP algorithm works fine for point targets because their scattering phase centers are fixed with respect to the receiver's positions. This is not the case for

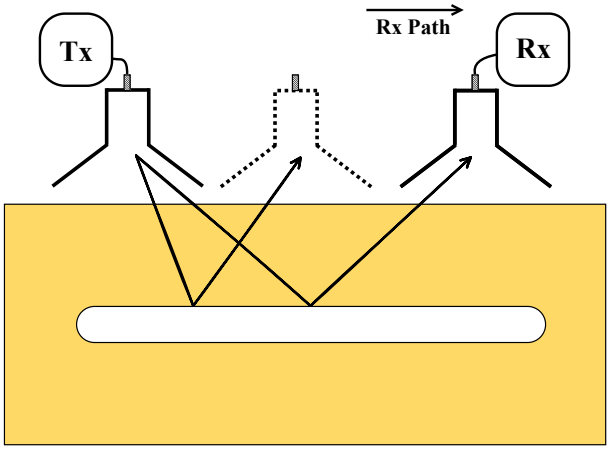
pipelines, as they are extended scatteres for which the scattering phase centers vary based on the location of the receiver and transmitter, as shown in Fig. 1.3. This multiple scattering phase centers problem can be addressed by taking into account the unique scattering mechanism for pipelines and devising a new algorithm for phase compensation (focusing) as will be discussed in Chapter 3 of this dissertation.

Relying on phase compensation alone (focusing) comes with its well-known disadvantage, namely the limited range and cross-range resolutions for detection and localization of the buried pipelines. To improve that, an optimization based approach may be considered wherein a forward scattering model is constructed and a cost function that compares the received signal with the forward model is defined. This is followed by optimizing the cost function, leading to the detection and localization of the buried objects. Such an approach is adopted in various works in the literature that use different froward models and optimization algorithms.

One category of research approaches the detection problem by considering a 2D scenario in which the forward model is obtained by operating a half-space Green's function on an unknown current distribution, resulting from the contrast between the buried object and the background medium. After that, optimization is carried out to optimize an objective function defined as the misfit between the measured data and the forward model. When the minimization process converges, the unknown contrast is determined and detection and localization are achieved. One example is the work in [44] where particle swarm optimization (PSO) is used to minimize the objective function. Another example is the research reported in [45] where evolutionary programming is adopted to minimize the objective function for large scale subsurface profiling. In [46], the authors used optimization-based sparse reconstruction to detect and localize electrically small buried objects. A similar, yet slightly different, work is found in [47] where a pulse based radar is used for detection of pipelines hidden inside a wall. In this work, the forward model is a simple one relying on the time



(a)



(b)

Figure 1.3: Side view of multistatic subsurface SAR scattering mechanism of a point target with a single scattering phase center for all Rx positions (a) and a pipeline with unique scattering phase center for each Rx position (b).

delay of the returned pulses and the optimization is carried out to separate the delays corresponding to the wall pulse from the delays of the pipelines pulses. Another category of studies in GPR follows a full-wave inversion approach [48, 49, 50, 51]. In this approach, the wave equation is solved by discretizing the subsurface domain into a collection of cells, leading to a system of equations that is solved by matrix inversion. The optimization is then carried out to minimize an objective function representing the difference between the measured and predicted solutions. When convergence is reached, the dielectric profile of the subsurface is revealed. Such optimization approaches are either 2D in nature or computationally burdensome because the full-wave forward model needs to be evaluated multiple times until convergence is reached.

Building on the algorithm for tracking the scattering phase centers developed in Chapter 3, the dissertation considers the general problem of scattering by multiple buried pipelines and develops a computationally efficient 3D forward scattering model for a multistatic subsurface SAR configuration. The forward model is validated by comparing it to full-wave solutions. After that, a dynamic grid-search based inversion algorithm is introduced to minimize the misfit between the forward model and the measured radar response leading to detection and localization of closely-spaced buried pipelines, as will be shown later in Chapter 4.

1.2.3 Pipeline Leak Detection and Localization

When dealing with the problem of leak detection using radars, the reported studies in the literature fall into different categories. The first category is concerned with very large leaks, or what is usually referred to as spills, that cover large area of land and can be detected by air borne radars from a long distance. In this category, one finds some studies like the one reported in [52] wherein a helicopter-borne GPR system is used to measure the radar response of a large oil spill under snow, suggesting that

a simple observation of the scattered field amplitude using GPR can be sufficient to detect such an oil spill because the spill leads to a reduction in the amplitude of the scattered field as the spill acts like a matching layer between the ice or soil substrate with snow packs above it. Other more elaborate studies like the ones reported in [53, 54, 55] use a fully polarimetric air borne SAR system to observe oil spills in the sea as well as to distinguish metallic man-made objects in the sea that are introduced when an accidental spill happens. The high deviation of the co-polarized channels phase difference is shown to indicate the presence of an oil spill while the correlation between the co-polarization and cross-polarization responses is shown to distinguish man-made from naturally occurring objects.

The other radar-based leak-detection category is concerned with pipeline leaks that occur in soil, which tends to be more localized compared to the large leaks in the sea or ice. Here, GPR B-Scans and tomographic reconstruction techniques are usually used, just like in the pipeline detection case. To offer more details, here are some examples of B-Scan based investigations. In [56], an FDTD simulation is performed for a buried pipeline with the leak modeled as a stratified soil medium where dielectric constant decreases as a function of distance away from the pipeline, resembling the gradual wetting nature of the leak. Both vertical and horizontal polarizations are used and the detection is accomplished by interpreting the disturbances found in the hyperbolas in the B-Scans. In [57], experimental studies are carried out for water leaks out of metallic as well as PVC pipelines. The experiments were conducted in a controlled-laboratory setting where water is injected in multiple stages and the GPR B-Scans are collected and analyzed at each stage to examine how detectable the leak is compared to the pipeline response alone before the leak is injected. Another experimental study is found in [58] where a scaled down model of a leaking pipeline is studied in a laboratory setting. The water leak was replaced with a plastic box filled with methanol which was shown to have electrical properties similar to those of

wet sand. The study which used B-Scan images with and without the leak concluded that disturbances on the B-Scan hyperbola shapes can be interpreted as a pipeline leakage. Another more realistic experimental work was reported in [59]. Here, a realistic experimental setting was conducted for 3 buried pipelines, two of which have a leak besides them (one leak consists of wet sand and the other is a larger leak consisting of water besides wet sand). The experiments used the usual GPR that acquires B-Scans and the disturbances in the resulting B-Scan hyperbolas are interpreted as leaks. Continuing on B-Scan based research, the authors in [60] used a hybrid method in which an electric wire sensitive to the dielectric constant of the surrounding medium is buried with the pipeline to provide a signal when the water leak gets mixed with the sand. This signal gives an estimated location for the leak. After that, a monastic traditional GPR is run over the pipeline, and the hyperbolas in the B-Scan are used to analyze the change in the dielectric constant of the sand before and after the start of the leak, offering better resolution compared to the electric wire alone.

Moving on to the tomographic reconstruction-based approaches, we find a couple of research studies [61, 62] in which the scattered field is written in terms of a Green's function that includes the response of the soil and the pipeline. After that, the model is inverted to obtain the impedance contrast (taking into account the pipeline presence using Green's function) and any deviation from the uniform impedance is considered to be a leak. A similar more comprehensive work is found in [63] where a comparison is performed between the traditional GPR B-Scans approach and the traditional tomographic reconstruction approach, as well as the new approach for tomographic reconstruction that includes the pipeline response incorporated into a Green's function. It is found that including the pipeline response in the formulation helps in making the contrast due to the leak more apparent. Also, among the tomographic reconstruction approaches is the more simple but coarse-resolution solution in

[64] where the resistivity profile of the underground is measured using a collection of voltage and current probes that are attached to the ground. After that, the measured voltage is used to estimate the resistivity profile of the underground from which the leak location is estimated by comparing it to the non-leaking pipeline case.

Besides the B-Scan and tomographic reconstruction, a more robust approach is the 2D monostatic back-projection (BP) based synthetic aperture radar (SAR) leak detection technique [65] in which the radar moves along the pipeline and BP is used to process all the signals coherently and construct 2D images from which the leak is detected. All the aforementioned approaches share a common drawback, namely their 2D nature, which involves scanning the leak from a limited number of angles. Moreover, with the exception of [61, 62, 63], all the other approaches do not address the fact that the scattered signal from the pipeline tends to dominate over the leak signal, thereby hindering the radar's ability to detect pipeline leaks. To acquire more information from the leak, a 3D BP can be used with a multistatic-SAR arrangement like the one illustrated in Fig. 1.2b. Under the multistatic configuration, not only is the leak observed from more angles, but at the same time the pipeline response problem becomes more apparent as the pipeline will scatter the incident wave in many directions. However, the unique scattering mechanism of a pipeline compared to localized point-like scatteres under the multistatic configuration (See Fig. 1.3) allows for the possibility of identifying the pipeline part of the radar response and eliminating it to improve leak detectability, as will be shown in Chapter 5 of this dissertation.

1.2.4 Direct and Ground Reflection Signals Cancellation

As discussed earlier, signal leakage (i.e., the direct signal from the transmitter and the ground reflection signal) constitutes a major barrier for the detection of buried objects, as they tend to be larger than the signals from the buried targets. There

are several techniques to deal with this problem in the literature, the most basic and notable among them are time gating and background subtraction. In time gating, the buried target signal is isolated from the direct and ground reflections as it arrives later in time. Time gating does not work well for shallowly buried targets and when the transmitted signal has side-lobes in time as in these cases, the buried target and direct signals overlap in time. Background subtraction is quite restrictive as it assumes a fixed offset between the transmitter and the receiver and sometimes it requires measuring the background signal under controlled settings where it is known apriori that no target is there. More advanced processing techniques exist in the literature, so we will illustrate with some examples of such techniques.

One of the techniques is the shift and scale technique suggested in [66]. The basic idea of this technique is to estimate the background signal by taking the average value across all the radar sampling points. After that, at each sampling point, a minimization procedure is performed wherein the estimated background signal is scaled and shifted in time to fit the background signal at that particular sampling position. A similar work can be found in [67] where instead of taking the average value to obtain an estimate for an initial background signal, a controlled experiment is carried out at one sampling position without the target to get an initial estimate for the background signal, which then gets shifted and scaled appropriately at other sampling positions.

Another technique is the $k - f$ filtering technique [68, 69]. In this technique, the received signal in position and time is transformed into angular and spatial frequency domains. After that, the background signal can be identified in the new domain due to its unique direction of arrival compared to the buried-target signals. This allows for filtering the background in the frequency and angular frequency domains, then transforming back to the original domains to obtain clearer buried-target signals.

Moreover, there are matrix decomposition based techniques [70, 71]. In theses techniques, the received signals at different times and positions are placed in a ma-

trix form. After that, an optimization is carried out to decompose the received signal matrix into a low-rank matrix that corresponds to the background and a separate sparse matrix that corresponds to the buried targets. Besides the matrix decomposition, another class of techniques that is relatively simpler and requires less processing is the use of a differential bistatic radar configuration where either two receivers [72] or two transmitters [73] are arranged in a symmetric way with respect to ground such that the direct and ground reflection components of the transmitted or the received signals interfere destructively, thereby canceling their effect. Those techniques require perfect phase and amplitude matching and depending on the distance and position, nulls can occur in undesired directions.

Building on an earlier work in [74] where the author used differential SAR to eliminate the strong glare in the backscatter from walls for a through-wall monostatic imaging system, a more general null-synthesis approach might be pursued to cancel the direct and ground reflection signals in a multistatic SAR system (like the one in Fig. 1.2b), as will be discussed in Chapter 6 this dissertation.

1.3 Dissertation Overview

This dissertation presents algorithms and techniques for the detection and localization of buried pipelines and buried pipeline leaks using a multistatic subsurface synthetic aperture radar (SAR). This entails developing a forward model to describe the scattering behaviour of the pipeline and the leaks for a multistatic radar configuration, as well as inversion techniques suited for those models. Furthermore, additional issues arising from the multistatic configuration are needed to be addressed which include the time-consuming data generation using simulation as well as the influence of the direct Tx-Rx coupling and the ground reflection (leakage) signal. A block diagram summarizing the different components of the dissertation is shown in

Fig. 1.4. The following is an overview of each of the dissertation's chapters.

Chapter 2 discusses a hybrid analytical and numerical simulation method for time-efficient calculation of the induced voltage across a receiver's terminals due multistatic scattering from deeply buried objects. The method works by calculating the current distribution on the surface of the target due to illumination from the transmitter. After that, the receiver is used as a transmitter and its field is calculated everywhere in the lower half space. Then the reciprocity theorem is used to relate the induced voltage across the receiver terminals due to the current distribution. By doing that, the method reduces the overall simulation time by a factor of $N/2$, where N is the number of Rx samples needed to form the SAR image. The chapter concludes by validating the method by comparing it with the results based on brute-force full-wave simulation method (which requires N simulations), as well as by image reconstruction from the dataset generated by the method.

In Chapter 3, a focusing algorithm designed specifically for buried-pipelines detection and localization in the multistatic SAR mode is discussed. The chapter starts with the analytic scattering solution of a pipeline and goes on to discuss how the phase propagation behavior for pipelines is different from that of point-like scatterers to motivate the use of the new focusing algorithm instead of the more common BP algorithm. After that, the algorithm steps are described in detail and the inherent assumptions made during the derivation are justified with numerical examples. This is followed by validating the algorithm on a full-wave simulation data. Utilizing a pair of antennas deigned for GPR applications, along with a portable vector network analyzer (VNA), the chapter ends with an experimental demonstration of the algorithm performance in a realistic lossy sand environment.

Chapter 4 considers the general problem of detection of multiple closely-spaced buried pipelines (as opposed to the single-pipeline case and the widely-spaced pipelines) in multistatic subsurface SAR. The chapter builds on the Chapter 3 algorithm for tracking scattering phase centers for pipelines and proceeds to develop a forward scattering model for multiple buried pipelines that takes into account the propagation phase as well as the signal attenuation due to propagation and medium losses. After that, an objective function representing the misfit between the measured data and the predicted response based on the forward model is minimized using a dynamic grid-search based algorithm leading to improvements in detection and localization in both range and cross-range resolutions. The performance of the approach is evaluated on full-wave simulation data, in the presence of signal leakage and noise, as well as using experimental measurements.

Chapter 5 discusses a technique to improve pipeline-leaks detectability when using a 3D multistatic subsurface synthetic aperture radar. Building on the forward and inverse scattering of the pipelines discussed in in Chapter 3, the chapter explains how to decompose the received signal and distinguish the pipeline contribution from the leak contribution to the signal. When the pipeline signal is identified and eliminated the detactability of the leak is improved significantly. To verify that, the chapter provides a physics-based model for oil leak spread inside the soil as well as a measured permittivity profile for oil-sand mixtures. The oil spread model and the measured permittivity are then used in a full-wave simulation model to simulate oil leaks from plastic as well as metallic pipes buried in various kinds of soil mixtures. After that, the leak detection technique is tested on the full-wave simulation data as well as on a VNA-based multistatic radar experimental setting where an oil leak is replaced with a water leak.

In Chapter 6, a method is presented for cancelling the effect of the direct Tx-Rx signal leakage and the ground reflection signal in multistatic SAR. The method works by co-processing adjacent Rx samples as a two-element array that has a null along the direction of the transmitter so as to cancel the direct and ground reflection signals. The chapter discusses the technique in detail and the potential problems in imaging that arise when creating nulls in specific directions. After that, the technique's effectiveness is tested on full-wave simulation data as well as measured data using a VNA based multistatic radar experimental setting.

Chapter 7 provides a summary, conclusions and recommendations for future work.

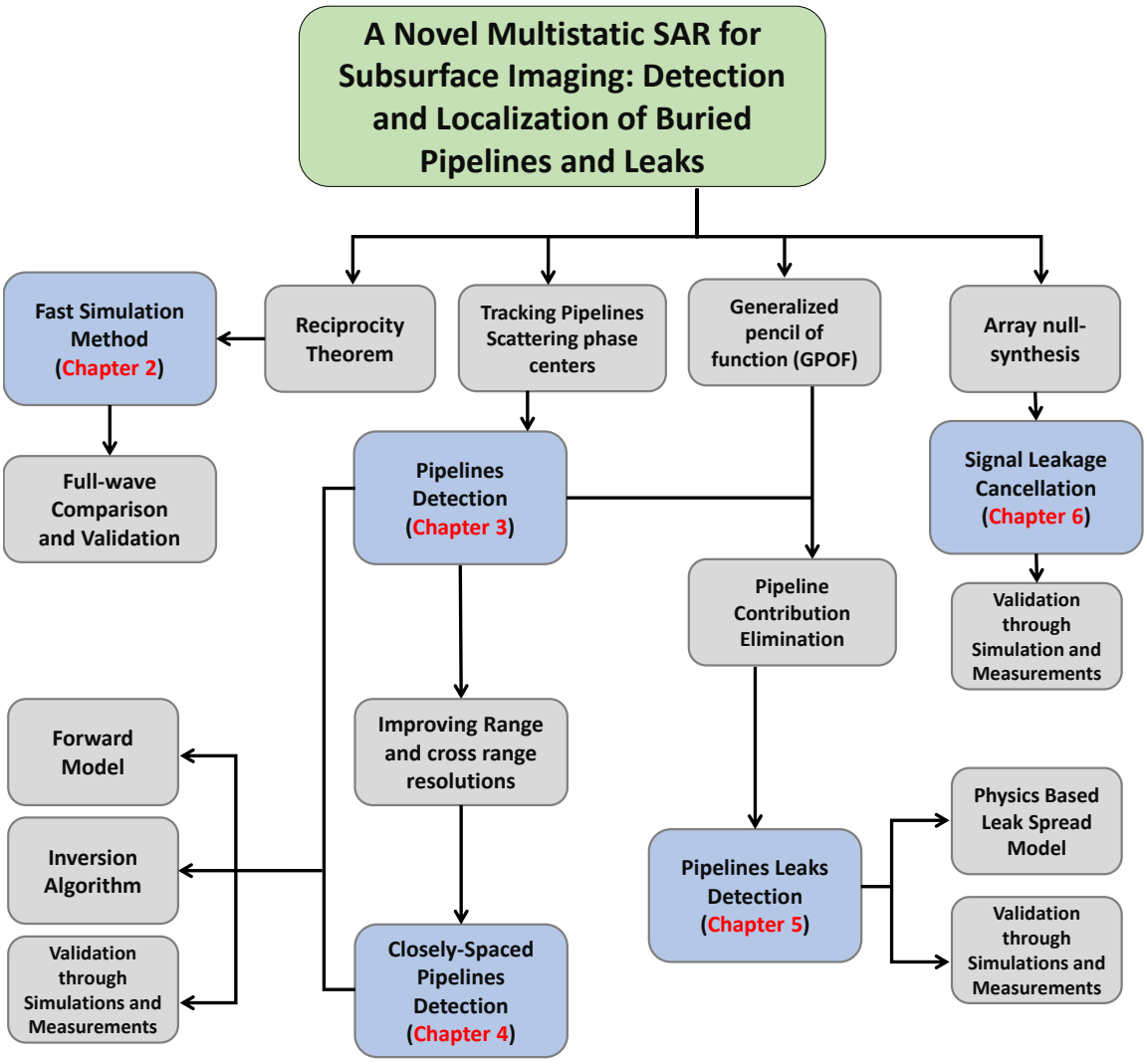


Figure 1.4: Dissertation flow chart.

CHAPTER 2

Fast Full-Wave Simulation Method for Multistatic SAR

2.1 Introduction

Full-wave simulation for a multistatic SAR configuration can be a time consuming process. This is because SAR requires taking multiple samples of the scattered field at different spatial locations using a moving Rx. The brute-force approach is to carry out a new simulation each time the Rx moves to a new position, making the simulation time grow with the number of required samples. This challenge can be addressed by dividing the simulation process into two stages. In the first stage, the Tx illuminates the underground, inducing a current distribution on the surface of the buried targets. The second stage consists of the induced current radiating the scattered field causing an induced voltage across the Rx terminals that is measured and used in SAR image reconstruction. Following this reasoning, the repeated simulations required by SAR can be reduced to two simulations only, one to calculate the induced current distribution on the target and another is to calculate the induced Rx voltage due to such a current distribution. This chapter illustrates this approach and compares it with the brute-force approach, leading to significant reduction in simulation time. The chapter considers the multistatic subsurface SAR system depicted in Fig. 2.1, and utilizes the reciprocity theorem to develop a fast full-wave simulation method for

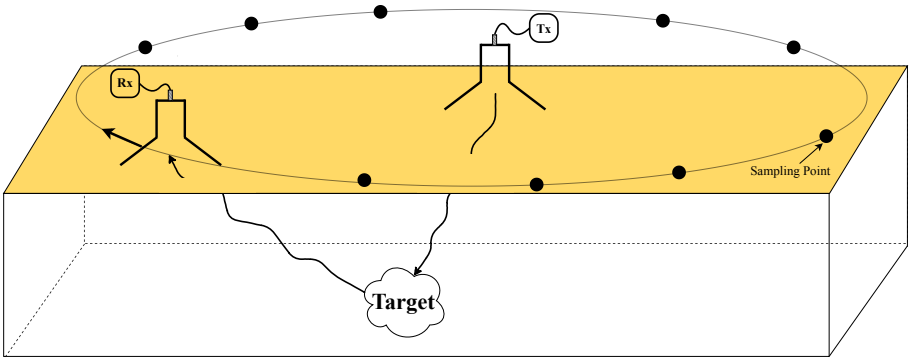


Figure 2.1: Multistatic subsurface SAR imaging system.

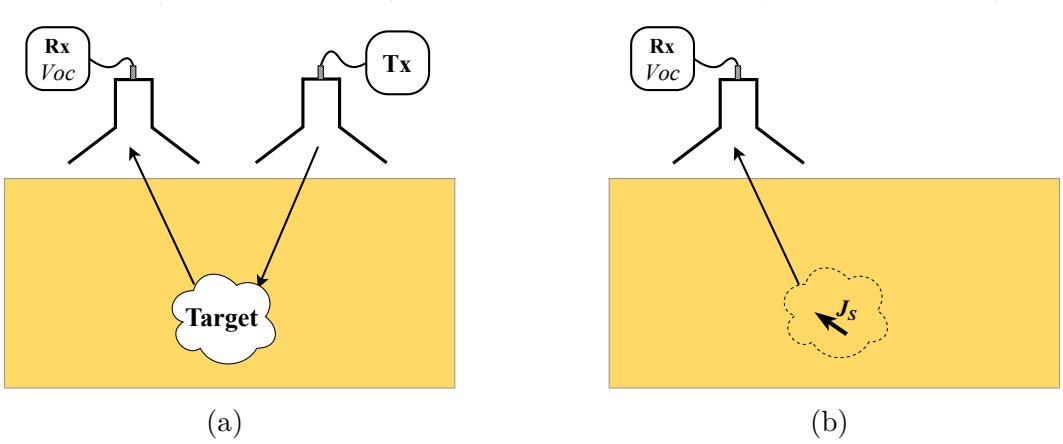
calculating the induced voltage across the Rx terminals due to scattering from targets buried deeply in the soil. The following sections explain the concept in detail and provide simulation and imaging results that demonstrate the efficacy of the proposed approach.

2.2 Fast Simulation Method

To better illustrate the difference in data generation between the proposed (fast) and the conventional (brute-force) simulation methods, a standard back-projection imaging scheme is considered for analysis. To form a 3-D bistatic SAR image in such a scheme, the following formula [75] can be used at each imaging point p in 3-D space:

$$Image\ (p) = \sum_{m=1}^{M} \sum_{n=1}^{N} V_{oc}^{nm} e^{j(k_{Air}^{m} R_{Air}^{n} + k_{Soil}^{m} R_{Soil}^{n})} \tag{2.1}$$

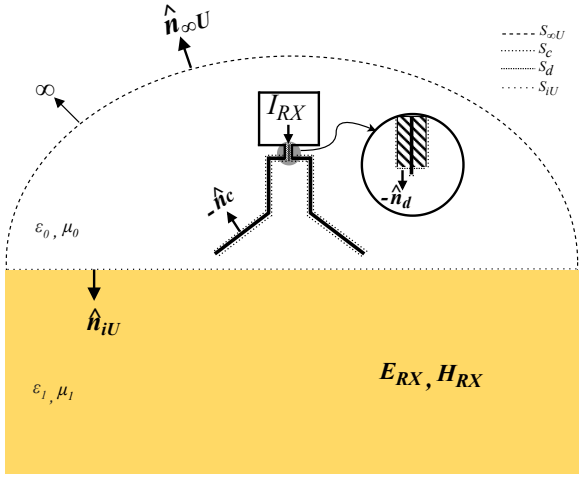
where V_{oc}^{nm} is the open circuit voltage across the Rx terminals at the m^{th} frequency and n^{th} sampling point, k_{Air}^{m} and R_{air} are the propagation constant at the m^{th} frequency and the signal path-length in air, respectively. The same is true for soil. To find all V_{oc}^{nm} values in the brute-force approach, a full-wave frequency sweep over M frequencies for (Tx, Rx at position n, target inside soil) is carried out N times for



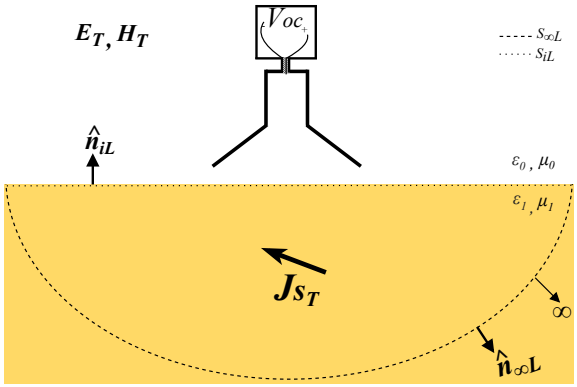
(a) (b)

Figure 2.2: The original (a) and the equivalent (b) problems.

N different Rx positions. Moving to the fast method, let us consider the problem of finding V_{oc} for one Rx location more carefully. The problem is shown in Fig. 2.2a. There is a transmitter (Tx) sending a signal to an arbitrary metallic target buried in the soil, a surface current distribution $\boldsymbol{J_s}$ is formed on the surface of the target, radiating a scattered signal to a receiver (Rx) that converts the signal into an open circuit voltage V_{oc} across its terminals. If the target is deep enough, the Tx-Rx direct signal as well as the signal reflected from the air-soil interface can be ignored as they can be time gated in real measurements. It should be noted that this assumption may not be warranted in situations where the effect of the tail of the direct and ground reflection signals is as strong as the target reflected signal, which sets some limitation to the applicability of the method. Moreover, it is assumed that the current distribution is a result of Tx-Target signal only and is not affected by the presence of the Rx antenna. That is, the higher order signals, such as the Tx-Rx-Target are negligible. The same is true for V_{oc} where it is caused by the Target-Rx signal only excluding the Target-Tx-Rx and other higher order signals. Hence, if we perform a full-wave frequency sweep with Tx and target only and save the surface current $\boldsymbol{J_s}$, the configuration of Fig. 2.2b can be considered to find V_{oc} across Rx terminals. To go about finding V_{oc}, the reciprocity theorem [76], which relates fields and currents in two different



(a)



(b)

Figure 2.3: First scenario with Rx excited (a) and second scenario with Rx in receiving mode (b).

scenarios, is utilized. The first scenario (Fig. 2.3a) is Rx excited by a current source I_{RX}, resulting in an electric field $\boldsymbol{E_{Rx}}$ radiated inside the soil. The second scenario is an impressed surface current distribution $\boldsymbol{J_{s_T}}$ inside the soil, resulting in V_{oc} across Rx terminals (Fig. 2.3b). As indicated by the surfaces in Fig. 2.3, the scene can be divided into two homogeneous regions. The first region is a source-free homogeneous air covered by a surface that goes around Rx without containing it while the second is a homogeneous soil that includes sources. If we denote the quantities of the first and

second scenarios by the subscripts Rx and T respectively, the reciprocity relations for the source-free air region become:

$$\oiint_{S_{\infty U}+S_c+S_d+S_{iU}} (\boldsymbol{E}_{\boldsymbol{Rx}}^{\boldsymbol{Air}} \times \boldsymbol{H}_{\boldsymbol{T}}^{\boldsymbol{Air}} - \boldsymbol{E}_{\boldsymbol{T}}^{\boldsymbol{Air}} \times \boldsymbol{H}_{\boldsymbol{Rx}}^{\boldsymbol{Air}}) \cdot \hat{\boldsymbol{n}}\, ds = 0 \tag{2.2}$$

The surface $S_{\infty U}$ is a hemisphere with an infinite radius and a surface normal directed radially, which means the fields at such a surface are far-field TEM waves. The component of (2.2) over $S_{\infty U}$ vanishes as shown below:

$$\begin{aligned} &\iint_{S_{\infty U}} (\boldsymbol{E}_{\boldsymbol{Rx}}^{\boldsymbol{Air}} \times \boldsymbol{H}_{\boldsymbol{T}}^{\boldsymbol{Air}} - \boldsymbol{E}_{\boldsymbol{T}}^{\boldsymbol{Air}} \times \boldsymbol{H}_{\boldsymbol{Rx}}^{\boldsymbol{Air}}) \cdot \hat{\boldsymbol{n}_{\infty \boldsymbol{U}}}\, ds \\ &= \iint_{S_{\infty U}} (\boldsymbol{E}_{\boldsymbol{Rx}}^{\boldsymbol{Air}} \cdot (\boldsymbol{H}_{\boldsymbol{T}}^{\boldsymbol{Air}} \times \hat{\boldsymbol{n}_{\infty \boldsymbol{U}}}) - \boldsymbol{E}_{\boldsymbol{T}}^{\boldsymbol{Air}} \cdot (\boldsymbol{H}_{\boldsymbol{Rx}}^{\boldsymbol{Air}} \times \hat{\boldsymbol{n}_{\infty \boldsymbol{U}}}))\, ds \\ &= \iint_{S_{\infty U}} (\boldsymbol{E}_{\boldsymbol{Rx}}^{\boldsymbol{Air}} \cdot (\frac{1}{\eta}\boldsymbol{E}_{\boldsymbol{T}}^{\boldsymbol{Air}}) - \boldsymbol{E}_{\boldsymbol{T}}^{\boldsymbol{Air}} \cdot (\frac{1}{\eta}\boldsymbol{E}_{\boldsymbol{Rx}}^{\boldsymbol{Air}}))\, ds = 0 \end{aligned} \tag{2.3}$$

The other surface S_c goes around a conducting material (the antenna surface along with its shielded source). Therefore, there is no surface tangential electric field which leads to:

$$\begin{aligned} &\iint_{S_c} (\boldsymbol{E}_{\boldsymbol{Rx}}^{\boldsymbol{Air}} \times \boldsymbol{H}_{\boldsymbol{T}}^{\boldsymbol{Air}} - \boldsymbol{E}_{\boldsymbol{T}}^{\boldsymbol{Air}} \times \boldsymbol{H}_{\boldsymbol{Rx}}^{\boldsymbol{Air}}) \cdot \hat{\boldsymbol{n}}_{\boldsymbol{c}}\, ds \\ &= \iint_{S_c} (\boldsymbol{H}_{\boldsymbol{T}}^{\boldsymbol{Air}} \cdot (\hat{\boldsymbol{n}}_{\boldsymbol{c}} \times \boldsymbol{E}_{\boldsymbol{Rx}}^{\boldsymbol{Air}}) - \boldsymbol{H}_{\boldsymbol{Rx}}^{\boldsymbol{Air}} \cdot (\hat{\boldsymbol{n}}_{\boldsymbol{c}} \times \boldsymbol{E}_{\boldsymbol{T}}^{\boldsymbol{Air}}))\, ds \\ &= \iint_{S_c} (\boldsymbol{H}_{\boldsymbol{T}}^{\boldsymbol{Air}} \cdot (\boldsymbol{0}) - \boldsymbol{H}_{\boldsymbol{Rx}}^{\boldsymbol{Air}} \cdot (\boldsymbol{0}))\, ds = 0 \end{aligned} \tag{2.4}$$

Contribution from surface S_d that goes around the dielectric material inside the coaxial cable is evaluated while keeping in mind that there is no current running through the cable in the receiving mode, and therefore no tangential H-field. Moreover, in the

standard coaxial cable the dominant mode is a TEM mode whose E-field is given by [77]:

$$\boldsymbol{E_T^{Air}} = \frac{V_{oc}}{\rho \ln \frac{b}{a}} \hat{\boldsymbol{\rho}} \tag{2.5}$$

Applying Ampere's law around the inner conductor in transmitting mode gives:

$$\boldsymbol{H_{Rx}^{Air}} = \frac{I_{Rx}}{2\pi\rho} \hat{\boldsymbol{\phi}} \tag{2.6}$$

With the above expressions, the surface integral of S_d becomes:

$$\begin{aligned}
&\iint_{S_d} (\boldsymbol{E_{Rx}^{Air}} \times \boldsymbol{H_T^{Air}} - \boldsymbol{E_T^{Air}} \times \boldsymbol{H_{Rx}^{Air}}) \cdot \hat{\boldsymbol{n}}_{\boldsymbol{d}} \, ds \\
&= \iint_{S_d} (\boldsymbol{E_{Rx}^{Air}} \cdot (\boldsymbol{H_T^{Air}} \times \hat{\boldsymbol{n}}_{\boldsymbol{d}}) - \boldsymbol{E_T^{Air}} \cdot (\boldsymbol{H_{Rx}^{Air}} \times \hat{\boldsymbol{n}}_{\boldsymbol{d}})) \, ds \\
&= \int_0^{2\pi} \int_a^b (\boldsymbol{E_{Rx}^{Air}} \cdot (\boldsymbol{0}) - \frac{V_{oc}}{\rho \ln \frac{b}{a}} \hat{\boldsymbol{\rho}} \cdot (\frac{I_{Rx}}{2\pi\rho} \hat{\boldsymbol{\phi}} \times \hat{\boldsymbol{z}})) \, \rho \, d\rho \, d\phi \\
&= -V_{oc} I_{Rx}
\end{aligned} \tag{2.7}$$

The only surface left is S_{iU} which is the surface touching the air-soil interface. From (2.2), (2.3), (2.4) and (2.7) we can write:

$$\begin{aligned}
&\iint_{S_{iU}} (\boldsymbol{H_T^{Air}} \cdot (\hat{\boldsymbol{n_{iU}}} \times \boldsymbol{E_{Rx}^{Air}}) - \boldsymbol{H_{Rx}^{Air}} \cdot (\hat{\boldsymbol{n_{iU}}} \times \boldsymbol{E_T^{Air}})) \, ds \\
&= V_{oc} I_{Rx}
\end{aligned} \tag{2.8}$$

Now, we apply the reciprocity relations to the impressed $\boldsymbol{J_{s_T}}$ source in the homoge-

neous soil with the surfaces identified in Fig. 2.3b

$$\oiint_{S_{\infty L}+S_{iL}} (\boldsymbol{E}_{\boldsymbol{Rx}}^{\boldsymbol{Soil}} \times \boldsymbol{H}_{\boldsymbol{T}}^{\boldsymbol{Soil}} - \boldsymbol{E}_{\boldsymbol{T}}^{\boldsymbol{Soil}} \times \boldsymbol{H}_{\boldsymbol{Rx}}^{\boldsymbol{Soil}}) \cdot \hat{\boldsymbol{n}}\, ds$$
$$= \iint_{S_{iL}} (\boldsymbol{H}_{\boldsymbol{T}}^{\boldsymbol{Soil}} \cdot (\hat{\boldsymbol{n_{iL}}} \times \boldsymbol{E}_{\boldsymbol{Rx}}^{\boldsymbol{Soil}}) - \boldsymbol{H}_{\boldsymbol{Rx}}^{\boldsymbol{Soil}} \cdot (\hat{\boldsymbol{n_{iL}}} \times \boldsymbol{E}_{\boldsymbol{T}}^{\boldsymbol{Soil}}))\, ds$$
$$= \iint_{S_{Target}} -\boldsymbol{J}_{\boldsymbol{s_T}} \cdot \boldsymbol{E}_{\boldsymbol{Rx}}^{\boldsymbol{Soil}}\, ds \tag{2.9}$$

In the derivation, we followed the same argument we used to obtain (2.3) by ignoring the zero contribution from the lower infinite hemisphere $S_{\infty L}$. Applying the continuity of the tangential E and H components along the air-soil interface and noting that $\hat{\boldsymbol{n_{iU}}}$ = - $\hat{\boldsymbol{n_{iL}}}$, we have:

$$\boldsymbol{H}_{\boldsymbol{T}}^{\boldsymbol{Air}} \cdot (\hat{\boldsymbol{n_{iU}}} \times \boldsymbol{E}_{\boldsymbol{Rx}}^{\boldsymbol{Air}}) - \boldsymbol{H}_{\boldsymbol{Rx}}^{\boldsymbol{Air}} \cdot (\hat{\boldsymbol{n_{iU}}} \times \boldsymbol{E}_{\boldsymbol{T}}^{\boldsymbol{Air}})$$
$$= \boldsymbol{H}_{\boldsymbol{Rx}}^{\boldsymbol{Soil}} \cdot (\hat{\boldsymbol{n_{iL}}} \times \boldsymbol{E}_{\boldsymbol{T}}^{\boldsymbol{Soil}}) - \boldsymbol{H}_{\boldsymbol{T}}^{\boldsymbol{Soil}} \cdot (\hat{\boldsymbol{n_{iL}}} \times \boldsymbol{E}_{\boldsymbol{Rx}}^{\boldsymbol{Soil}}) \tag{2.10}$$

Combining (2.8), (2.9) and (2.10), the open circuit voltage can be found from:

$$V_{oc} = \frac{1}{I_{Rx}} \iint_{S_{Target}} \boldsymbol{J}_{\boldsymbol{s_T}} \cdot \boldsymbol{E}_{\boldsymbol{Rx}}^{\boldsymbol{Soil}}\, ds \tag{2.11}$$

This formula indicates that to obtain V_{oc} at the Rx terminals due to the scattered field from the target for any Rx position, we only need two quantities. The first is $\boldsymbol{J}_{\boldsymbol{s_T}}$, which is obtained by performing one full-wave simulation of Tx and target inside the soil as a function of frequency under the approximation that $\boldsymbol{J}_{\boldsymbol{s_T}}$ is not affected by the Rx presence. The second is the E field everywhere in the lower half-space where Rx is used as a transmitter and its field is calculated for all desired frequencies. This field calculation is sufficient to find $\boldsymbol{E}_{\boldsymbol{Rx}}^{\boldsymbol{Soil}}$ at any point on the target surface location for

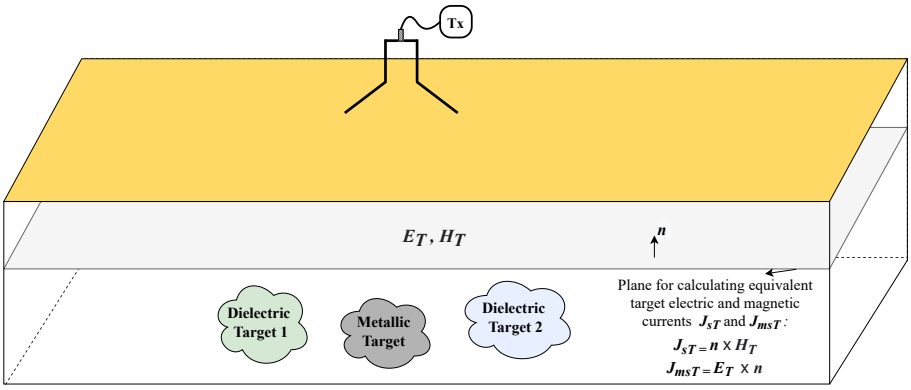


Figure 2.4: Tx above half-space, the scattered field from the targets can be computed along a hypothetical plane. Then, the scattered electric ($\boldsymbol{E_T}$) and magnetic ($\boldsymbol{H_T}$) fields can be converted to equivalent currents representing the scattered field due to all the dielectric and metallic targets below the plane.

any receiver position or orientation because Rx is above a homogeneous soil medium and there are no orientation-dependent scatterers in the scene. Therefore, instead of performing a new simulation for (Tx, Rx at position n, target inside soil) every time Rx moves to a new position in order to obtain V_{oc}, we only need two simulations, which leads to a decrease in computation time by a factor of $\frac{N}{2}$, where N is the number of Rx positions (sampling points) required to form a SAR image. It should be noted that the derivation was done for metallic targets for clarity of illustration, but the method should work equally well for any type of target whether it is dielectric or metallic. This is done by the help of the source equivalence principle [76]. Basically, instead of finding the currents on the surface of the target, the fields can be calculated along a hypothetical plane, then converted into equivalent electric and magnetic currents as illustrated in Fig. 2.4. When this is done, the final formula for computing the voltage induced across the Rx terminals becomes:

$$V_{oc} = \frac{1}{I_{Rx}} \iint_{Plane} \left(\boldsymbol{J_{s_T}} \cdot \boldsymbol{E_{Rx}^{Soil}} - \boldsymbol{J_{ms_T}} \cdot \boldsymbol{H_{Rx}^{Soil}} \right) ds \tag{2.12}$$

where the equivalent targets surface currents on the plane are obtained by:

$$\boldsymbol{J}_{s_T} = \boldsymbol{n} \times \boldsymbol{H}_T \tag{2.13}$$

$$\boldsymbol{J}_{sm_T} = \boldsymbol{E}_T \times \boldsymbol{n} \tag{2.14}$$

Here, $\boldsymbol{n}$ is the normal vector of the plane as indicate in Fig. 2.4, and $\boldsymbol{E_T}, \boldsymbol{H_T}$ refer to the scattered fields due to the targets at the plane where the equivalent currents are calculated. It should be noted that the method should work for inhomogeneous stratified soil too by introducing new integration surfaces and applying boundary conditions just like what was done in (2.8) through (2.11).

2.3 Simulation and Imaging Results

To demonstrate the performance of the proposed method, we considered a realistic scenario of two antennas, a fixed transmitter and a fixed receiver, above soil surface with a PEC sphere as a target buried deeply in the soil medium. The antenna used for both Tx and Rx is an out-of-phase fed parallel geometry of a two-element antenna array, as shown in Fig. 2.5. This antenna is designed for ground penetrating radar applications and is described in [78]. The Tx and Rx antennas are located 2 meters apart and 10 cm above a dry soil surface with relative permittivity of 3.5 and loss tangent of 0.01714. The PEC sphere has a 15-cm radius and is buried at a 1-m depth inside the soil medium, right below the Tx. As means of comparison, a conventional (brute-force) method and the proposed method are each used to obtain V_{oc} data. For the conventional method, a simulation of (Tx,Rx,Target) and (Tx,Rx) are preformed and the resulting V_{oc} values are subtracted on from the other, to isolate the response of the target from the Tx-Rx signal, as well as the soil interface reflections. As mentioned in the previous section, regarding the fast method, the higher order signals such as Tx-Rx-Target and Target-Tx-Rx can be considered to be negligible and ignored in

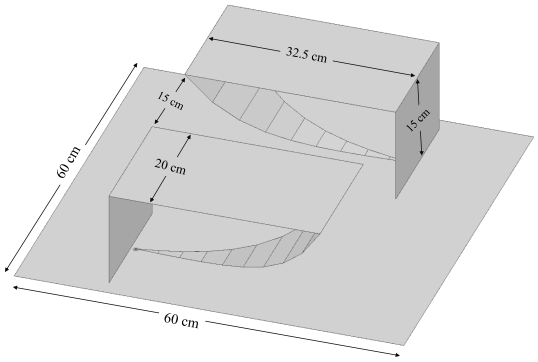
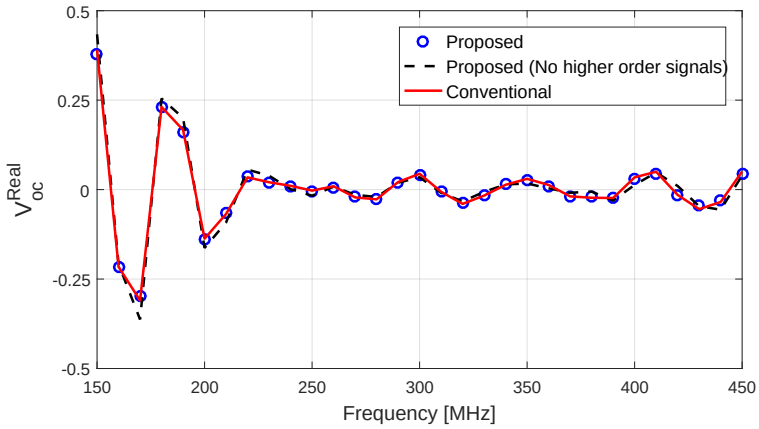
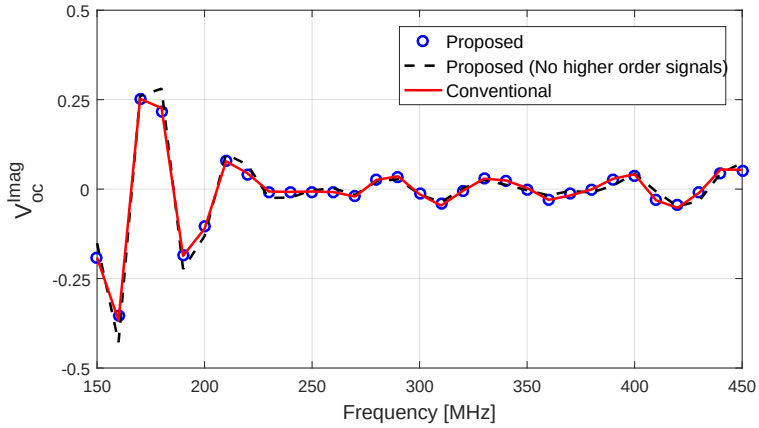


Figure 2.5: Parallel geometry ENVELOP antenna array used in simulation.

this method. To test this assumption, a simulation of (Tx,Target) is performed to obtain $\boldsymbol{J_{sT}}$ with and without the presence of Rx. Another simulation of Rx above the soil surface is carried out to obtain $\boldsymbol{E_{RX}^{Soil}}$, with and without the presence of Tx. Next, (2.11) is used to obtain V_{oc} due to the target, including and excluding the higher-order signals. Simulations are performed with a discrete frequency sweep settings in an ANSYS HFSS software environment for 31 frequency points in the range 150 MHz to 450 MHz as dictated by the bandwidth of the antenna. Fine local mesh settings are applied around the target surface to obtain accurate results. Fig. 2.6 shows the results of the conventional and proposed methods. There is an almost exact agreement between the conventional and the proposed methods when the higher order effects are included and very good agreement when they are excluded, which supports the validity of our assumption in the derivation of the proposed method. The same comparison is performed again using three other PEC targets, one is an extended target and the other two have more complex geometries. The extended target is a cylinder 1-meter in length and 7.5-cm in radius, buried at 1-meter depth, right below the Tx antenna and oriented 45 degrees from the line connecting the Tx and the Rx antennas. The Tx and the Rx antennas are separated by 2 meters and located 10 cm above the soil surface, just like in the sphere case. The open-circuit voltage computed using the full-wave analysis and the proposed approximate method

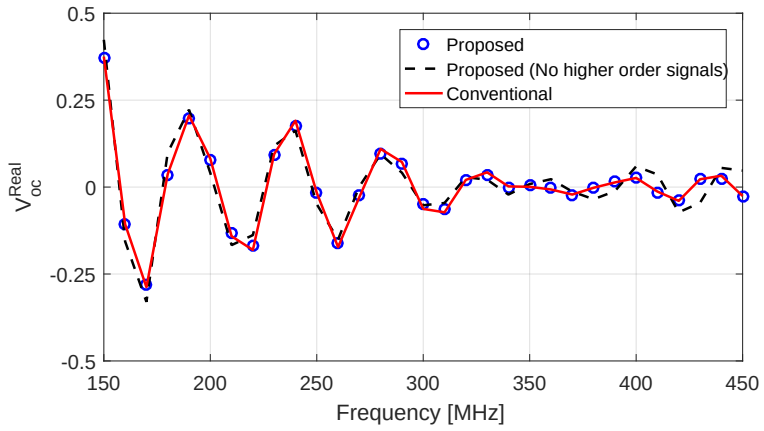


(a)

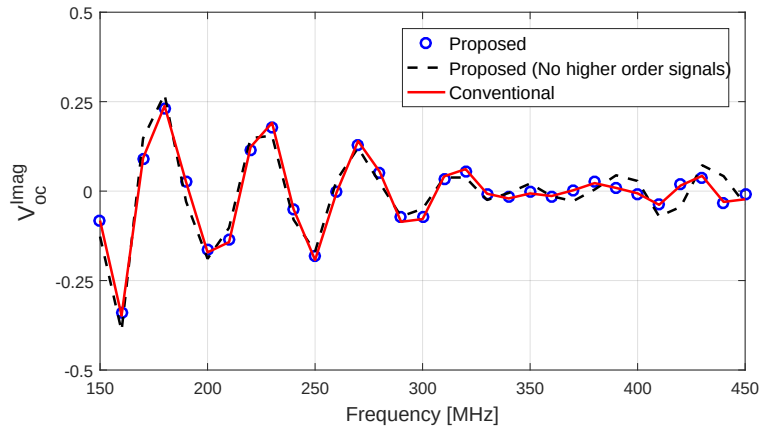


(b)

Figure 2.6: The real (a) and imaginary (b) parts of V_{oc} due to a PEC sphere obtained using the conventional (brute force) and the proposed (fast) methods.



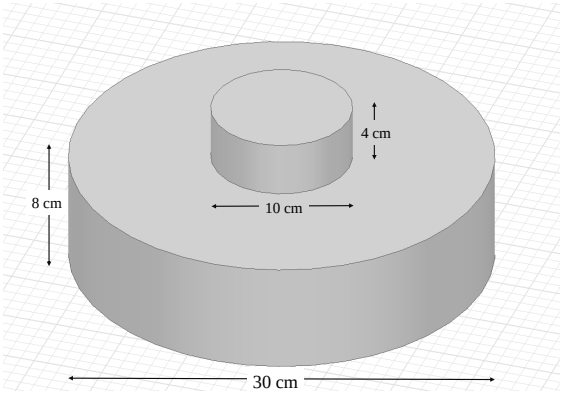
(a)



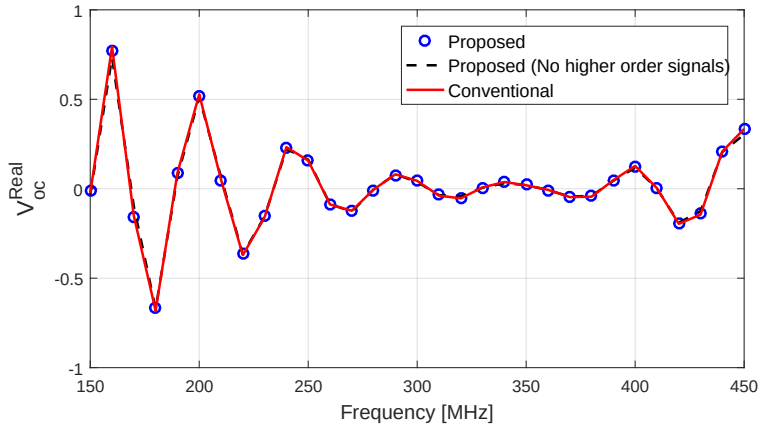
(b)

Figure 2.7: The real (a) and imaginary (b) parts of V_{oc} due to a PEC Cylinder obtained using the conventional (brute force) and the proposed (fast) methods.

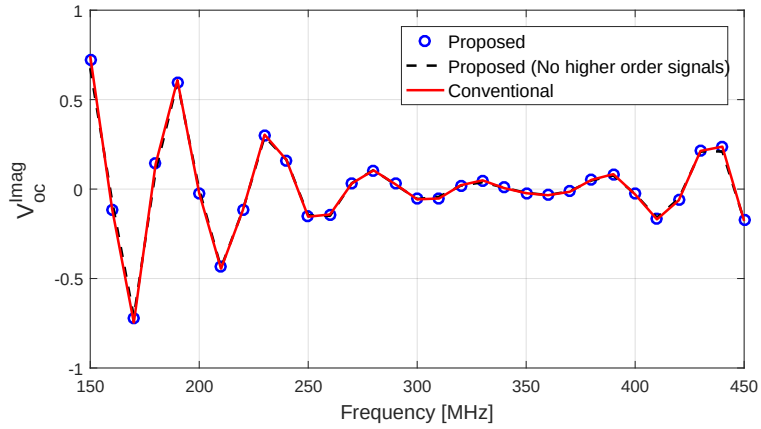
for the cylinder are compared in Fig. 2.7. There is good agreement in the results just like in the sphere case. The next target is composed of two circular cylinders connected with each other to represent a landmine. The landmine is buried at a 1-meter depth at equal distance from the Tx and the Rx antennas, where the Tx and the Rx antennas have the same positions as in the sphere case. The comparison of the results, along with the dimension of the landmine, are shown in Fig. 2.8 where excellent agreement is observed. The last complex target is composed of an ancient soldier's shield and sword that resemble what might be found in an archaeological site. The geometry of the complex target is shown in Fig. 2.9a. It is buried at a 0.7-meter depth inside the soil medium right below the Tx antenna. The Tx and the Rx antennas are separated by 1.6-meters and located 10 cm above the soil. Fig. 2.9 shows the comparison of the open-circuit voltages at the receiver for the complex target. The results show excellent agreement between the proposed and conventional methods when including higher order signals, and a small deviation when excluding the higher order signals. This is expected as the complex target is buried at a lower depth than the sphere case and the Rx antenna is brought closer to the Tx antenna in this simulation, compared to the previous simulations, leading to more prevalence for the ignored higher order signals. After confirming the validity of the proposed method for one fixed Rx position, the computation is carried out to generate data for all Rx positions required in SAR imaging. Using the same settings for the sphere simulation, V_{oc} data are obtained for 42 Rx positions located uniformly on a circle with a 2-meter radius centered right above the sphere. Next, back-projection formula (2.1) was applied to form a 3-D SAR image. Fig. 2.10 shows a two-plane cut of the reconstructed 3-D image for the sphere. The image reconstruction works well and indicates a target around 1 meter depth with an approximate radius of 15 cm. This gives further validation for the validity of the data set generated by the proposed fast method.



(a)

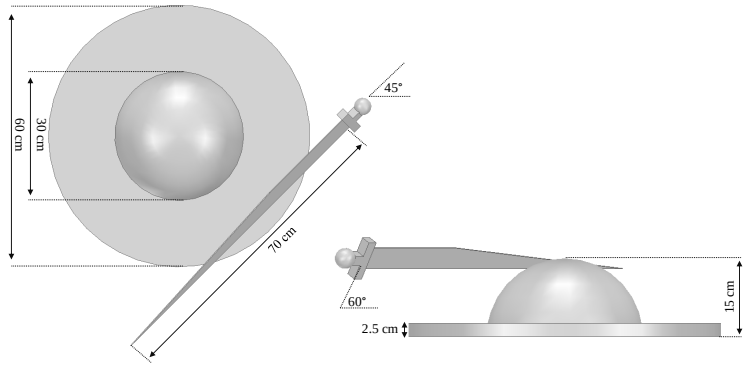


(b)

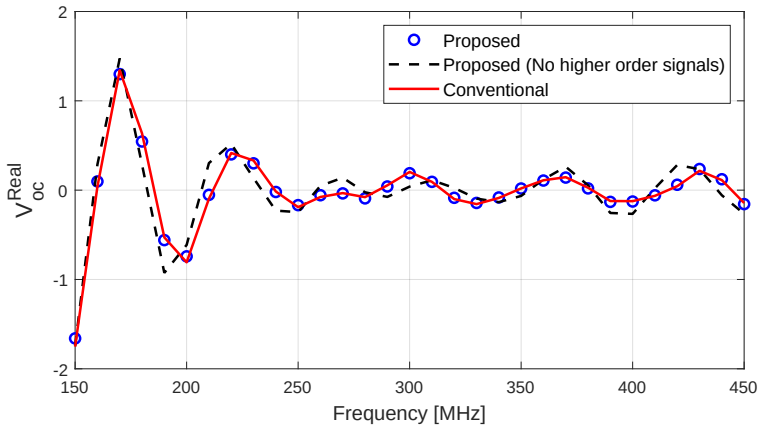


(c)

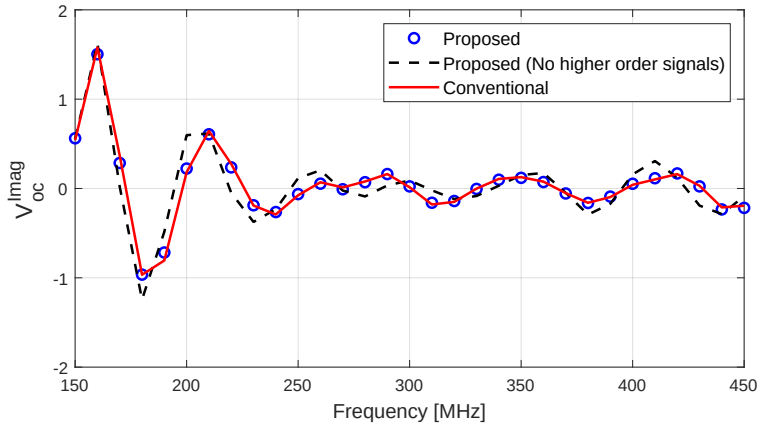
Figure 2.8: PEC Landmine geometry (a), the real (b) and imaginary (c) parts of V_{oc} due to the Landmine obtained using the conventional (brute force) and the proposed (fast) methods.



(a)



(b)



(c)

Figure 2.9: Complex PEC target geometry (a), the real (b) and imaginary (c) parts of V_{oc} due to the Complex target obtained using the conventional (brute force) and the proposed (fast) methods.

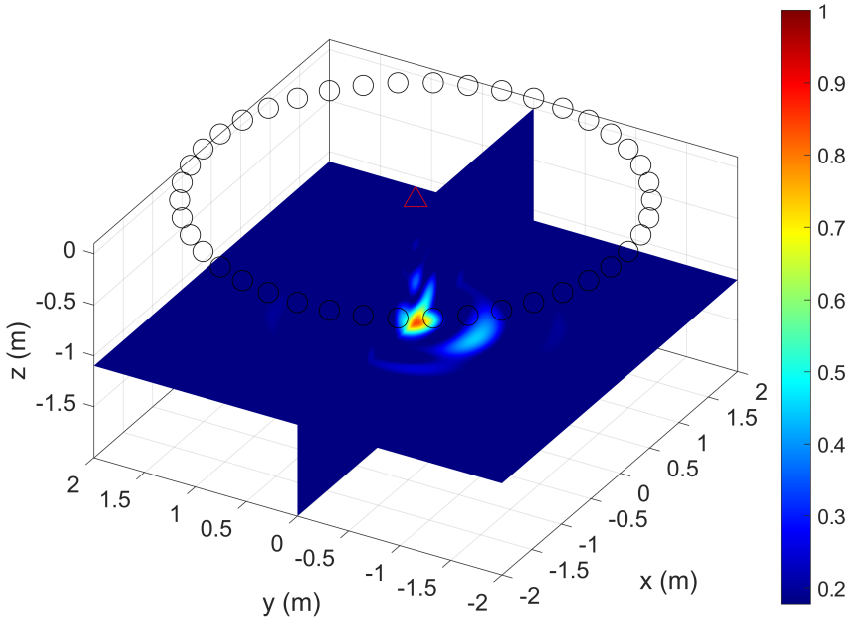


Figure 2.10: Two-planes cut of a reconstructed 3-D image of a 15 cm radius PEC sphere buried at 1 meter depth Tx is indicated by triangle and sampling points are indicated by circles.

2.4 Conclusion

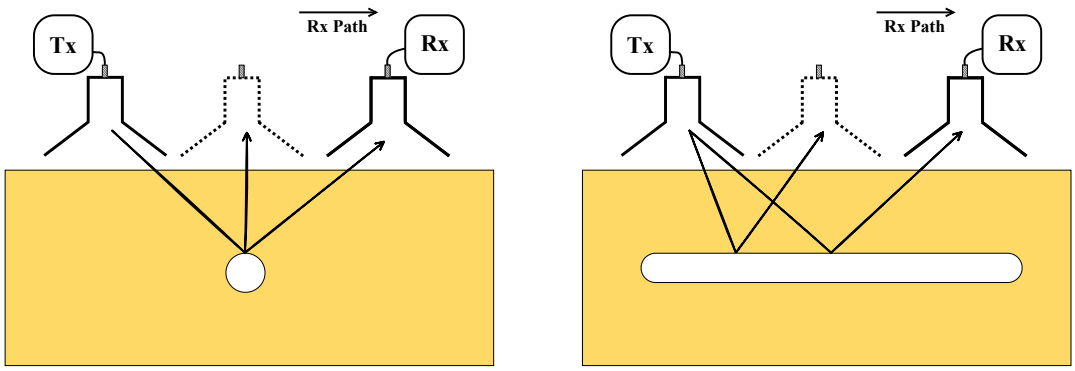
In this chapter, a fast full-wave simulation method for calculating the scattering from buried objects for a multistatic imaging radar is proposed. The method works by replacing the target with its equivalent current distribution and using the receiver as a transmitter, along with applying reciprocity relations to calculate the open circuit voltage across the receiver's terminals due to the target. A detailed derivation as well as comparison results with conventional full-wave simulation are presented. Additionally, the reliability of the method is tested by performing a 3-D SAR image reconstruction on a dataset generated by the proposed method. The method can serve as a good tool for generating data for performance evaluation of different subsurface imaging techniques.

CHAPTER 3

Detection and Localization of Buried Pipelines

3.1 Introduction

Detection and localization of buried pipelines using a multistatic subsurface SAR configuration is a challenging problem. The challenge arises from the extended nature of pipelines which makes the use of traditional focusing algorithms not feasible because these algorithms assume a point-target scattering mechanism with a fixed scattering phase center for all receivers. By incorporating the unique scattering mechanism of pipelines as shown in Fig. 3.1, this chapter presents a novel algorithm for imaging pipelines which works by tracking the pipeline scattering phase centers and coherently summing the measured multistatic signals after compensating for the phase shifts due to each scattering phase center. The rest of the chapter is organized as follows. Section 3.2 starts with the 3D pipeline scattering model, leading to the derivation of a novel pipeline detection and localization algorithm. Section 3.3 uses the analytical model along with numerical simulations to justify the assumptions made in the derivation of the pipelines detection and localization algorithm and to contrast the proposed algorithm with the hyperbola recognition approach currently in use in the literature, Section 3.4 provides full-wave simulations as well as experimental measurement results demonstrating the effectiveness of the proposed algorithm.



(a) (b)

Figure 3.1: Side view of multistatic subsurface SAR scattering mechanism of a point target with a single scattering phase center for all Rx (a) and a pipeline with unique scattering phase center for each Rx (b).

3.2 Pipeline Detection and Localization Algorithm

The geometry of the problem is shown in Fig. 3.1 where a dielectric or metallic pipe is placed in a half-space dielectric medium with the pipe being parallel to the air-dielectric interface.

3.2.1 Forward Problem

Assuming $e^{j\omega t}$ time dependence and plane-wave incidence at angle θ_i with respect to the pipeline axis (z-axis), the scattered field from the pipeline can be written compactly as:

$$\boldsymbol{E^s} = \sum_{n=-\infty}^{\infty} \Big[\Big(\boldsymbol{a_n}(\theta_i, r_{in}, r_{out}) H_n^{(2)}(k_\rho\, \rho) + \boldsymbol{b_n}(\theta_i, r_{in}, r_{out}) H_n^{(2)'}(k_\rho\, \rho) \Big) e^{-jn\phi} \Big] e^{-jk_z z} \quad (3.1)$$

where $k_\rho = k\, sin\theta_i$, $k_z = k\, cos\theta_i$, k is the wave number for the background medium and $H_n^{(2)}(.)$ is the Hankel function of the second kind. Vectors $\boldsymbol{a_n}$ and $\boldsymbol{b_n}$ specify the components of the scattered field and match the boundary conditions for TE^z and

TM^z modes and can be found analytically for various types of pipes [79, 80, 81, 82, 83]. Lastly, r_{in} and r_{out} are the inner and outer radii of the pipe, which are the same for a single-layer pipe. Insofar as the far-field behavior of the scattered field is concerned, the large argument expansion of the Hankel functions [84] can be used to simplify the expression in (3.1) to:

$$\boldsymbol{E^s} \approx \boldsymbol{A}(\rho, \phi, \theta_i, r_{in}, r_{out})\, e^{-j(k\, cos\theta_i z + k\, sin\theta_i \rho)} \tag{3.2}$$

where the vector $\boldsymbol{A}$ lumps the summation and all the terms inside it. If the phase contribution from this vector is ignored (a step that will be justified in the next section), the equation describing constant-phase contours becomes:

$$k\,(sin\theta_i\,\rho + cos\theta_i\,z) = constant \tag{3.3}$$

This equation describes a collection of circles on the surface of a cone with generating angle θ_i as the value of z gets larger. This means that for an incident wave with an angle θ_i, the scattered field will have a phase that progresses along the cone surface until the receiver is reached. Hence, the conical scattered field from a point on the pipe reaches only a subset of the receivers whose locations intersect with the cone, as opposed to the scattered field from a point target that reaches all receivers. This fact is the reason for why applying the BP algorithm directly to the scattered field from a pipe does not work well and leads to ill-focused images. To overcome this problem, the phase needs to be compensated for in a way that is appropriate to the pipe scattering behavior.

3.2.2 Inversion Algorithm

Using the behavior of the scattered field, together with the knowledge of the locations of the transmitter and the receivers, the aim of the inversion algorithm is to determine

the depth, and orientation, as well as the horizontal displacement of the pipe with respect to the transmitter location. Fig. 3.2a gives a top view of the subsurface SAR system as well as the coordinate systems. Also, Fig. 3.2b gives a perspective view of the pipeline and the local (primed) coordinate system. The primed coordinate system is obtained by rotating the x-axis by α, shifting the origin horizontally by d and downward by h. Hence, α, d and h represent the pipeline parameters that need to be determined by the inversion algorithm. The equation describing the forward scattering cone for a point along the pipe located on the z'-axis (for which the incident angle from the transmitter is θ_i) is given by:

$$y'^2 + x'^2 = tan^2\theta_i\Big(z' - R\,cot\theta_i\Big)^2 \tag{3.4}$$

where $(0, 0, R\,cot\theta_i)$ is the location of the cone tip (see Fig. 3.2b). As seen by the primed coordinates, the cone will intersect the plane containing Tx and Rxs at height h and form a hyperbola that is described by:

$$h^2 + x'^2 = tan^2\theta_i\Big(z' - R\,cot\theta_i\Big)^2 \tag{3.5}$$

Conversely, for the n^{th} Rx location (x'_{on}, h, z'_{on}), there is a unique cone that will intersect it, which can be found by substituting the Rx coordinates in the the hyperbola equation (3.5) and solving for θ_i. The solution leads to two values of θ_i but only one of them is a physical solution, which is given by:

$$\theta_i^n = \arctan\Big(\frac{\sqrt{h^2 + x'^2_{on}} + R}{z'_{on}}\Big) \tag{3.6}$$

Having found the cone generating angle, the cone tip (scattering phase center) along the pipe for the n^{th} Rx can be found by $S^n = (0, 0, R\,cot\theta_i^n)$ and this can be used to determine the actual bistatic path the wave has taken from Tx to the n^{th} Rx. This

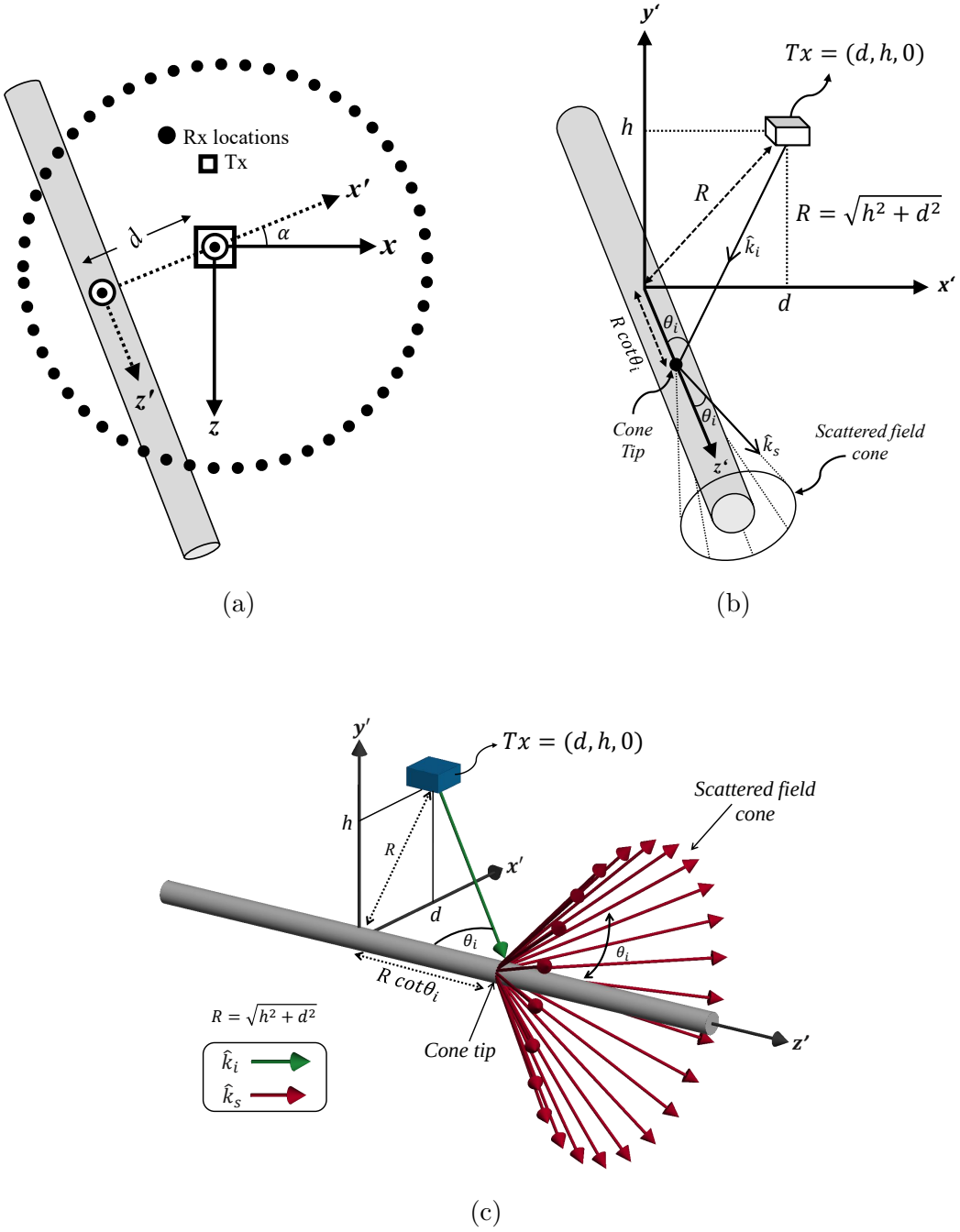


Figure 3.2: (a) Top view of the coordinates showing the pipe and the subsurface SAR system and (b) the primed local coordinates along the pipe axis and (c) a colored illustration of the pipeline scattering mechanism as seen by the primed coordinates.

pathlength is given by:

$$PL\left(Rx_n\right) = R_{Tx-S^n} + R_{S^n-Rx_n} \tag{3.7}$$

where,

$$R_{Tx-S^n} = \sqrt{(R\,cot\,\theta_i^n)^2 + R^2} \tag{3.8}$$

$$R_{S^n-Rx_n} = \sqrt{(R\,cot\,\theta_i^n - z'_{on})^2 + x'^2_{on} + h^2} \tag{3.9}$$

Using (3.7), the path length can be obtained for any Rx (sampling point). This allows for compensating for the phase of the received field at each Rx. The phase-compensated signals add up coherently for all receivers and frequencies to find the pipeline parameters. Mathematically:

$$Search(\alpha, d, h) = \sum_{m=1}^{M}\sum_{n=1}^{N} V^{nm} e^{j\left(k^m PL\left(Rx_n\right)\right)} \tag{3.10}$$

where V^{mn} is the received voltage for the n^{th} Rx terminal at the m^{th} frequency and k_m is the wave number at that frequency. The sum in (3.10) attains its maximum value for different values of α, d and h that correspond to the actual pipelines parameters. Fig. 3.3 summarizes the algorithm steps and the associated MATLAB code is found in Appendix. A.

3.3 Analytical and Numerical Analysis

In the derivation of the inversion algorithm, several assumptions have been made. This section aims to examine the impact of these assumptions which include: 1) the radar antennas are at the far-field of the pipeline and vice versa, 2) the phase behavior of the scattered field depends on the conical phase propagation and the phase due to other terms in (3.2) are negligible and 3) the actual model of half space can be replaced with a single medium (ignoring the air-dielectric interface) without incurring

Algorithm I Pipelines Detection and Localization in SAR

Input: $\{V_{11}, \dots, V_{MN}\}, \{(x_{o1}, z_{o1}), \dots, (x_{oN}, z_{oN})\}$,
$\{(\alpha_1, d_1, h_1), \dots, (\alpha_K, d_K, h_K)\}$,

For *k=1 to K* **Do**

- Transform (x_{on}, z_{on}) into (α_k, d_k, h_k) coordinates $\forall n$
- Solve for θ_i^n $\forall n$
- Calculate R_{Tx-S^n} and $R_{S^n-Rx_n}$ $\forall n$
- Compensate for the pipeline phase and do a coherent sum
- Save the sum in $Search(\alpha_k, d_k, h_k)$

End

$$(\alpha, d, h)_{Actual} = \underset{(\alpha,d,h)}{\operatorname{argmax}} |Search(\alpha, d, h)|$$

Figure 3.3: Algorithm for pipelines detection and localization in multistatic subsurface SAR.

much error in the final results. Moreover, the sensitivity of the pipe parameters estimation as a function of error in the background medium permittivity is investigated and a method to estimate the background medium dielectric is suggested. Finally, the time domain responses of the pipe for different multi-static Tx-Rx arrangements is investigated to contrast the proposed algorithm with the hyperbola recognition approach.

3.3.1 The Accuracy of Far-field Assumption

In the derivation of the proposed algorithm, two assumptions were made regrading the phase of the transmitted and received signals. The first assumption is that the Tx and the Rx are ideal points that send and receive plane waves with phases solely dependent on spatial propagation. In reality, the antennas of both Tx and Rx may add additional phase depending on the location of the target relative to the antenna, and this is particularly true when the antenna is electrically large and the target is in the near-field of the antenna. The other assumption is that the Rx is far enough from

the pipeline, allowing the use of large-argument expansion of the Hankel function to move from expression (3.1) to (3.2). To investigate the first assumption, Ansys HFSS full-wave simulation software was used to find the phases of the transmitted field from two different antennas. The first antenna is a Hertzian dipole that is used in the simulation section and the other is the ENVELOP antenna described in [78] and used in the measurement section. Both antennas are placed 5 cm above lossless sand with a dielectric constant of 5. After that, the additional phase introduced by the antenna is calculated as follows:

$$AP(r,\theta,\phi) = phase\Big[\Big(E_\theta(r,\theta,\phi) + E_\phi(r,\theta,\phi)\Big)e^{jkr}\Big] \tag{3.11}$$

Here, it is assumed that the centroid of the antenna is at the origin of the spherical coordinates, and E_θ and E_ϕ are the transverse components of the field radiated by the antenna. The multiplication by e^{jkr} removes the phase due to spatial propagation, leaving the additional phase introduced by the antenna. Fig. 3.4 shows the mean value of $AP(r,\theta,\phi)$ over the main lobe of the ENVELOP antenna ($\phi \in [0, 360]$ with $\theta \in [-60, 60]$) for different values of r for the two antennas used in this work at 300 MHz (the center frequency of the subsurface radar system used in this chapter). As expected, the Hertzian dipole introduces no additional phase other than propagation phase while the ENVELOP antenna does introduce a phase that does not exceed 30 degrees, on average, even if the target is in the near-field of the antenna. The same analysis applies to the antenna when it acts as a receiver, due to the reciprocity theorem (see Chapter 2 for more details). The phase error due to the ENVELOP antenna is not large because the antenna size is electrically small ($< \lambda_{min}$ in maximum dimension). For electrically larger antennas, the phase introduced by the antenna might be significant, in which case it needs to be calibrated out before applying the pipe detection algorithm. The calibration might be done by obtaining the additional

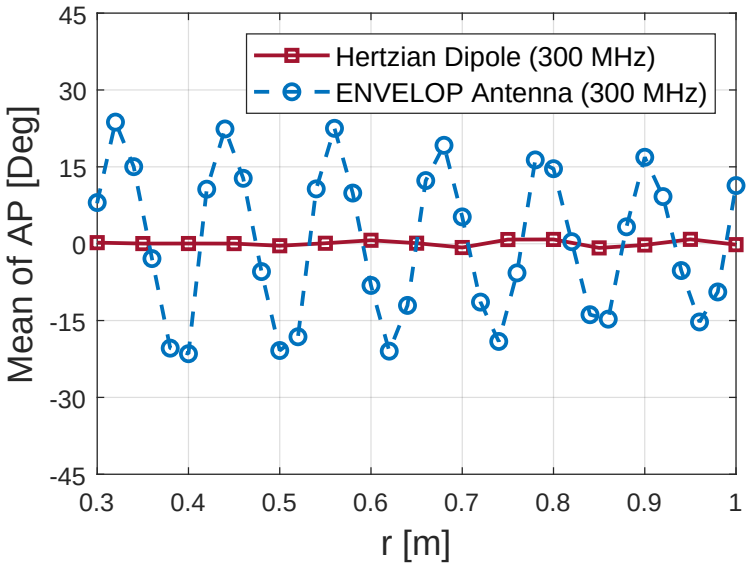


Figure 3.4: Mean value of the phase introduced by the antenna over the main lobe at various distances.

antenna phase via full-wave simulation, then eliminating it from the radar response or by following other calibration techniques such as the one discussed in [85] for the case of a horn antenna in GPR. The other assumption (using large-argument approximation of Hankel function) is examined as follows. Using the analytical formulas for pipeline scattering derived in [79] for a metallic pipe and in [82] for a concentric dielectric pipe, the scattered field phase was calculated using the exact expression as well as the large-argument approximation of Hankel function. Basically, the phase difference between the two expressions is examined. As representative examples, a metallic pipe with a diameter of 20 cm and a concentric dielectric pipe with diameters of 20 and 15 cm are considered. The frequency is set to 300 MHz. The dielectric value for the background medium is set to a typical value for sand which is 5 and the dielectric values for the core of the dielectric pipe is set to $80 - j20$, resembling the dielectric of water [86], while the outer layer dielectric is set to 3, a typical value for PVC material. Fig. 3.5 shows the phase error due to the far-field approximation of Hankel function as a function of the pipe depth (i.e., h). As shown, even when the Rx

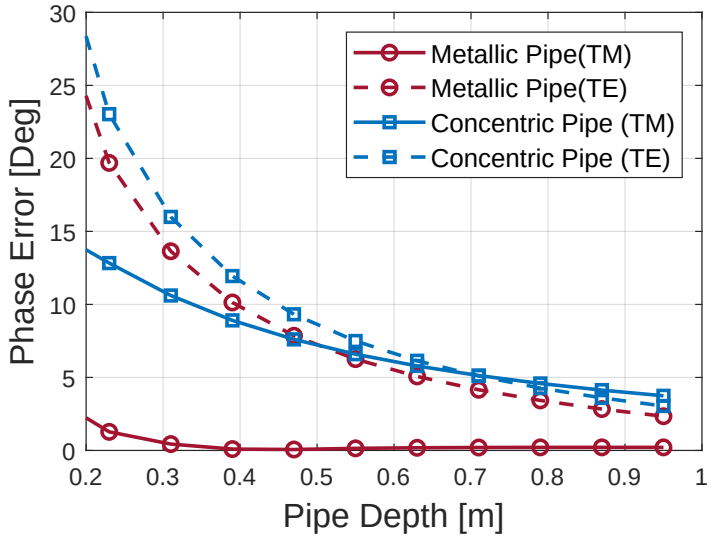


Figure 3.5: Phase error due to far-field approximation of Hankel function.

is less than one diameter above the pipe, the maximum phase error does not exceed 30 degrees, which is an acceptable phase deviation in the proposed imaging algorithm. The reason 30 degrees is taken as an acceptable cut-off for phase error is because the algorithm relies on the phase-compensated signals (phasors) to be aligned along a particular direction in a statistical sense and at 30-degree deviation, more than 86% of the phasor is aligned in the right direction.

3.3.2 Conical Phase Front Assumption

In the forward-model derivation, the scattered field phase is solely attributed to the conical propagation and the phase due to the summation term $\boldsymbol{A}$ in (3.2) is ignored. This assumption can be easily verified if the pipe diameter is electrically small by direct examination of the analytical formulas for the scattered field. This simplification fails when the pipe diameter becomes large in terms of wavelength, in which case the non-conical phase contribution to the scattered field has to be taken into account. To investigate the effect of these other phase sources, Altair FEKO simulation software is used to generate the scattered field phase of a pipe buried in soil with $\epsilon_{Soil} = 5.4$.

Then, the simplified forward model is used to predict the phase and the phase error between the simplified model and FEKO data is calculated. Two scenarios are considered, a metallic and a concentric dielectric pipe. The dielectric materials are the same as in the previous example and the ratio between the inner and outer diameters for the dielectric pipe is 5/6. Both Tx and Rx antennas are composed of two Hertzian dipoles perpendicular to each other and have a 90 degree phase shift so as to generate a circular polarization that excites both TE^z and TM^z modes in the scattered field. In both scenarios, the pipe is located at 1-m depth and the Rx samples are uniformly distributed on a 6-m line along the pipe axis, while the Tx is fixed in the middle of the Rx samples. The frequencies considered in the simulation are from 150 MHz to 450 MHz. Fig. 3.6 shows the mean phase error (across all frequencies and sampling points) as a function of the pipe diameter. Here the phase is calculated once by assuming the scattering phase centers to be at the pipe core (as implied mathematically in (3.2)), and then again by placing the phase centers at the pipe's top surface. By examining the phase error, it is obvious that the phase associated with the term $\boldsymbol{A}$ in (3.2) is correcting for physical location of the phase center which is on the surface of the pipe and not at its core. Therefore, ignoring the non-conical phase terms does not invalidate the model, it only tells us that the algorithm will detect the depth of the pipe measured at its top surface rather than its center.

3.3.3 Single Medium Assumption

The soil over the pipeline was assumed to be a single medium in the forward model derivation instead of a half-space. This assumption is partly justified by the fact that the Tx and Rx antennas in the SAR system considered in this chapter are supposed to be very close to the air-soil interface (less than 10 cm above it). To provide further justification, FEKO software is used to generate scattered-field data for a pipe buried in a half-space air-soil medium. The simulations are carried out for a metallic pipe

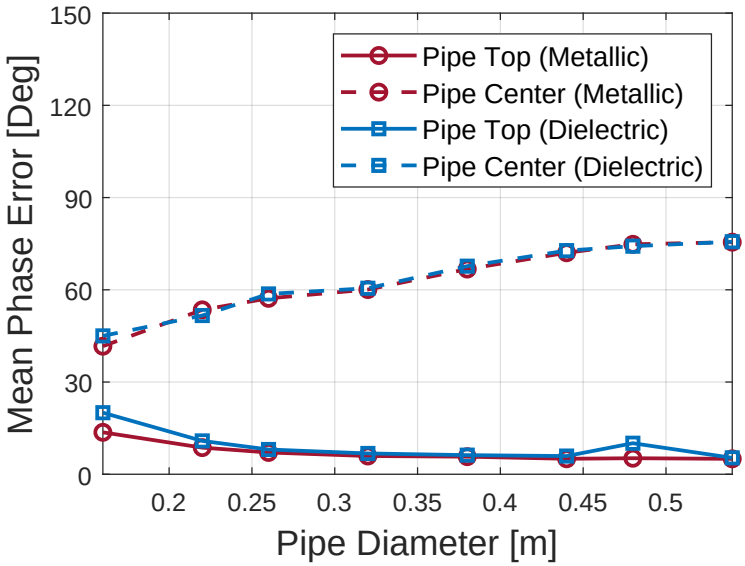


Figure 3.6: Mean phase error across all Rxs and frequencies Vs pipe diameter.

5 cm in diameter and buried at 80 cm depth, over the frequency range of 150 MHz to 450 MHz using circularly polarized Hertzian dipoles as antennas located 10 cm above the air-soil interface. The Rx samples are taken along three concentric circles with radii of 1, 1.5 and 2 meters, where the Tx is fixed in the middle of the circles. Next, the phase difference in the scattered field between the forward model data and FEKO data is calculated. Fig. 3.7 shows the mean value of the phase error across all frequencies and Rx samples versus different values of half-space dielectric. As shown, irrespective of the dielectric value, the error never exceeds 20 degrees. Hence, if the antennas are 10 cm or less above the interface, replacing the half space with a single medium does not affect the algorithm performance in any significant way.

3.3.4 Soil Dielectric Estimation

Another important goal of the proposed algorithm is to estimate the background medium's permittivity. When applying the algorithm to a real scenario, it is most likely that the background permittivity is unknown. In such cases, multiple permittivity values are considered and the algorithm is applied to each of them. The permit-

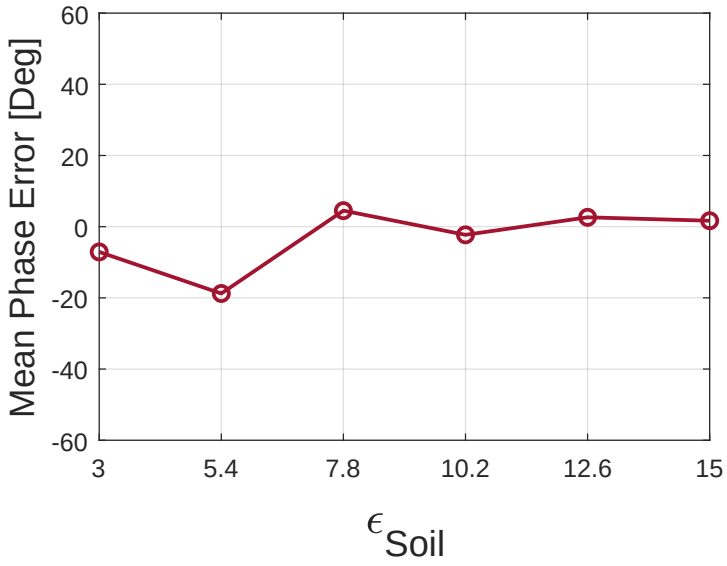


Figure 3.7: Mean value of the scattered field phase error between the forward model and FEKO simulation data.

tivity value that provides the highest coherence (highest peak of $|Search(\alpha, d, h)|$) is taken to be the background dielectric value. In this way, not only does the algorithm detect the pipeline, but it also measures the permittivity of the soil. To examine the sensitivity in the estimation of the background dielectric, the algorithm is performed on the FEKO simulation data of the previous example (a metallic pipe buried in a single soil medium with $\epsilon_{Soil} = 5.4$). Fig. 3.8 shows the pipe parameters estimated by the algorithm as a function of error in the value of the soil dielectric constant. Here, it is assumed that the soil dielectric is known. It is shown that the pipe depth (h) and displacement (d) are affected by errors in ϵ_{Soil} while the pipe orientation (α) is virtually independent of our choice of ϵ_{Soil}. This suggests a method to estimate ϵ_{Soil} robustly. Initially, a value of ϵ_{Soil} is assumed and the algorithm is performed to detect the pipe orientation. Now that the pipe orientation is known with good confidence, Rx can move in a line perpendicular to the pipe axis, which includes the fixed Tx. In this case, the pipe will behave as a point target (i.e., the scattered field will reach all Rxs from a single scattering phase center). To illustrate, (3.6) can be used

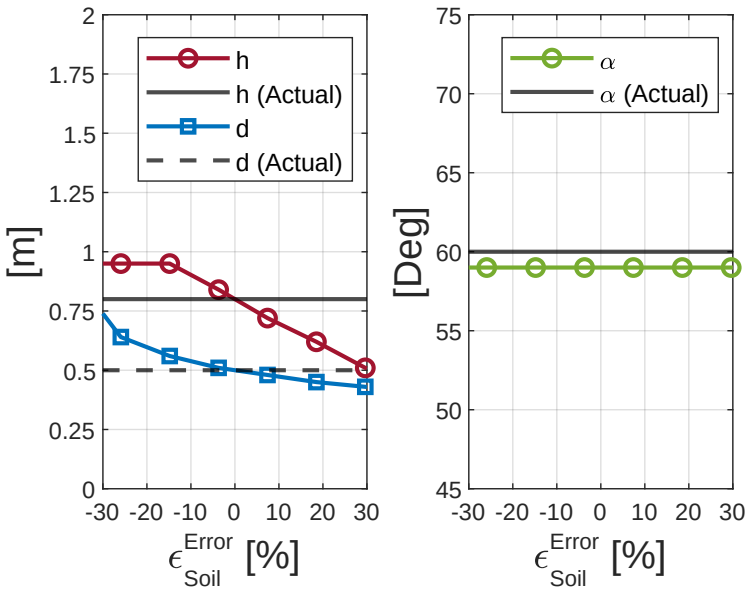


Figure 3.8: Parameters estimation versus background permittivity error.

with $z'_{on} = 0$. Now that the pipe is behaving like a point target, the BP algorithm can be applied while varying ϵ_{Soil} until the best focus is achieved. This will provide a more accurate value for ϵ_{Soil}. It is also possible to use the proposed algorithm for estimating ϵ_{Soil} but since the proposed algorithm is not as sensitive to errors in ϵ_{Soil}, using BP leads to better results. To demonstrate, both the proposed algorithm and the BP algorithm are performed for different values of ϵ_{Soil} and the highest peak for each ϵ_{Soil} is saved and plotted in Fig. 3.9. BP leads to a sharper peak at the correct ϵ_{Soil} compared to the less sensitive and more flat behavior for the peak obtained using the proposed algorithm. It should be noted that throughout the preceding discussion, only the real part of ϵ_{Soil} was of interest as it is what mostly determines the phase behavior; the imaginary part of ϵ_{Soil} leads mainly to signal attenuation, which is not the primary concern of the algorithm.

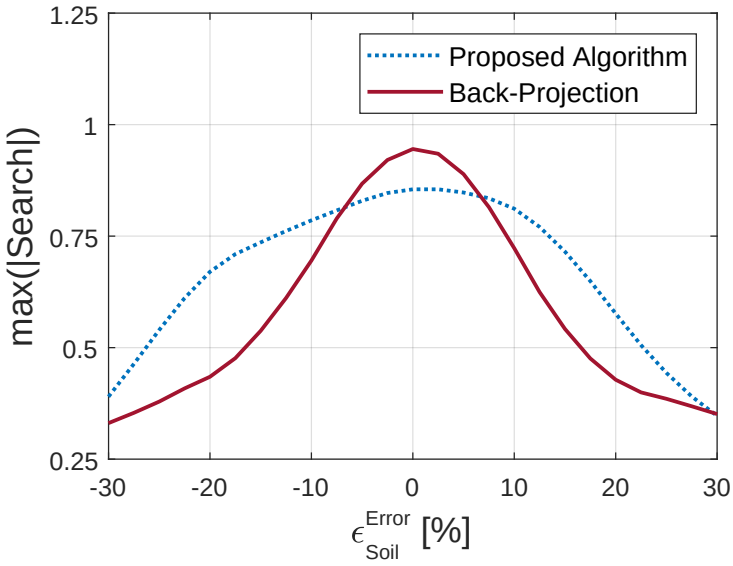


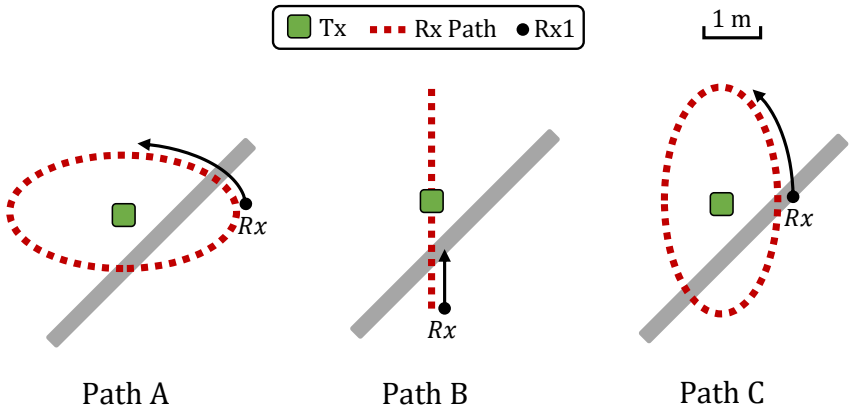
Figure 3.9: Peak of the search space Vs error in real background permittivity.

3.3.5 Time Domain Responses for Different Tx-Rx Arrangements

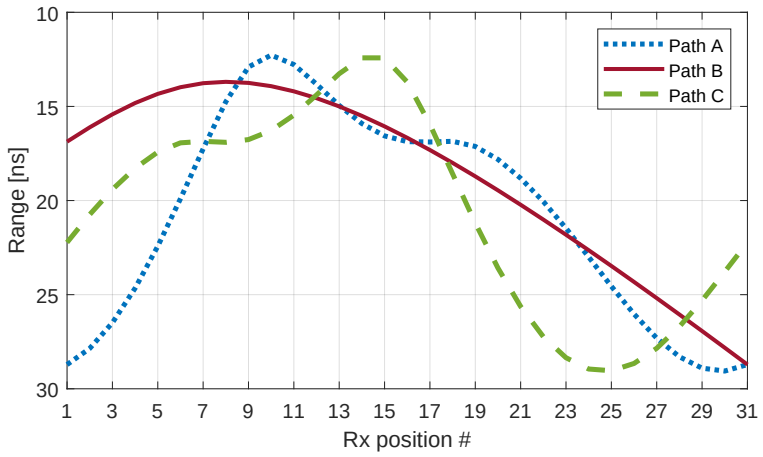
As mentioned in the introduction, one of the advantages of the proposed algorithm is its suitability to any multistatic Tx-Rx arrangement, compared to the hyperbola recognition approach which requires the arrangement to be a straight line when operating in a multistatic configuration. To illustrate, the range (in time) is plotted as a function of Rx positions using different Rx paths. Mathematically, the range is found by:

$$Range(Rx_n) = \frac{PL\,(Rx_n)}{c_{Soil}} \tag{3.12}$$

where $PL\,(Rx_n)$ is the signal pathlength obtained using (3.7) and c_{Soil} is the wave speed inside the soil. Choosing soil with a dielectric constant of 5 and a pipe at 0.5-m depth, three Tx-Rx arrangements are considered (Fig. 3.10a) and their resulting range is plotted in Fig. 3.10b. For the straight path (Path B), the result is the usual hyperbola with the minimum shifted because the path is not centered around



(a)



(b)

Figure 3.10: Rx paths used (a) and the resulting range as a function of Rx positions (b), the pipe is buried at 0.5 m depth.

the pipe. However, when the path is changed to an arbitrary one like the vertical and horizontal ellipsis in paths C and A, the resulting range profile is no longer a hyperbola and the pipe may not be detectable using hyperbola recognition, in contrast to the proposed algorithm that accounts for the signal pathlength for any multistatic Tx-Rx arrangement.

3.4 Simulation and Measurement Results

Now that the main assumptions in the algorithm derivation have been justified, this section demonstrates the performance of the algorithm for realistic scenarios of buried pipes in lossy background media using simulation as well as actual measurements.

3.4.1 Simulation

Full-wave analyses based on FEKO software are used to generate scattered-field data for two different scenarios of buried pipes. One case pertains to a metallic pipe with a 20-cm diameter and the other case is a PVC pipe, which is filled with water, having inner and outer diameters of 20 and 24 cm, respectively, with dielectric constants of $\epsilon_{PVC} = 3$ and $\epsilon_{Water} = 76.6 - j11.7$. A frequency band extending form 100 MHz to 500 MHz in 30 MHz increments is used for the stepped-frequency radar. Both Tx and Rx antennas are circularly polarized Hertzian dipoles located 10 cm above a lossy soil half space with $\epsilon_{Soil} = 10 - j1$. The Rx samples are located in three concentric circles of 1, 2, and 3m radii and less than $\lambda_{min}/2$ spacing, where λ_{min} is the wavelength at the highest frequency. The actual parameters for the metallic pipe are $(\alpha, d, h) = (45, -1.4, 0.75)$ and for the dielectric pipe are $(\alpha, d, h) = (45, 1.4, 0.75)$. Fig. 3.11 shows the results obtained by applying the algorithm to the scattered field part of the simulation data. Two local maxima in the search space are shown (the brighter one indicates the strongly scattering metallic pipe). This shows that

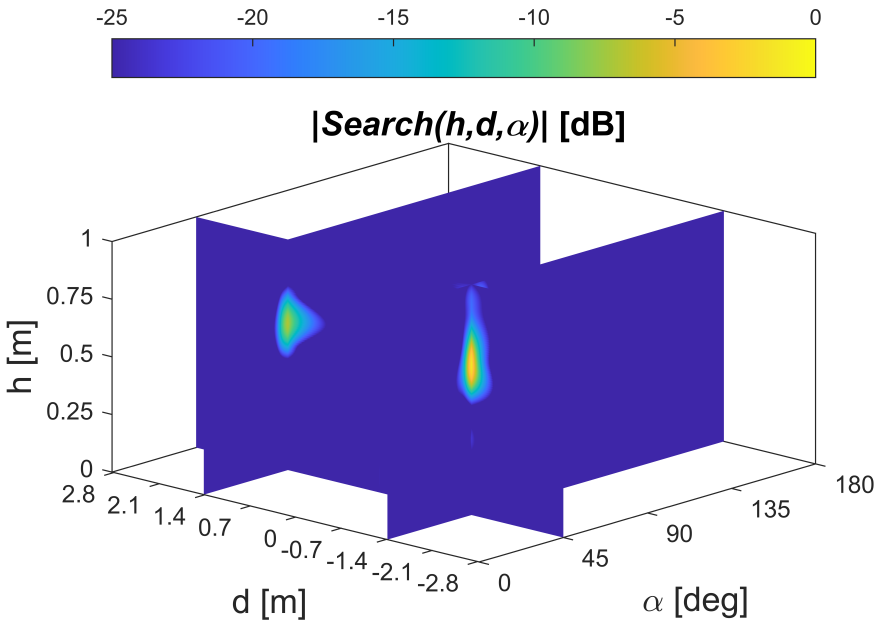


Figure 3.11: The search space of the algorithm when applied to simulation data of a metallic and dielectric pipes.

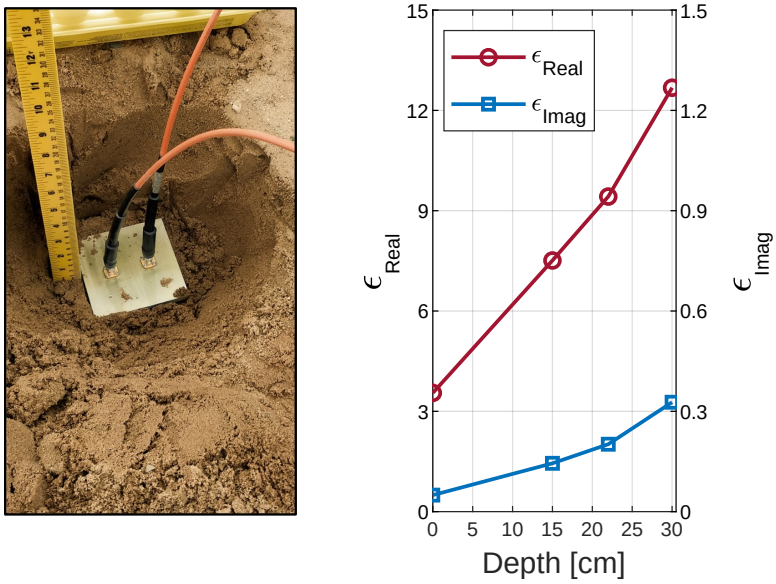
the algorithm is able to detect both metallic and dielectric pipes, even under lossy background conditions. It should be emphasized that the metallic and dielectric pipes are far enough apart so that their mutual interaction is negligible.

3.4.2 Measurements

A realistic sandy environment at Silver Lake Recreation Area in Pinckney, Michigan in the USA was chosen to conduct the experiments (see Fig. 3.12). Using a portable vector network analyzer (VNA) and a dielectric probe based on a ring resonator proposed and discussed in [87], the dielectric profile of the sand as a function of depth was measured on site. Fig. 3.13 shows the ring resonator and the measured dielectric profile of the sandy environment used for experimentation. Because the soil moisture increased with depth, so did the dielectric profile. After determining the sand permittivity, two experiments were conducted, one for a metallic pipe and the



Figure 3.12: Measurement place near Silver Lake in Pinckney, Michigan.



(a) (b)

Figure 3.13: (a) The ring resonator used at different depths (b) the resulting sand dielectric profile.

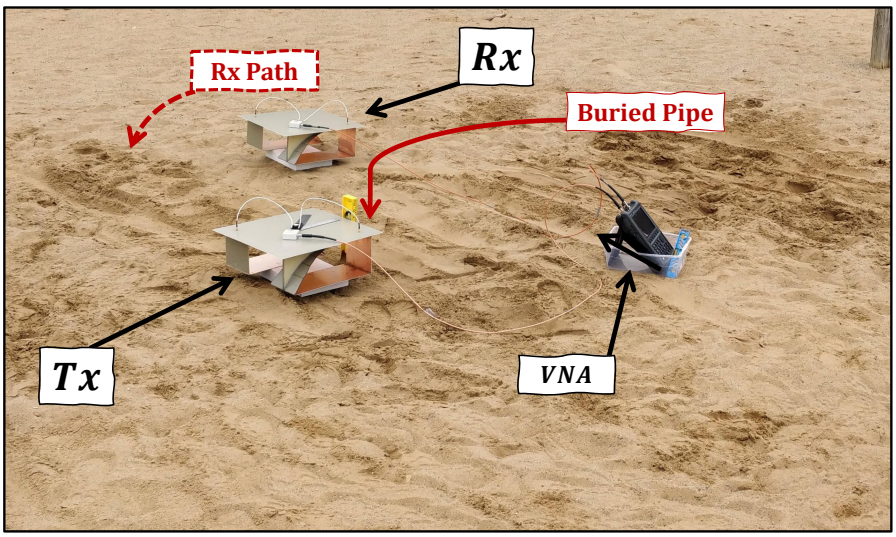


Figure 3.14: The VNA based multistatic subsurface SAR Setup A used in the two experiments.

other for a PVC pipe filled with water. Two experimental setups were used in the two experiments, one setup includes the signal leakage from the Tx to the Rx while the other blocks it. The first setup is shown in Fig. 3.14 and the second setup is shown in Fig. 3.15. There is a fixed Tx antenna placed in the middle of the scene and an Rx antenna is moved on circles concentric around the Tx. A VNA is used to measure the S_{21} data each time the Rx is moved to a new position with the samples taken across the frequency range 100 MHz to 500 MHz in 16 MHz increments, providing enough unambiguous range inside the sand medium. Both Tx and Rx antennas are out-of-phase fed ENVELOPE antennas designed for subsurface radars as proposed in [78]. The delay caused by the coaxial lines connecting the antennas to the VNA is measured and accounted for by processing S_{21} data. Generally speaking, three main signals are received by Rx of the bi-static subsurface radar system, which are the direct signal from the Tx, the ground reflection signal, and the buried target signal. Direct and ground reflection signals attenuate proportional to $1/r^2$, but the sum attenuates proportional to $1/r^4$ since Tx and Rx are very close to the ground, making ground reflection almost canceling the direct signal as discussed in [88]. However, the direct

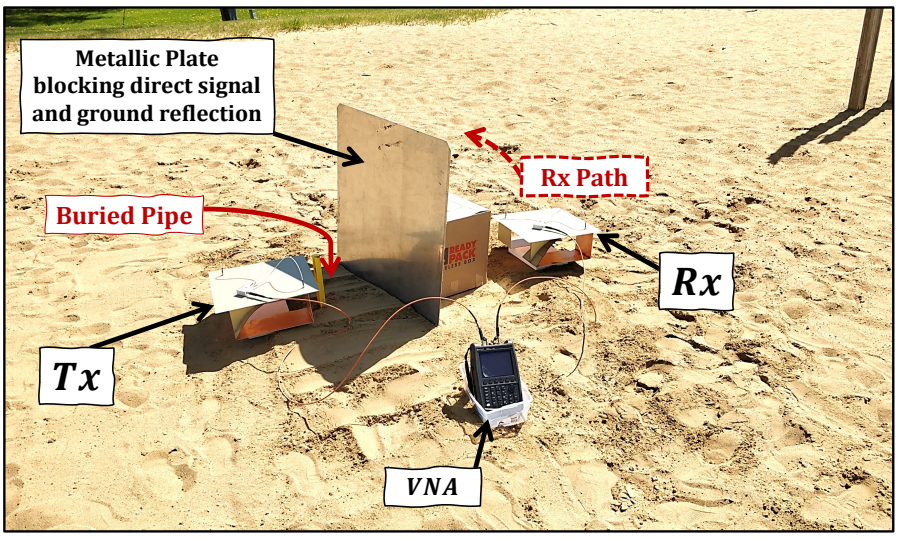
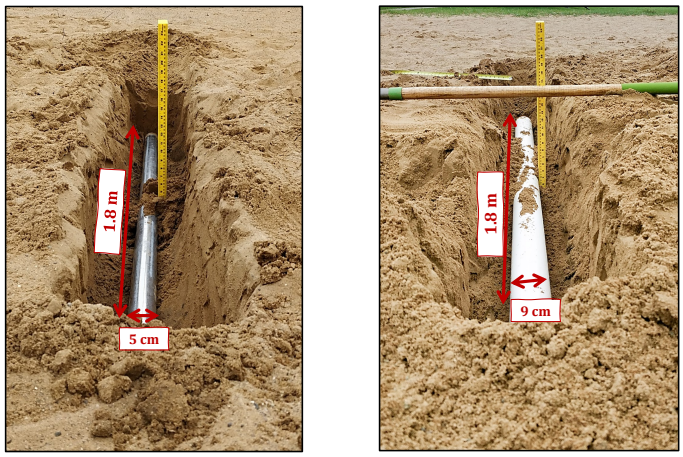


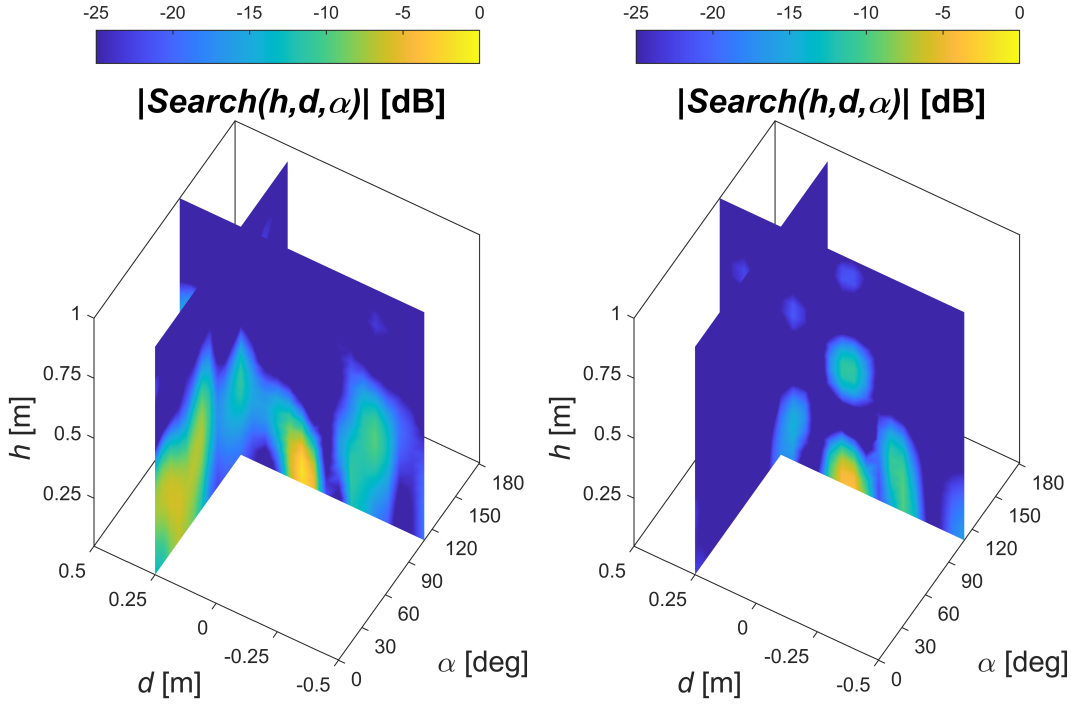
Figure 3.15: The VNA based multistatic subsurface SAR Setup B used in the two experiments. Compared to Setup A in Fig. 3.14, there is a metallic plate inserted between the Tx and Rx to reduce Tx-Rx coupling and ground reflections.

signal can still be much stronger than the scattered signal from the pipe because the pipe signal suffers exponential attenuation from the lossy soil, in addition to the $1/r^4$ propagation loss. This fact hinders the radar's ability to detect weak targets. To alleviate this problem, a metallic plate (Fig. 3.15) is placed between Tx and Rx and tilted slightly to scatter the direct and the ground reflection signals away from the Rx, making the buried target signal more discernible. Using Setup A and Setup B, a 1.8-m long metallic pipe with 5-cm diameter (Fig. 3.16a) and a 1.8-m long water-filled PVC pipe (Fig. 3.16b) with 9-cm diameter were buried in sand with the following parameters $(\alpha, d, h) = (110, 0.25, 0.45)$. For Setup A, the Rx samples are taken on a circular paths with 1.5-m radius and having 36 samples to ensure less than $\lambda_{min}/2$ spacing among the samples. After that, the collected S_{21} data is processed to eliminate cable delay, then it is used in (3.10) as V^{nm} to fill in the search space. The detection results using Setup A are shown in Fig. 3.17. For both metallic and PVC pipeline cases, a strong peak is shown around zero depth, not at the actual pipelines parameters. This peak represents the direct Tx-Rx coupling and the ground reflection



(a) Metallic (b) Water filled PVC

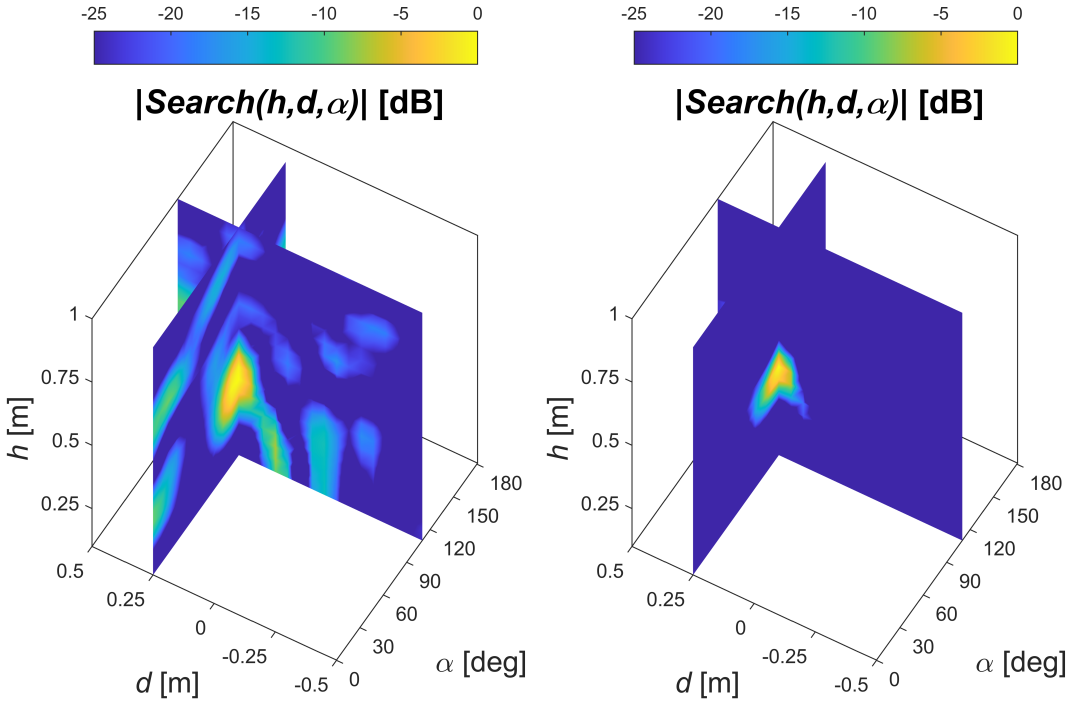
Figure 3.16: The buried pipes used in the experiment.



(a) Metallic Pipeline. (b) Water-filled PVC Pipeline.

Figure 3.17: The magnitude of the search space obtained from the metallic and PVC pipes measurements using Setup A. A strong peak is shown near zero depth indicating the direct Tx-Rx coupling signal.

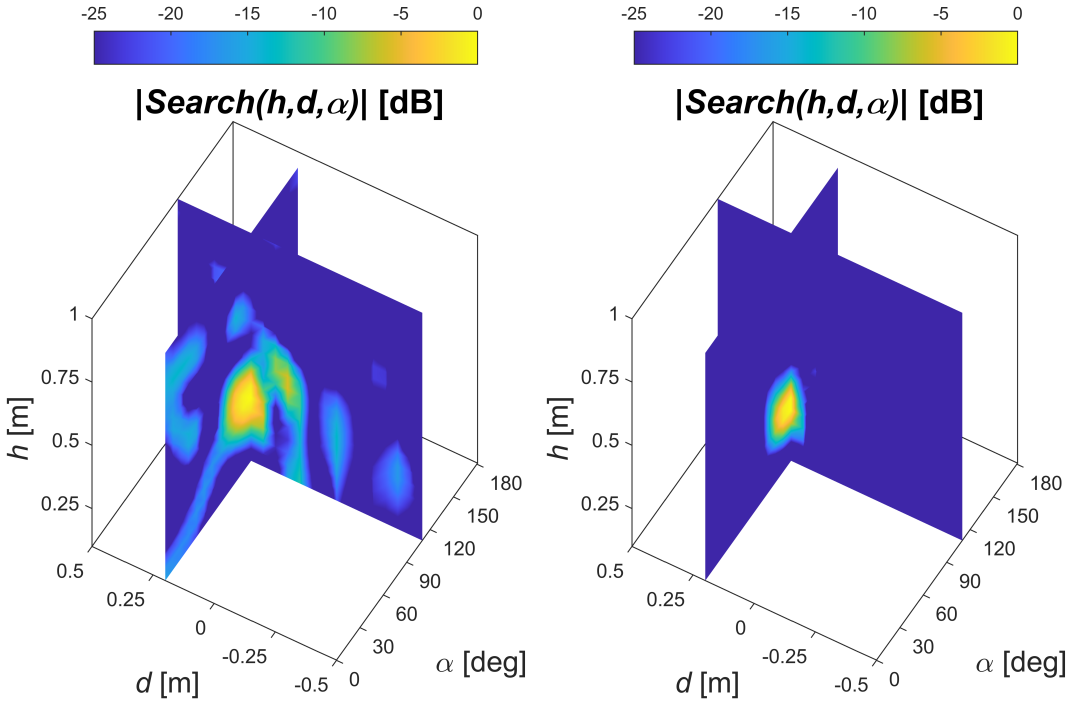
signals obscuring pipelines detection. To address this issue, Setup B with a metallic plate reducing such leakage signals is used instead of Setup A. Using setup B, Rx samples are taken on three circular paths with radii of 1.25,1.5 and 1.75 meters with each circle having 36 samples. Next, the collected signals are used in (3.10) as V^{nm} to fill in the search space. To get a sharper detection peak, it is better to apply (3.10) for each circle and construct the search space individually. After that, the search spaces for all three circles are multiplied together to remove noisy peaks and conserve the peak associated with the pipeline. Fig. 3.18a shows the magnitude of the signal in the search space using the 1.25 m circle only and Fig. 3.18b shows the magnitude of the signal in the search space when constructed using the product of the 1.25, 1.5, 1.75 m circles. As can be seen, using Setup B allows the algorithm to detect the pipe even when using a single circle because the direct coupling has been reduced by the metallic plate. Moreover, using multiple circles leads to a more robust peak detection. Using setup B with the exact settings for the metallic pipe, the water-filled PVC pipe measurements are used in the algorithm. Similar to the metallic pipe case, Fig. 3.19a shows the peak in search space using one circle while Fig. 3.19b shows the product of the peak in the search spaces for the three circles. Here a sharp peak is observed that is more than 20 dB above the rest of the search space, indicating the ability of the algorithm to also detect and localize dielectric pipes, so long as the direct Rx-Tx coupling and ground reflections are mitigated. In both cases of metallic and PVC pipes, the background dielectric used in the algorithm is obtained using the dielectric estimation method proposed in the previous section, which led to $\epsilon_{Sand} = 7.5$. This value is consistent with the mean value of the real part of the dielectric profile given in Fig. 3.13b.



(a) Single circle.

(b) Product of 3 circles.

Figure 3.18: The magnitude of the search space obtained from the metallic pipe measurements using Setup B. The use of the metallic plate repressed the direct coupling and ground reflections allowing for the detection and localization of the buried metallic pipe.



(a) Single circle.

(b) Product of 3 circles.

Figure 3.19: The magnitude of the search space obtained from the water filled PVC pipe measurements using Setup B. The use of the metallic plate repressed the direct coupling and ground reflections allowing for the detection and localization of the buried water filled PVC pipe.

3.5 Conclusion

In this chapter, a novel pipe detection and localization algorithm using a multistatic subsurface SAR is proposed. The algorithm works by taking into account the unique scattering mechanism of pipelines and provides a phase compensation scheme tailored to it. By summing the compensated signals coherently across all receivers and frequencies, the actual pipeline depth, the horizontal displacement, and the orientation are revealed. The algorithm is derived based on the physics of the pipeline scattering phenomena and different aspects of the derivation are investigated. Finally, the algorithm's ability to detect both metallic and layered dielectric pipelines is demonstrated by applying it to the scattered field data of pipelines buried in a realistic lossy soil environment using simulation as well as actual measurements. As a focusing based algorithm, the algorithm is expected to have finite range and cross range resolutions in detection and localization. This makes the algorithm suitable for detection and localization of a single buried pipeline, or a collection of buried pipelines with large separation between them. The next chapter tackles the general problem of detection and localization of closely spaced buried pipelines that may fall below the resolution limits of the algorithm proposed in this chapter.

CHAPTER 4

Detection and Localization of Closely-Spaced Buried Pipelines

4.1 Introduction

As was illustrated in the preceding chapter (Chapter 3), the challenge of focusing SAR signals of buried pipelines, given their dynamic scattering phase centers which move as a function of the Rx position, can be addressed by devising a new SAR phase-compensation (focusing) algorithm suited specifically to pipeline geometries, leading to their detection and localization in multistatic SAR. This focusing-based procedure entails finite resolutions along the range and cross-range directions. This makes the algorithm in Chapter 3 suitable for detection of a single pipeline or a collection of pipelines with large-enough separations between them. When the pipelines are too close, the algorithm may not be able to resolve the pipes. To address this limited-resolution challenge, a new algorithm that relies on both the phase and amplitude of the pipelines' scattered field is proposed in this chapter. The basic idea of the algorithm is to utilize a 3D forward scattering model for buried pipelines in multistatic SAR to define an objective function whose minimization leads to detection and localization of closely spaced buried pipelines. The rest of the chapter is organized as follows. Section 4.2 starts with developing the forward scattering model for multiple buried pipelines in 3D multistatic SAR and moves to explain the dynamic grid search

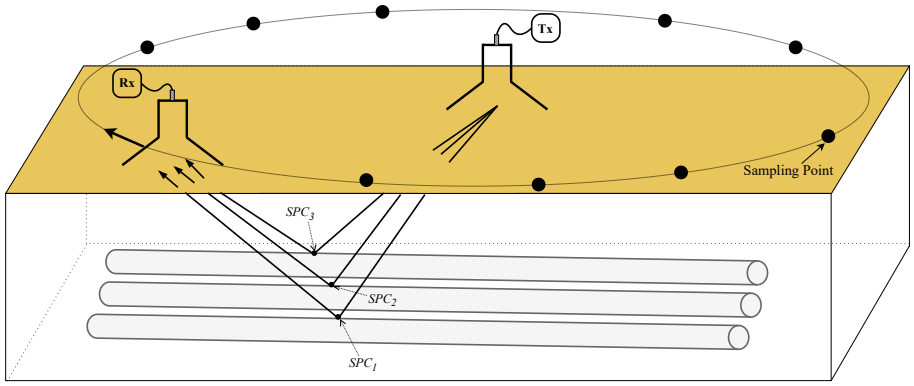


Figure 4.1: Multistatic subsurface SAR system. There is a fixed transmitter (Tx) illuminating the underground and a moving receiver (Rx) that samples the scattered field around the Tx. It is noted that unlike point targets that have a fixed scattering phase center, pipelines have dynamic scattering phase centers that depend on the Rx position relative to the Tx.

based minimization algorithm used for detection and localization of closely-spaced pipelines. Section 4.3 provides a numerical analysis for some of the approximations made in the forward model derivation and Section 4.4 provides a comprehensive numerical and experimental evaluation of the performance of the novel dynamic grid search algorithm.

4.2 Closely-Spaced Buried Pipelines Detection and Localization Algorithm

The geometry of the problem under consideration is shown in Fig. 4.1. This figure shows multiple pipelines buried in a half-space dielectric medium with the pipes' axes parallel to the half-space interface. The transmitter (Tx) and receiver (Rx) antennas are assumed to be very close and matched to the half-space so that the antenna can be assumed to radiate plane waves in different directions inside a single medium. The forward scattering model and inversion algorithm for a single pipeline in a subsurface multistatic SAR configuration has been discussed in detail in Chapter 3, and they will

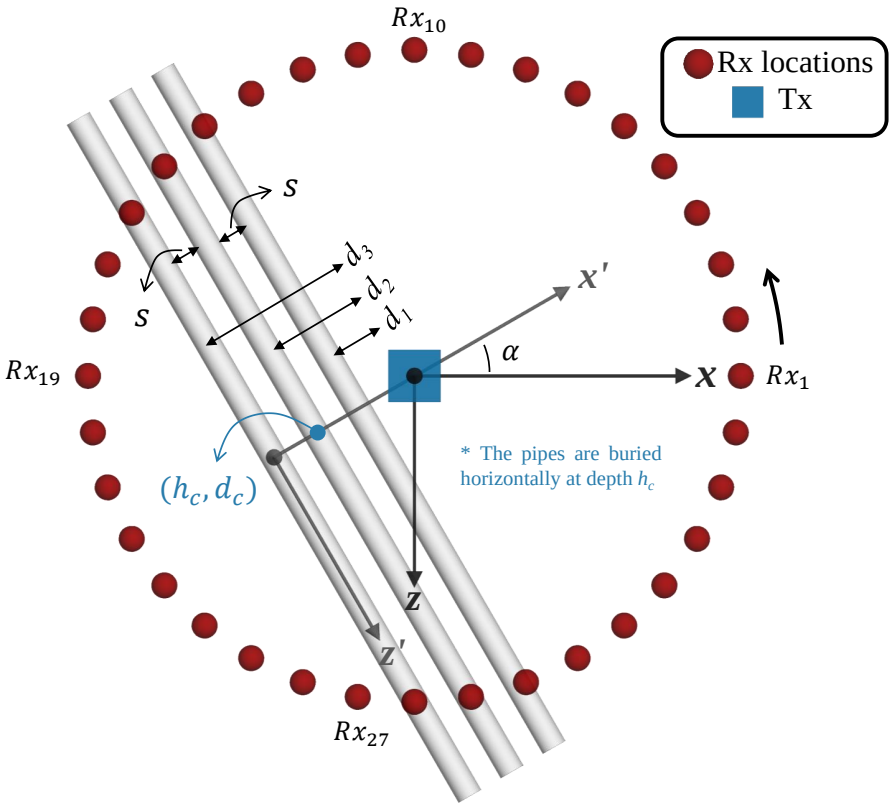


Figure 4.2: Top view of the coordinate systems (the global and the primed one along one of the pipes) and the subsurface SAR configuration. The pipes have the same depth h_c with varying displacements determined by the spacing s. For vertically buried pipes the displacement will be d_c and the depths will be varying. Displacement direction is from the Tx location to a specific pipes' center.

be discussed briefly again in the following subsections to facilitate the derivation of the scattering model and inversion algorithm for the general case of multiple buried pipelines using multistatic subsurface SAR.

4.2.1 Forward Scattering of A Single Pipeline

For $e^{j\omega t}$ time dependence and plane wave incidence at an angle θ_i with respect to the pipeline axis (z-axis), the analytical expression for the scattered field of a pipeline in the far-field can be written as:

$$\boldsymbol{E^s} \approx \boldsymbol{A}(\rho, \phi, \theta_i)\, e^{-j(k\, cos\theta_i z + k\, sin\theta_i \rho)} \tag{4.1}$$

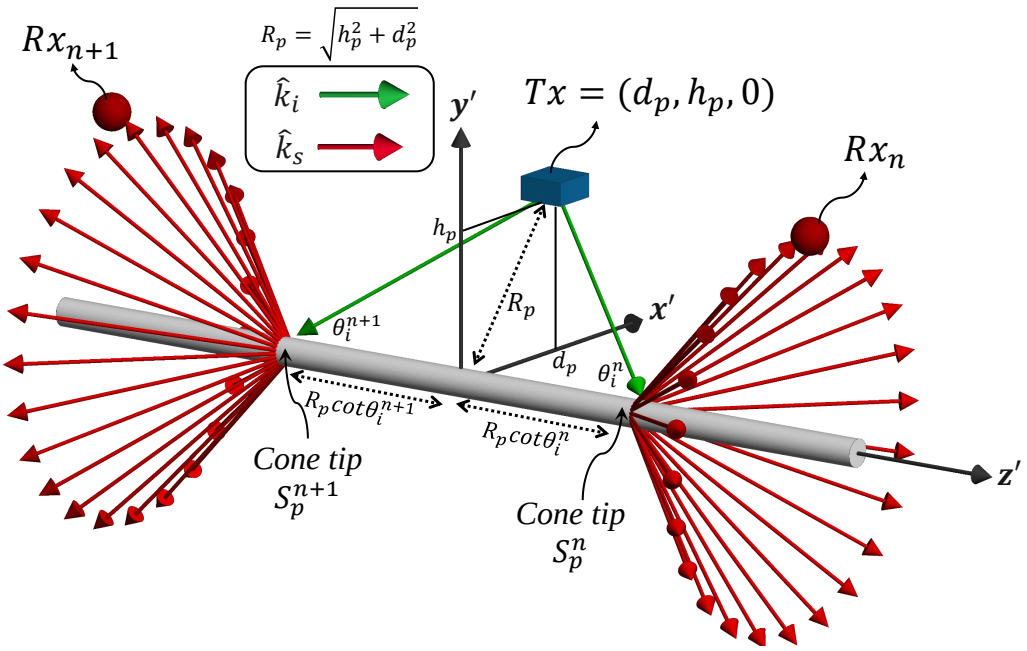


Figure 4.3: The primed local coordinates along an arbitrary pipe p of depth h and displacement d from the Tx. Only two cones are shown for illustration. Each Rx has a unique cone and SPC (the cone tip). The same applies for the other pipes.

where $k_\rho = k\,sin\theta_i$, $k_z = k\,cos\theta_i$ and k is the wave number for the background medium. The vector $\boldsymbol{A}$ specifies the components of the scattered field that satisfy the boundary conditions for TE^z and TM^z modes and can be found analytically for various types of pipes [79, 80, 81, 82, 83]. The exponential term in (4.1) indicates that the scattered field propagates along a surface of a cone until reaching a specific Rx location. The Tx antenna typically has a wide beam resulting in the generation of multiple scattered field cones (i.e., a cone for each possible wave incidence at θ_i as illustrated in Fig. 4.3). The cone tip for a wave coming at an angle θ_i is the location of the scattering phase center (SPC) for the particular Rx location that happens to intersect with the θ_i cone. To find the particular θ_i^n for the n^{th} Rx location (hence the cone tip and the SPC), suppose the pipe's orientation angle is α, and its displacement and depth with respect to the Tx are d and h, respectively (see Fig. 4.2). In the primed coordinate system whose z-axis is along the pipeline (Fig. 4.3), the solution for θ_i^n is found to be (see Chapter 3):

$$\theta_i^n = \arctan\left(\frac{\sqrt{h^2 + x_{on}'^2(\alpha, d, h)} + \sqrt{d^2 + h^2}}{z_{on}'(\alpha, d, h)}\right) \tag{4.2}$$

where ($z_{on}^{'}$,$x_{on}^{'}$) are the coordinates of the Rx location in the pipeline coordinate system. These coordinates are functions of (α, d, h) parameters. Having found θ_i^n, the SPC coordinate is given by $S^n = (0, 0, \sqrt{d^2 + h^2}\,cot\theta_i)$. From S^n, the total bistatic signal pathlength, which consists of two segments, can be calculated. The first segment is R_{Tx-S^n}, the distance from the Tx to the SPC and the second segment is $R_{S^n-Rx_n}$, the distance from the SPC to the n^{th} Rx location. Knowing the pathlength allows for predicting the phase behavior, which leads to the detection of the pipeline, as will be shown in Subsection 4.2.3

4.2.2 Forward Scattering of Multiple Pipelines

To model the scattering behavior of multiple pipelines, both the amplitude and phase of the scattered field from the pipelines need to be accounted for. To do that, the knowledge of the SPC of each pipeline for each Rx location is utilized to form the forward model. For a collection of Np pipelines oriented at α, arranged in a horizontal or vertical plane ($ar = 1, 2$) with their center at (h_c, d_c) and spacing of s (see Fig. 4.2), the forward model (FM) of the received voltage at the m^{th} frequency and n^{th} Rx location is given by:

$$FM_{mn}(ar, N_p, d_c, h_c, s) = \sum_{p=1}^{N_p} P_{Tx}^{m} \times P_{Rx_n}^{m} \times \frac{e^{-jk_m(R_{Tx-S_p^n} + R_{S_p^n - Rx_n})}}{R_{Tx-S_p^n} \times R_{S_p^n - Rx_n}} \tag{4.3}$$

Here, P_{Tx} refers to the Tx antenna radiation pattern that implicitly depends on $(\phi_p^{Tx}, \theta_p^{Tx})$, the coordinates of the SPC of the p^{th} pipe as seen by the Tx spherical coordinate system centered at the Tx antenna centroid. The same applies to P_{Rx_n}, the Rx antenna radiation pattern that depends implicitly on $(\phi_p^{Rx_n}, \theta_p^{Rx_n})$, the coordinates of the p^{th} pipe's SPC as seen by the spherical coordinates system centered at the Rx antenna centroid at the n^{th} Rx location. Furthermore, the path in the exponent $(R_{Tx-S_p^n} + R_{S_p^n - Rx_n})$ accounts for the propagation phase and attenuation due to loss in the medium, while the product $R_{Tx-S_p^n} \times R_{S_p^n - Rx_n}$ in the denominator accounts for the attenuation due to the spherical propagation of the waves emitted by the Tx. Depending on the arrangement and the spacing (ar and s), the values of the depth h_p and displacement d_p of the p^{th} pipeline can be obtained from:

$$d_p = \begin{cases} d_c + (p - \frac{N_p+1}{2}) \times s & ar = 1 \\ d_c & ar = 2 \end{cases} \tag{4.4}$$

$$h_p = \begin{cases} h_c + (p - \frac{N_p+1}{2}) \times s & ar = 2 \\ h_c & ar = 1 \end{cases} \tag{4.5}$$

where (d_c, h_c) is the centroid of the collection of pipes. This forward model is to be used to minimize an objective function leading to the detection and localization of the multiple buried pipelines as will be discussed in the following subsection (4.2.3).

4.2.3 Inversion Algorithms

Given the received voltage $\{V_{mn}\}$ at each Rx location and frequency, in addition of the precise knowledge of the Tx and Rx locations, the aim of the inversion algorithm is to determine the parameters (α, h, d) (i.e., orientation, depth and displacement) of each buried pipeline. One way to go about finding the parameters is to define the following basic focusing search as was done in Chapter 3:

$$Search(\alpha, d, h) = \sum_{m=1}^{M} \sum_{n=1}^{N} V_{mn} e^{j\left(k_m(R_{Tx-S^n} + R_{S^n-Rx_n})\right)} \tag{4.6}$$

This search simply compensates for the phase of a pipeline with parameters (α, h, d) across all Rx locations and frequencies, then sums the results coherently. The process can be repeated for many values of each possible parameter (α, h, d), and then the sum is maximized at the actual pipeline parameters as illustrated in the algorithm in Fig. 4.4. This approach works fine if there is only a single buried pipeline. However, when there are multiple pipelines, especially closely spaced ones, the algorithm will no longer be able to separate them. This is because the algorithm is a focusing-based algorithm which entails limited range and cross-range resolutions (wide full-width at half maximum of $|Search(\alpha, d, h)|$). Moreover, due to its relatively stronger scatter-

Algorithm I Basic focusing based pipelines detection

Input: $\{V_{11}, \dots, V_{MN}\}, \{(x_{o1}, z_{o1}), \dots, (x_{oN}, z_{oN})\}$,
$\{(\alpha_1, d_1, h_1), \dots, (\alpha_K, d_K, h_K)\}$,

For *k=1 to K* **Do**

- Transform (x_{on}, z_{on}) into (α_k, d_k, h_k) coordinates $\forall n$
- Solve for θ_i^n $\forall n$
- Calculate R_{Tx-S^n} and $R_{S^n-Rx_n}$ $\forall n$
- Compensate for the pipeline phase and do a coherent sum
- Save the sum in $Search(\alpha_k, d_k, h_k)$

End

$$(\alpha, d, h)_{Actual} = \underset{(\alpha,d,h)}{\operatorname{argmax}} |Search(\alpha, d, h)|$$

Figure 4.4: Basic phase compensation (focusing) algorithm for finding single pipeline or widely spaced pipelines parameters proposed in Chapter 3.

ing, the pipeline closest to the Tx will have a strong peak that may overshadow the peaks associated with the other pipelines. To overcome this limitation, the following objective function can be defined:

$$J(ar, N_p, d_c, h_c, s) = \sum_{m=1}^{M} \sum_{n=1}^{N} |V_{mn} - a_m \, FM_{mn}| \tag{4.7}$$

where a_m is a normalization factor that brings the forward model signal level to the received signal level for each frequency. This objective function represents the misfit between the measured voltage data $\{V_{mn}\}$ and the predicted scattering behavior for a collection of pipelines with parameters (ar, N_p, d_c, h_c, s). When the pipelines parameters match the actual ones, the objective function is expected to be minimized, leading to detection and localization of multiple closely spaced pipelines. This objective function has 5 parameters. To minimize it in a computationally efficient manner, a dynamic grid search algorithm is applied to it. The dynamic grid search algorithm loops over all the discrete values of the parameters ar and N_p as well as the spacing s, which has a limited range. To search for the pipelines collection centroid (d_c, h_c),

the algorithm in Fig. 4.4 is applied first and the resulting peak in $|Search(\alpha, d, h)|$ is used to determine the pipelines orientation α as well as an initial estimate of (d_c, h_c). This is because for closely spaced pipelines that are not resolved by the basic search, a single peak will appear within the spatial extent of the pipelines collection. After obtaining an initial estimate, a dynamic search window is applied based on the number of pipes N_p and their arrangement ar. This means that for horizontally (vertically) buried pipes, the window will extend around the d_c (h_c) dimension, where the extent is determined based on the number of assumed pipes N_p and the spacing s. The algorithm steps are summarized in Fig. 4.5 and the associated MATLAB code is found in Appendix. B.

4.3 Numerical Analysis

In the derivation of the forward model, several approximations have been made to reach the final result. One approximation is that the pipelines are in the far-field of the Tx and Rx antennas and vise versa. Another approximation involves ignoring the scattering phase contribution from the vector $\boldsymbol{A}$ in (4.1) and using only the propagation phase term. These two approximations have been discussed in detail in Chapter 3 and will not be discussed here. Aside from these approximations, the forward model assumes the antennas to be very close to the soil surface and matched to it, allowing for the approximation that the pipelines are buried in a uniform medium instead of the real scenario of an air medium above a soil half-space medium. Additionally, the forward model is a first order scattering model that ignores multiple scattering among pipelines and any possible shadowing effects. This section discusses the impact of the uniform-medium assumption and the discarding of higher-order scattering mechanisms. The numerical analysis and simulations throughout this chapter use one of the three representative soil media summarized in Table 4.1, where the water content

Algorithm II Dynamic grid search based pipelines detection

Input: $\{V_{11}, \dots, V_{MN}\}, \{(x_{o1}, z_{o1}), \dots, (x_{oN}, z_{oN})\}$, $\max(N_p)$, $\max(s)$, δs, δd, δh

Do a search using **Algorithm I** to get the pipelines orientation α and an initial estimate of (h_c, d_c) i.e (h_c^0, d_c^0)

For $ar = [1,2], N_p = [1, \max(N_p)]$ **Do**
- **For** $s = [0, \max(s)]$ **with** δs spacing **Do**
  - **If** ar=1
    - $h = s$, $d = \frac{N_p}{2} s$
  - **Else**
    - $d = s$, $h = \frac{N_p}{2} s$
  - **End**
  - **For** $h_c = [-h, h] + h_c^0$ **with** δh spacing **Do**
    - **For** $d_c = [-d, d] + d_c^0$ **with** δd spacing **Do**
      - Calculate and store $J(ar, N_p, h_c, d_c, s)$
    - **End**
  - **End**
- **End**

End

$$(ar, N_p, h_c, d_c, s) = \underset{(ar, N_p, h_c, d_c, s)}{\operatorname{argmin}} J(ar, N_p, h_c, d_c, s)$$

Figure 4.5: Novel dynamic grid search algorithm for finding multiple closely spaced pipelines parameters.

is obtained from the survey in [89] and the dielectric constants are calculated using Code 4.7 provided in [86].

Table 4.1: Soil Media Used in Simulations and Numerical Analysis

Soil Type	**Composition (Sand, Slit, Clay)**	**Relative Permittivity**	**Water Content**
Sand	(96%,2%,2%)	$4.35 - j0.3$	1%
Loam	(12%,44%,44%)	$6.1 - j2.1$	10%
Clay	(2%,41%,57%)	$15.5 - j6$	30%

4.3.1 Uniform Medium Assumption

The reason for neglecting the half-space interface and treating the Tx and Rx antennas as if they were radiating and receiving through a uniform medium is based on the fact that when the antennas are placed very close to the soil interface and matched to it, the propagation phase goes mostly through the soil and only the amplitude radiation patterns of the antennas are effected by the interface presence. To demonstrate the validity of this assumption, the radiation patterns of the antennas can be obtained by simulating the antennas above a soil medium using a full-wave simulation. In this way, the effect of the air-soil interface becomes included in the radiation patterns in (4.3). To test this approach, Altair FEKO simulation software is used to generate full-wave scattered-field data of two Perfect Electric Conductor (PEC) pipelines of 10-cm diameter buried in a half-space dielectric medium. The Tx-Rx configuration is the same as the circular one shown in Fig. 4.2, with the circle having 3.2-m diameter. The two pipes are at 1-meter depth and oriented along the z-axis and placed at 0.5 and 1 meter along the x-axis (i.e $d_1 = -0.5m, d_2 = -1m, \alpha = 0, h_c = -1m$). The antennas used for Tx and Rx are Hertzian dipoles oriented along the z-axis and placed 5 cm over the half-space consisting of air and a sand medium as in Table 4.1. The forward model is then used to find the scattered field to be compared with the full-

wave solution. The forward model is used twice. One time, the radiation patterns of the dipoles are obtained with analytical expressions for a dipole in a uniform medium [90] and the other time the full-wave simulation is used to find the radiation patterns of the dipoles when placed above the half-space. The comparison results for the received voltage values for different Rx locations at 300 MHz frequency (the central frequency of the radar used in this work) are shown in Fig. 4.6. The comparison shows that when calculating the radiation patterns assuming a uniform medium, noticeable deviations in amplitude from the full-wave data are observed. However, when using the radiation patterns of a dipole above the half-space, the amplitude deviations are no longer observed and excellent agreement is obtained between the forward model and the full-wave data. This supports the validity of approximating the half-space with a single medium, so long as the antennas are close to the half-space interface and their amplitude radiation patterns are obtained when they are placed above the half-space medium.

4.3.2 Efficacy of The First Order Scattering Assumption

To examine the efficacy of the first-order scattering model that ignores the mutual interactions among the pipelines, Altair FEKO simulation software is used to generate the full-wave scattered field data for two scenarios of arrays of pipelines that are buried horizontally and vertically. The medium of choice for both scenarios is the moderately lossy loam medium in Table 4.1, while the Tx-Rx configuration is the same as the one in Fig. 4.2 with 3.2-m diameter circle with the Tx and Rx antennas being Hertzian dipoles directed along the z-axis. For the horizontally arranged pipelines scenario, 4 standard-size 8.625-in (21.9-cm) diameter [91] PEC pipelines with 10-cm edge-to-edge spacing are chosen as a representative example of relatively large pipes in terms of wavelength inside the loam medium (about $\frac{\lambda}{2}$ diameter). The pipelines are buried at 80 cm depth below the Tx and oriented along the z-axis (i.e, $d_1 = -0.13m, d_2 =$

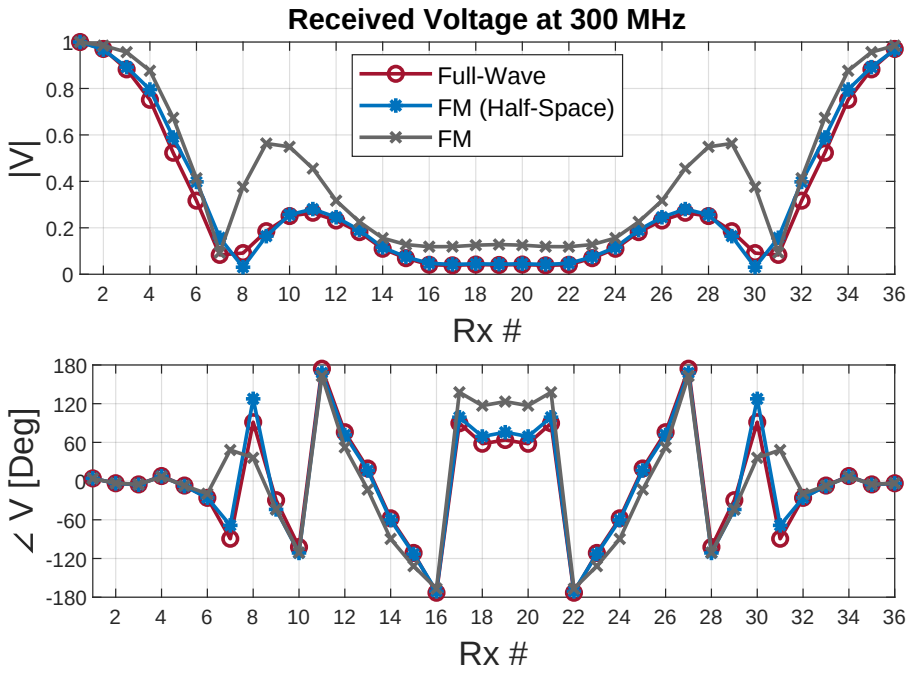


Figure 4.6: Received voltage values for different Rx locations obtained by full-wave simulation as well as using the forward model in (4.3) where the radiation patterns are calculated one time for a single medium - FM - and another time for half-space scenario - FM (Half-space). The data are for two 10 cm diameter PEC pipelines with $d_1 = -0.5m, d_2 = -1m, \alpha = 0, h_c = -1m$ (See Fig. 4.2).

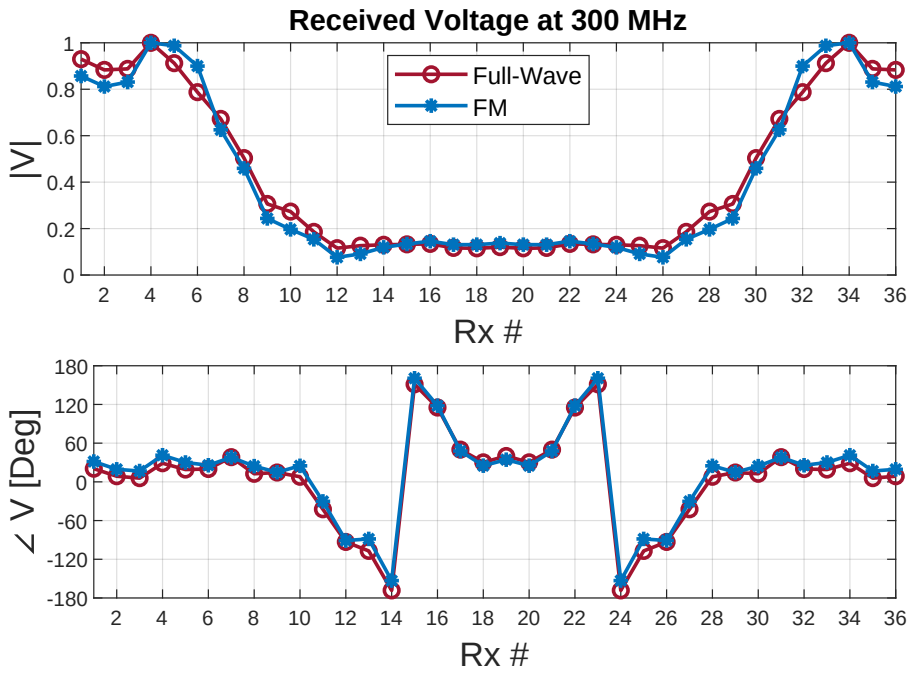


Figure 4.7: Received voltage values for different Rx locations obtained by full-wave simulation as well as using the forward model (4.3) at 300 MHz frequency. The data are for four PEC pipelines with $d_1 = -0.13m, d_2 = -0.44m, d_3 = -0.75m, d_4 = -1.06m, \alpha = 0, h_c = -0.8m$ (See Fig. 4.2) inside loam medium.

$-0.44m, d_3 = -0.75, d_4 = -1.06m, \alpha = 0, h_c = -0.8m$ in Fig. 4.2). The comparison results between the full-wave simulation and the forward model (4.3) are shown in Fig. 4.7. It is observed that the amplitude value is rather low for Rx locations 10-27, which is expected as these Rx locations are the farthest from the pipelines, making their scattered signals travel longer distances and hence experience more attenuation from the lossy loam medium. Aside from that, excellent agreement with full-wave data is observed with only slight deviations due to ignoring the mutual interactions among the pipelines. It will be shown in the performance evaluation section (Section 4.4) that such deviations do not prevent the cost function to be minimized at the correct parameter values, leading to successful detection and localization. The other scenario is for 3 vertically arranged dielectric pipelines with inner and outer layers. The inner layer material is water with dielectric constant of $80 - j20$ and standard diameter size

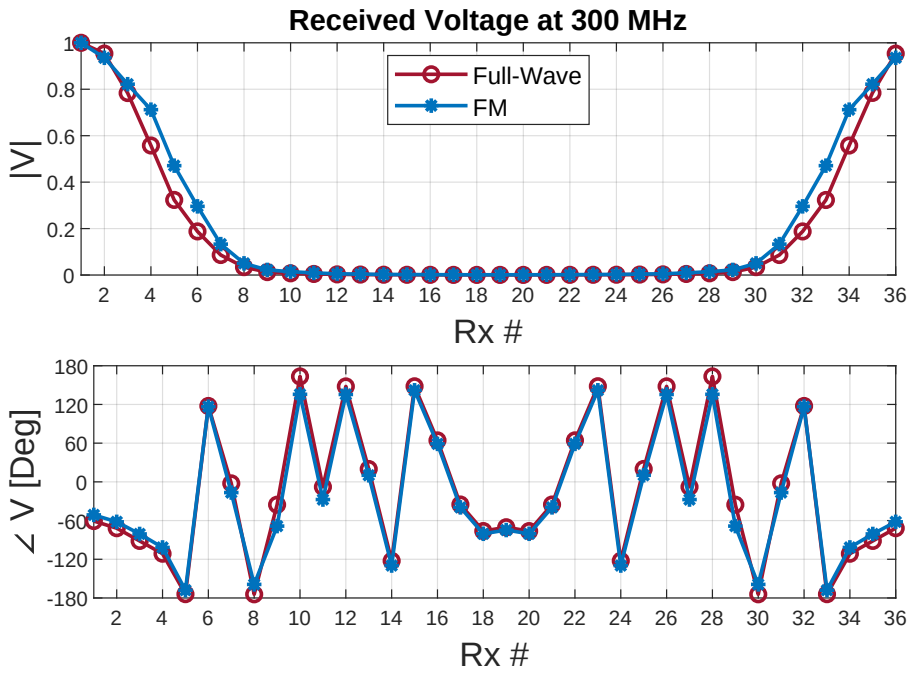


Figure 4.8: Received voltage values for different Rx locations obtained by full-wave simulation as well as using the forward model (4.3) at 300 MHz frequency. The data are for 3 dielectric pipelines arranged vertically with $h_1 = -0.75m, h_2 = -1m, h_3 = -1.25m, \alpha = 0, d_c = -1.25m$ (See Fig. 4.2) inside loam.

of 4-in (10.2-cm) [91] (about $\frac{\lambda}{4}$ inside loam). The outer layer represents a Polyvinyl chloride (PVC) material with dielectric constant of 3 and diameter of 10.204-cm. The 3 pipes are placed 1.25-m at the x-axis and oriented along the z-axis with 15-cm edge-to-edge vertical spacing (i.e, $h_1 = -0.75m, h_2 = -1m, h_3 = -1.25m, \alpha = 0, d_c = -1.25m$ in Fig. 4.2). Comparison between the full-wave simulation data and the forward model (4.3) at 300 MHz is shown in Fig. 4.8. Here, as in the PEC pipes case, a low amplitude is observed for Rx locations 10-27. Moreover, excellent agreement is obtained in comparison with full-wave data with slight overestimation in amplitude especially at Rx locations 1-6 and 31-36, which are the locations closest to the pipelines as can been seen in Fig. 4.2. This slight overestimation of amplitude by the forward model can mainly be attributed to the exclusion of the effects of shadowing. These deviations should not prevent successful detection and localization

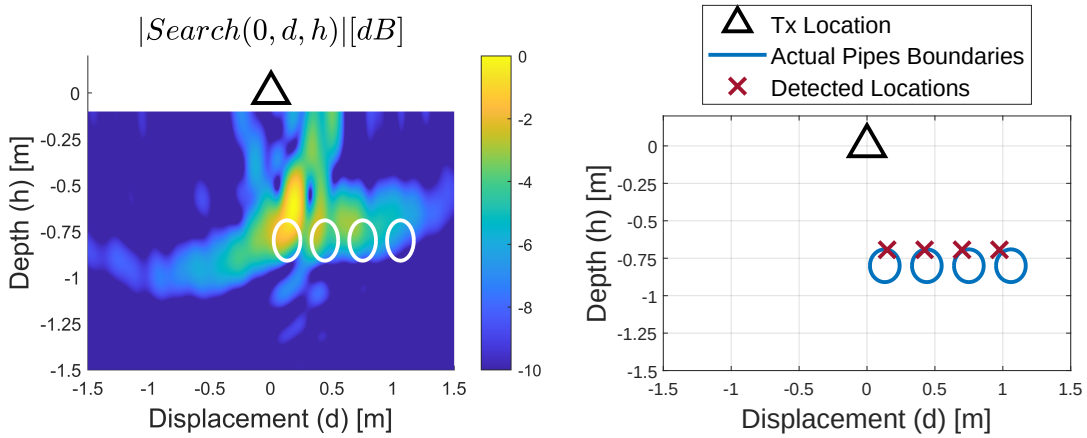
of these vertically buried pipelines as will be shown in Section 4.4.

4.4 Performance Evaluation for The inversion Algorithms

With the forward model validated in the previous section, this section aims to provide a comprehensive analysis of the performance of the dynamic grid search inversion algorithm. At first, the algorithm is tested on results based on the full-wave simulation scenarios considered in the previous section. Also, the robustness of the algorithm is tested and discussed by including the signal leakage from the Tx to the Rx as well as additive noise. Finally, the algorithm is evaluated on experimental data for metallic and water-filled PVC pipes buried in a realistic lossy sand environment.

4.4.1 Performance Evaluation Using Full-Wave Simulation

To evaluate the performance of the dynamic grid search inversion algorithm, the two scenarios of 4 horizontally arranged PEC pipelines and 3 vertically arranged water-filled PVC pipelines in a loam medium in Section 4.3.2 are considered. The Tx and Rx arrangement is shown in Fig. 4.2 with an Rx circle diameter of 3.2-m. The Tx and Rx antennas are the same Hertzian dipoles and the simulation frequency range is from 150 MHz to 450 MHz, with a 20-MHz frequency step. Only the scattered field data are calculated with the FEKO simulation software. The data is then processed using Algorithm I (Fig. 4.4) and Algorithm II (Fig. 4.5). The algorithms' performance results for the first scenario of 4 horizontal PEC pipes are shown in Fig. 4.9. The Search results of applying Algorithm I shows a clear peak near the boundary of the pipeline closest to the Tx location. However, the other pipelines are not detected as their responses are suppressed by the response from the pipe closest to the Tx. Moreover, for the third and forth pipes, only one small peak is observed near them



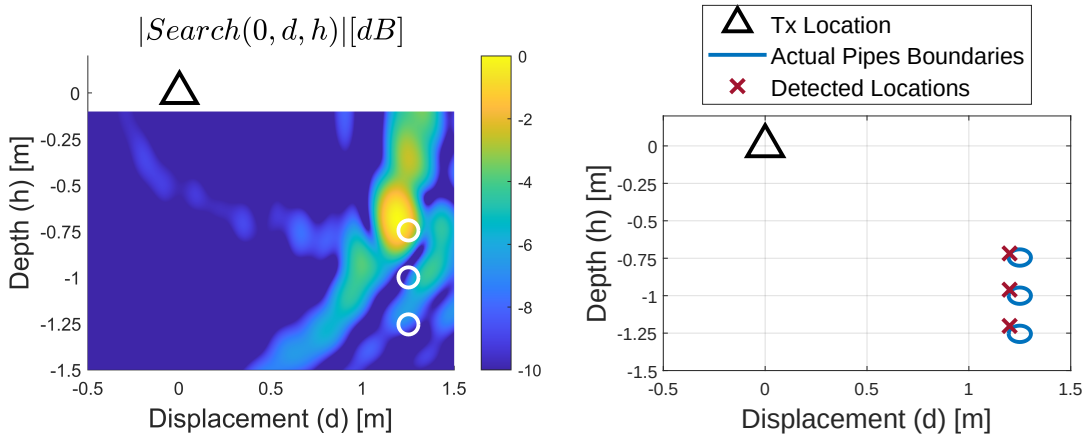
(a) (b)

Figure 4.9: An h-d cut of the Search space of Algorithm I (Fig. 4.4) (a) and the detection results of Algorithm II (Fig. 4.5) (b) when applied to full-wave simulation data. The data is for four PEC pipelines of 21.9-cm diameter and 10-cm edge-to-edge spacing inside Loam medium from Table 4.1.

due to the resolution limitations of Algorithm I. When applying Algorithm II, the final detection results show the ability of the algorithm to detect all four pipelines with the detected locations corresponding to the upper edges of the pipes, indicating the physical fact that first-order scattering occurs at the pipes' edges, not their centers. The results for the second scenario are shown in Fig. 4.10. Here also similar to the first scenario, only one peak is shown near the top pipeline whereas the other pipelines are not detected by the basic search of Algorithm I. However, the results of Algorithm II show the ability of the algorithm to detect all three pipes at their edges closest to the Tx location.

4.4.2 Performance Evaluation Including Tx-Rx Signal Leakage

The analysis done so far considers the scattered field from the pipelines only. However, in real scenarios for multistatic subsurface radar, the received signal will contain both the response from the buried pipelines as well as a strong leakage signal resulting



(a) (b)

Figure 4.10: An h-d cut of the Search space of Algorithm I (Fig. 4.4) (a) and the detection results of Algorithm II (Fig. 4.5) (b) when applied to full-wave simulation data. The data is for three water-filled PVC pipelines of 10.2-cm diameter and 15-cm edge-to-edge spacing inside Loam medium from Table 4.1.

from the direct coupling between the Tx and Rx, in addition to the ground reflection. Such a leakage signal may hinder detection if not mitigated. To test the algorithm performance in the presence of a leakage signal, the forward model in (4.3) is used to generate pipeline-scattered-field data. Next, the leakage signal is obtained by full-wave simulation of Tx and Rx Hertzian dipoles located 5 cm above empty an sand medium and added to the forward-model data. The Tx-Rx configuration is the same one used in Section 4.3.2 and the frequency range is from 150 MHz to 450 MHz, with 20-MHz frequency step. Mathematically, the received signal for the m^{th} frequency and n^{th} Rx location is calculated as:

$$V_{mn} = FM_{mn}(ar, N_p, d_c, h_c, s) + a\, V_{mn}^{Leakage} \tag{4.8}$$

where a is a scaling factor that adjusts the leakage signal to different levels. For comprehensive analysis, 20 different cases of buried pipelines are considered where the parameters of the forward model are obtained randomly and summarized in Table 4.2. To quantify the algorithm performance across all cases, the true and false detection

Table 4.2: Benchmark Performance Cases

Parameter	Cases Values
ar	$1, 2, 2, 1, 1, 1, 1, 2, 2, 2, 1, 1, 1, 2, 2, 2, 1, 2, 2, 2$
N_p	$3, 5, 2, 5, 5, 5, 3, 4, 5, 4, 3, 3, 3, 3, 2, 4, 4, 2, 5, 2$
h_c $[m]$	$0.77, 0.87, 0.91, 0.70, 0.71, 0.74, 0.94, 0.79, 0.74, 0.81,$ $0.73, 0.59, 0.81, 0.89, 0.66, 0.54, 0.79, 0.57, 0.51, 0.70$
d_c $[m]$	$0.67, 0.34, 0.55, 0.94, 0.52, 0.32, 0.40, 0.020, 0.81, 0.97,$ $0.74, 0.41, 0.86, 0.27, 0.13, 0.70, 0.96, 0.28, 0.14, 0.99$
s $[m]$	$0.20, 0.15, 0.20, 0.15, 0.15, 0.25, 0.25, 0.10, 0.15, 0.25,$ $0.10, 0.25, 0.25, 0.25, 0.25, 0.10, 0.10, 0.15, 0.15, 0.20$

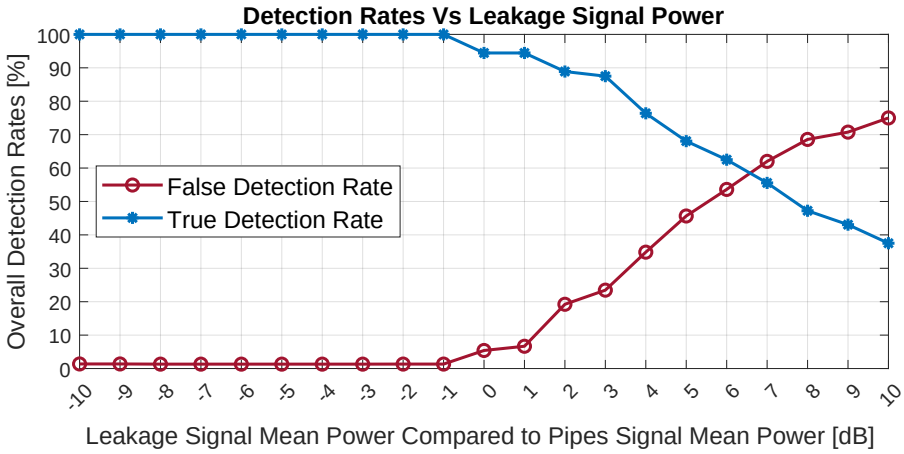


Figure 4.11: Overall detection rates across the 20 pipelines cases in Table 4.2 buried in Sand medium (Table 4.1) for varying levels of leakage signal.

rates are defined as:

$$True\ Detection\ Rate = \frac{N_{Truly\ Detected}}{N_{Actual\ Pipes}} \tag{4.9}$$

$$False\ Detection\ Rate = \frac{N_{Falsely\ Detected}}{N_{Detected\ Pipes}} \tag{4.10}$$

where the true detection criterion is when the detected pipe location does not differ from the actual location by more than 5 cm and N stands for the total number across all the considered cases. Fig. 4.11 shows the detection rates for varying levels of leakage signal. The performance results show that the algorithm works well so long

as the leakage signal is at the same level as the pipes' signal or lower. It should be noted that the leakage signal is typically much stronger than the buried pipeline signals. However, because the leakage signal travels through air while pipeline signals travel through soil at lower speeds, the leakage signal arrives much earlier and can be gated out. When proper gating is applied, the remaining part of the leakage signal (the part that has similar delays to the pipeline signals) is only the time domain side-lobes of the leakage signal and such side-lobes typically have low values and are not expected to be higher than the pipeline signals. When the side-lobes are quite high, a Gaussian window can be applied in the frequency domain to reduce time domain side-lobes as discussed in [10]. Furthermore, for cases where the pipelines are not buried deep enough, time-gating may not work and an alternative differential radar mode can be adopted to mitigate the leakage signal as will be discussed in Chapter 6, or some mechanism to increase isolation between the Tx and Rx may be used as is done in the experimental part of this Chapter (Subsection 4.4.4).

4.4.3 Performance Evaluation Including Noise

Another aspect of this investigation is to determine the robustness of the dynamic grid search inversion algorithm against noise. To investigate that, data was generated using the forward model (4.3) for the 20 cases in Table 4.2. After that, an Additive white Gaussian noise (AWGN) was added to the data with varying signal-to-noise (SNR) ratios. The dynamic grid search algorithm (Fig. 4.5) was then applied to the noisy data using the same frequency range and Tx-Rx configuration in Section 4.4.2 and the detection rates defined in (4.9) and (4.10) were calculated and plotted in Fig. 4.12 for the sand and clay media of Table 4.1. The results show that the algorithm to is indeed robust so long as the SNR is above 15 dB. It should be noted that such SNR level can be easily achieved in subsurface radars operating in the frequency range 150 MHz - 450 MHz because the propagation losses are not high

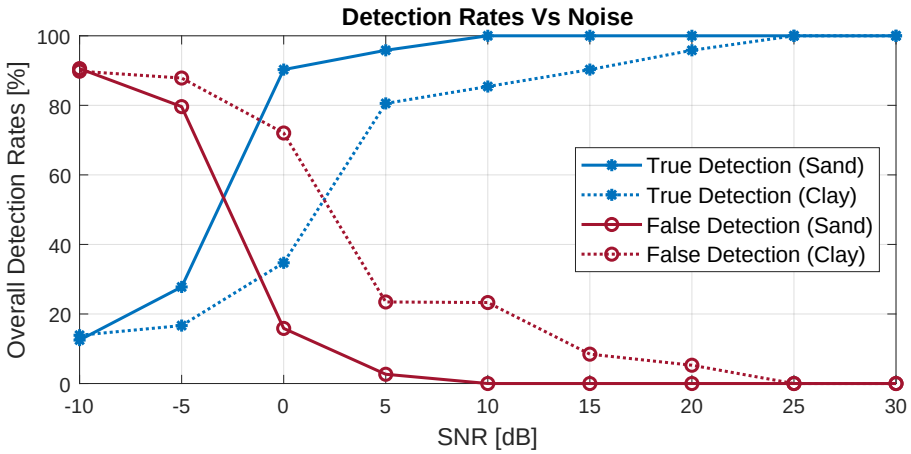


Figure 4.12: Overall detection rates across the 20 pipelines cases in Table 4.2 buried in sand and clay media (Table 4.1) for varying levels of noise.

at these frequencies, making the received signal well above the thermal noise level. When the source of noise is radar clutter rather than thermal noise, the algorithm may not perform optimally and a noise-suppression procedure needs to be performed before applying the algorithm.

4.4.4 Performance Evaluation Using Experimental Data

To evaluate the dynamic grid search algorithm performance on actual data, a realistic sandy environment at Silver Lake Recreation Area, Pinckney, MI, USA, was chosen to perform the experiments. The experimental location is shown in Fig. 4.13 along with the dielectric profile of the sand as a function of depth measured on site by a portable ring resonator probe discussed in [87]. After determining the sand permittivity, two experiments were carried out. In one experiment, two metallic pipelines with 5-cm diameter and 20-cm edge-to-edge spacing are buried at 35 cm depth. In the other experiment, two water-filled PVC pipelines with 9-cm diameter and 20-cm edge-to-edge spacing are buried at 35 cm depth. Fig. 4.14 shows the buried pipelines. The data in the two experiments were collected with the portable vector network analyzer (VNA) based multistatic SAR system shown in Fig. 4.15. There is a fixed Tx antenna

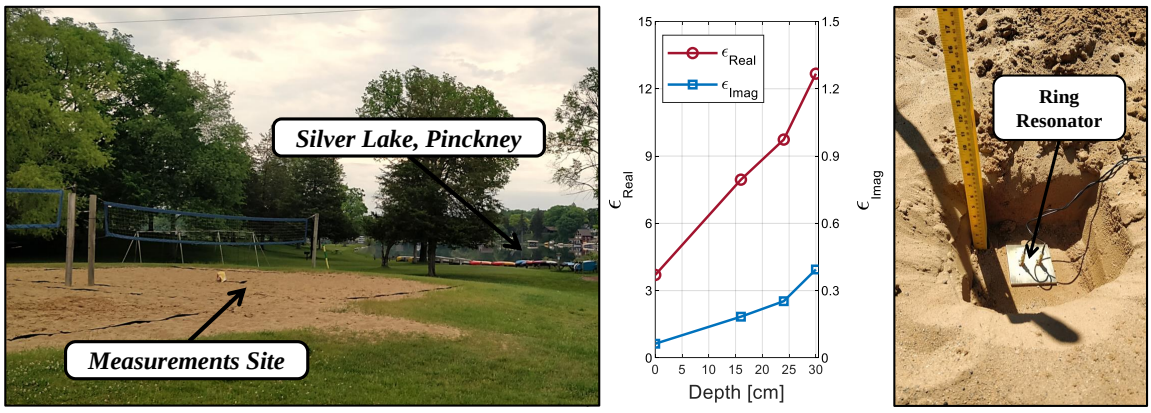
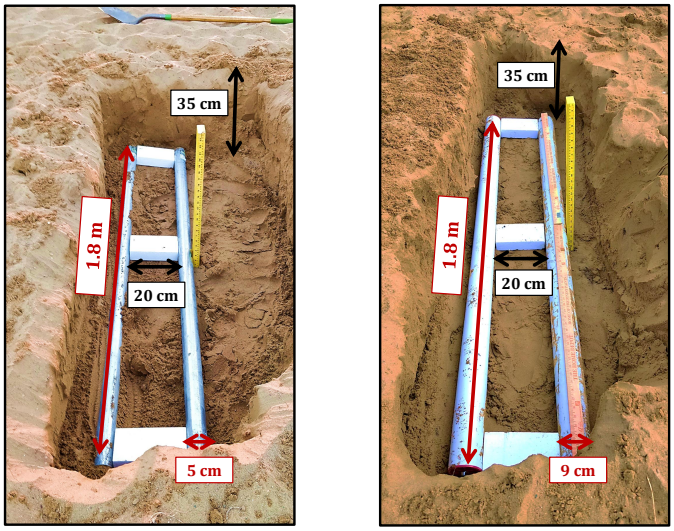


Figure 4.13: Experiments location near Silver Lake, Pinckney, MI, USA along with the ring resonator probe and the resulting dielectric profile



(a) (b)

Figure 4.14: Buried metallic (a) and water-filled PVC (b) pipelines used in the two experiments

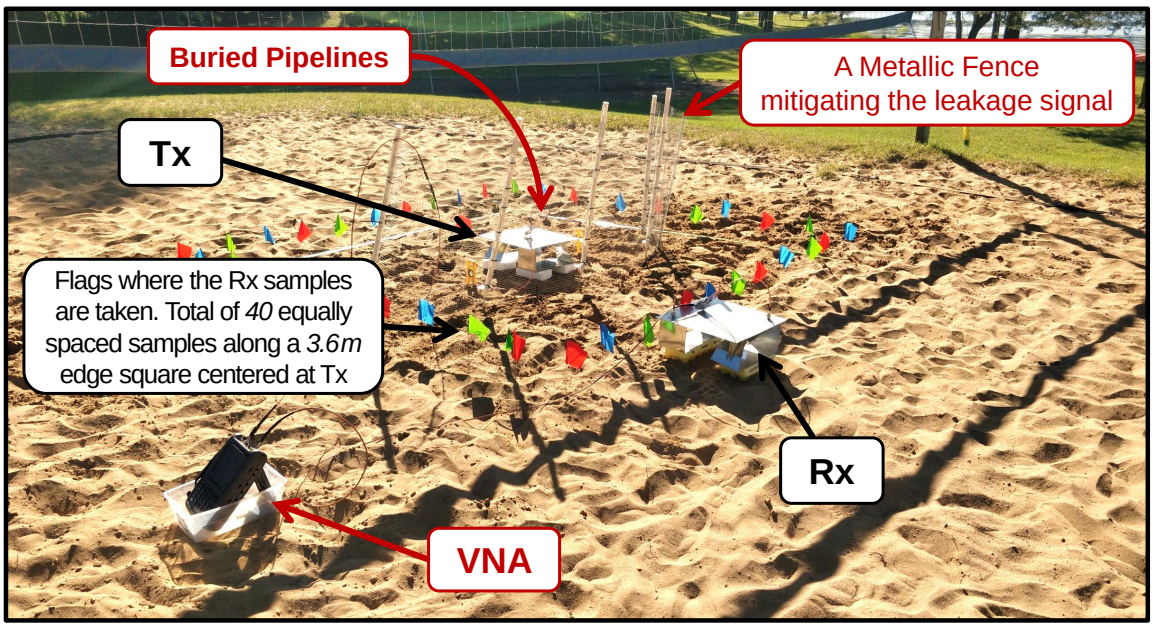
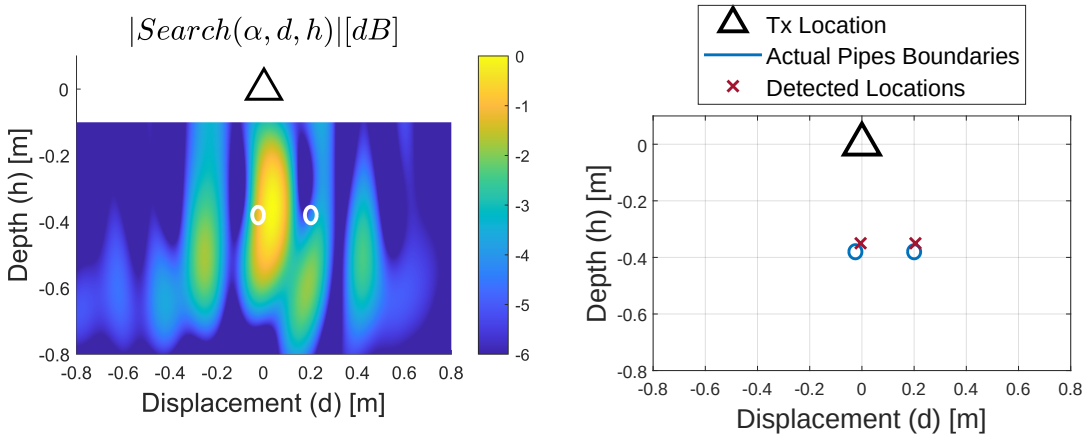


Figure 4.15: VNA-based multistatic SAR setup for both experiments. The Rx is moved along a square of 3.6-m edge length, collecting S_{21} data at 40 different locations while the Tx is fixed in the middle.

in the middle of the scene and an Rx antenna that is moved around the Tx along a square of 3.6-m edge length, collecting a total of 40 S_{21} parameter samples at different locations, using the VNA over the range 150 MHz to 450 MHz in 20 MHz frequency increments, 3dBm power (maximum allowed by the VNA) and 1 kHz IF bandwidth. The antennas used for the Tx and Rx are ENVELOPE antenna arrays designed specifically for subsurface radars and discussed in [78]. To mitigate the leakage signal, a metallic fence is inserted between the Tx and Rx antennas. Moreover, the collected S_{21} data are processed to remove the delay and attenuation caused by the coaxial cables. This is done by dividing the collected S_{21} data by S_{21} measured for the cables when they are connected together by a through connector. After removing the cables delay and attenuation, both Algorithm I (Fig. 4.4) and Algorithm II (Fig. 4.5) are applied to the data. The results for the metallic pipelines experiment are shown in Fig. 4.16. The basic search algorithm results in a single peak between the two pipelines, thereby unable to resolve them, while the final result of the dynamic grid



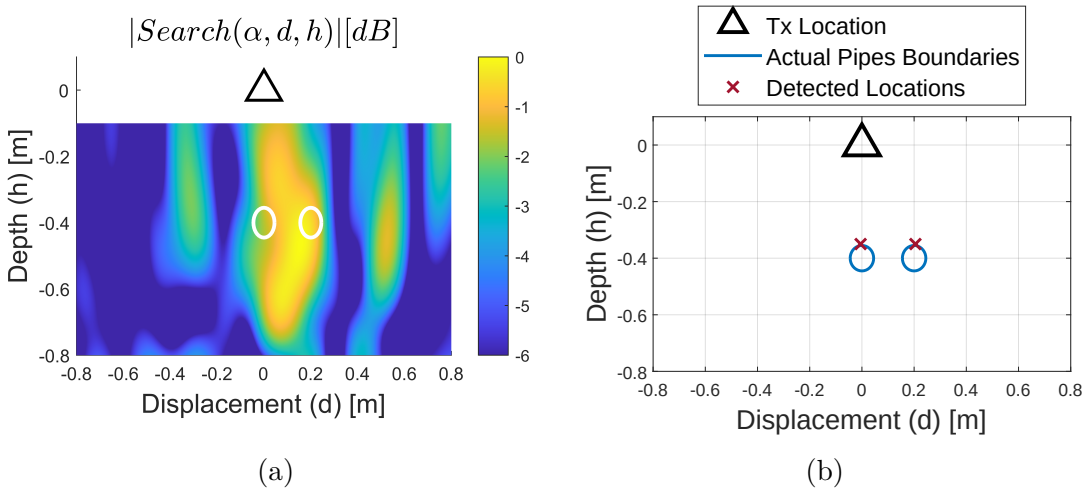
(a) (b)

Figure 4.16: An h-d cut (at the actual α) of the Search space of Algorithm I (Fig. 4.4) (a) and the detection results of Algorithm II (Fig. 4.5) (b) when applied to metallic pipelines experiment (Fig. 4.14a). The data is for 2 metallic pipelines of 5cm diameter and $d_1 = -0.225, d_2 = 0.025, \alpha = 0, h_c = -0.35$ (See Fig. 4.2).

Table 4.3: Computation Time for Algorithm II at Different Search Resolutions

$max(N_p)$	$\delta s\,[cm]$	$\delta d\,[cm]$	$\delta h\,[cm]$	Time [minutes]
5	8	8	8	0.97
5	4	8	8	1.52
5	2	8	8	2.8
7	8	8	8	2.03

search algorithm shows two detected pipelines near the actual pipeline boundaries. Moving to the second experiment, the results for the water-filled PVC pipelines are shown in Fig. 4.17. Here again the dynamic grid search algorithm managed to resolve the two closely spaced pipelines while the basic search algorithm results in a single peak between the two pipelines. A finial point to mention is the computation time required by the novel Algorithm II (Fig. 4.5). The time mainly depends on the required search resolution (i.e the spacing $\delta s, \delta d, \delta h$) and the maximum number of pipelines considered. Using "Intel(R) Core(TM) i7-8700 CPU @ 3.20GHz" processor, 16 frequency points, 36 Rx samples, and fixing $max(s)$ to 80 cm, the required times for running Algorithm II (Fig. 4.5) are summarized in Table 4.3.



(a) (b)

Figure 4.17: An h-d cut of the Search space of Algorithm I (Fig. 4.4) (a) and the detection results of Algorithm II (Fig. 4.5) (b) when applied to water-filled PVC pipelines experiment (Fig. 4.14b). The data is for 2 water-filled PVC pipelines of 9cm diameter and $d_1 = -0.245, d_2 = 0.045, \alpha = 0, h_c = -0.35$ (See Fig. 4.2).

4.5 Conclusion

In this chapter, a novel 3D forward scattering model and dynamic grid-search based inversion algorithm for multiple buried pipelines in wideband multistatic subsurface synthetic aperture radar (SAR) is proposed. The model tracks the scattering phase centers of each pipeline for each receiver position, then accounts for both propagation phase and amplitude attenuation due to propagation and medium losses. An objective function is defined as the misfit between the received data and the forward model. After that, the dynamic grid search algorithm minimizes the objective function, leading to detection and localization of closely spaced pipelines along the range and cross range directions. The forward model is validated with full-wave simulations and the algorithm is applied to full-wave simulation data as well as experimental data, demonstrating its superiority over the basic phase compensation (focusing-based) algorithm for buried pipelines detection proposed in Chapter 3. After successful detection and localization of buried pipelines, the next chapter will utilize this knowledge to improve buried pipeline leaks detection in multistatic subsurface SAR.

CHAPTER 5

Detection and Localization of Buried Pipeline Leaks

5.1 Introduction

As detailed in Chapter 3, pipelines have multiple scattering phase centers that scatter the incident wave to the different Rx positions. When trying to detect pipeline leaks using a multistatic subsurface SAR, the multiple scattering phase centers make the pipeline contribution to the radar response much larger compared to the more localized leak contribution. This makes leak detection a challenging task. To address this challenge, this Chapter utilizes the different scattering mechanisms of the leak and the pipeline signals illustrated in the multistatic SAR configuration shown in Fig. 5.1, and presents a technique to identify and eliminate the pipeline contribution, after which a back-projection (BP) algorithm is applied to the remaining part of the radar response to improve leak detection and localization. The rest of the chapter is organized as follows. Section 5.2 presents the received signal model and explains the pipeline signal identification and elimination technique as well as how BP is applied to detect the leak. Section 5.3 presents a physics-based oil spread model inside the soil as well as a semi-empirical formula for calculating the leak's dielectric. Section 5.4 presents comprehensive full-wave simulations in addition to experimental measurement results demonstrating the effectiveness of the proposed technique.

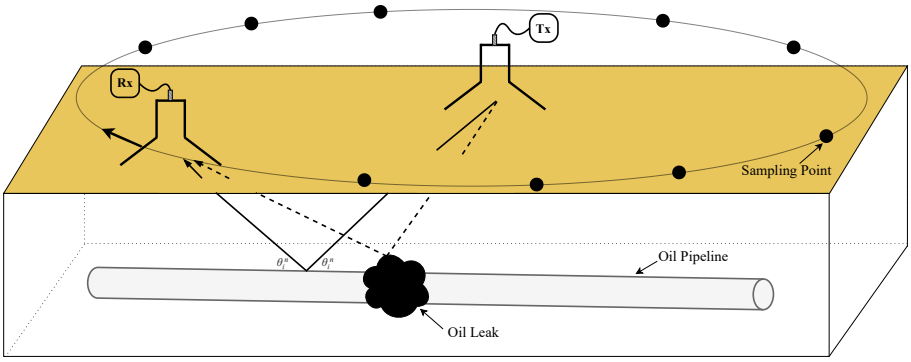


Figure 5.1: Multi-static subsurface SAR imaging arrangement, the pipeline signal (soild) takes a different path compared to the leak signal (dashed).

5.2 Leak Detection and Localization Technique

The geometry of the scattering problem is shown in Fig. 5.1. There is a pipeline (dielectric or metallic) placed in the lower half-space soil medium with the pipe being parallel to the soil-air interface. There is also a region in the soil around a point on the pipeline representing the leak. A multistatic radar arrangement is considered where the antennas are placed close to the interface and matched to the soil medium, as explained in [78]. Assuming the pipe location and orientation are already known using the pipe detection and localization algorithm proposed in Chapter 3, the following subsections provide the received signal model, a technique to estimate the pipeline part of the signal, the way BP algorithm is used to detect the leak after eliminating the pipeline response and conclude with a discussion about the optimal arrangement of Rx samples.

5.2.1 Received Signal Model

In order to remove the response of the pipeline from the overall signal, the received signal needs to be modeled based on the physics of the problem. To do that, the multiple interactions between the pipe and the leak are ignored. This leads to the following $e^{j\omega t}$ time dependent signal model for V_{mn}, the voltage received across the

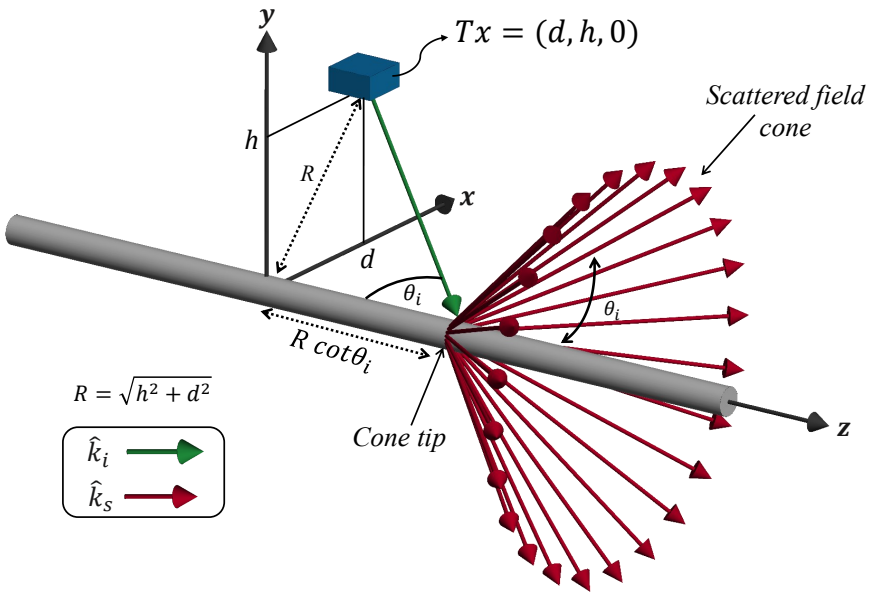


Figure 5.2: Perspective view for the scattering scene with the coordinate system along the pipeline used for analysis. The incident wave making an angle θ_i with the pipeline axis generates a scattered field cone with θ_i as generating angle.

n^{th} Rx terminals at the m^{th} frequency:

$$V_{mn} = A_{mn}^{Pipe}\, e^{-j\beta_{mn}^{Pipe}} + \iiint_V A_{mn}^{Leak}(\boldsymbol{r'})\, e^{-j\beta_{mn}^{Leak}(\boldsymbol{r'})}\, d\boldsymbol{r'} \tag{5.1}$$

where A_{mn} and β_{mn} refer to the amplitude and phase at the n^{th} Rx location and m^{th} frequency, respectively. The leak response is represented as an integral over the volume of the leak. To determine the propagation phase of the pipe part of the signal, the conic propagation behavior of the pipe's scattered signal, discussed in Chapter 3 and illustrated in Fig. 5.2, is utilized. For a pipeline located at depth h and displaced at a distance d with respect to the Tx, the incident wave along the vector $\hat{k}_i$ impinges on the pipe at an angle θ_i^n and generates a set of scattered field vectors $\hat{k}_s$, forming a cone that intersects the n^{th} Rx location of interest. As derived in Chapter 3, the

cone generating angle θ_i^n is given by:

$$\theta_i^n = arctan\Big(\frac{\sqrt{h^2 + x_{on}^2} + R}{z_{on}}\Big) \tag{5.2}$$

where x_{on}, z_{on} are the coordinates of the n^{th} Rx on the ground and R is the distance of the Tx from the origin of the coordinate system used in the analysis and given by:

$$R = \sqrt{h^2 + d^2} \tag{5.3}$$

Once θ_i^n is found, the pipe signal phase can be calculated as:

$$\beta_{mn}^{Pipe} = k_m(R_{Tx-To-S^n} + R_{S^n-To-Rx_n}) \tag{5.4}$$

where k_m is the wave propagation constant inside the soil and $R_{Tx-To-S^n}$ is the distance from the Tx to the cone's tip S^n on the pipe and $R_{S^n-To-Rx_n}$ is the distance from the cone's tip to the n^{th} Rx location, calculated as:

$$R_{Tx-To-S^n} = \sqrt{(R\,cot\,\theta_i^n)^2 + R^2} \tag{5.5}$$

$$R_{S^n-To-Rx_n} = \sqrt{(R\,cot\,\theta_i^n - z_{on})^2 + x_{on}^2 + h^2} \tag{5.6}$$

Knowing β_{mn}^{Pipe} makes it possible to reconstruct the pipe contribution to the received signal if the pipe amplitude coefficient in (5.1) is known. Since the received signal from the pipe is in the form of a discrete sum of exponential terms, the generalized pencil of function (GPOF) procedure can be used to estimate the pipe amplitude coefficient in (5.1).

5.2.2 GPOF Method

Generalized pencil of function (GPOF) is a mathematical procedure for approximating a signal by a sum of complex exponents varying in amplitude and phase [92]. For Radar applications, each exponent can be interpreted as representing a specific scatterer whose phase depends on its location with respect to the Radar system [16]. Using GPOF, the actual received signal at the n^{th} Rx location is approximated by:

$$V_{nm}^{GPOF}(K) = \sum_{k=1}^{K} A_k \, e^{j\omega_m t_k} \tag{5.7}$$

where A_k and t_k are complex in general and the integer K is a fitting parameter that needs to be specified. Here, t_k physically represents the delay propagation time and A_k specifies the amplitude of the scatterer. Choosing K too large may lead to superfluous exponents that do not correspond to the actual physical scatterers such as exponents with negative time delays. To put (5.7) in a physically meaningful form that is close to (5.1), K is chosen iteratively until a sensible physical representation is achieved. Basically, GPOF is applied for the received signal at each Rx location and K is increased in 1-step increments. At each increment of K, the fitting error at the n^{th} Rx location is calculated as:

$$Error = \sum_{m=1}^{M} | V_{nm}^{Received} - V_{nm}^{GPOF}(K)| \tag{5.8}$$

Then the K value resulting in the first local minimum of (5.8) is chosen for that particular Rx location. Among all exponential terms, one belongs to the pipeline. This is typically the one with the largest amplitude. But, we can more generally identify it by requiring the phase associated with the exponent to be the one closest

to the known pipeline phase calculated using (5.4). Mathematically, the index (i) of the term associated with the pipeline signal is found by:

$$i = \underset{i}{\operatorname{argmin}} |Re(t_i) \times c_{Soil} - \beta_{mn}^{Pipe}/k_m| \tag{5.9}$$

where c_{Soil} is the wave speed inside the soil and β_{mn}^{Pipe} is calculated using (5.4). After finding the index (i), the GPOF approximated pipe signal becomes:

$$\tilde{V}_{mn}^{Pipe} = A_i \, e^{j\omega_m t_i} \tag{5.10}$$

5.2.3 BP Algorithm for Leak Detection

With the knowledge of the pipe signal, the pipe contribution can be subtracted from the overall radar, response resulting in a clearer leak signal that can be used in the BP algorithm to find the leak location. Rather than interpreting the images formed by BP to identify the leak presence, an easy to interpret leak indicator is defined at each point along the pipe axis as follows. At each point along the pipe, BP is applied on a rectangular slice of width (W) and height (H) that is transverse to the pipe axis and centered around it at that point. After that, the focused pixels in the image formed by BP in that slice are summed together, thereby defining the value of the leak indicator $I(z)$ at that point. This sum (leak indicator) is expected to have large values at the points that correspond to the leak location since the associated slices will have a larger number of bright pixels due to the leak presence compared to the slices at other points which have fewer bright pixels. The slice width (W) and height (H) are chosen depending of the extent of the Rx locations on the ground (the synthetic aperture size) and the expected extent of the leak spread. In this work, W

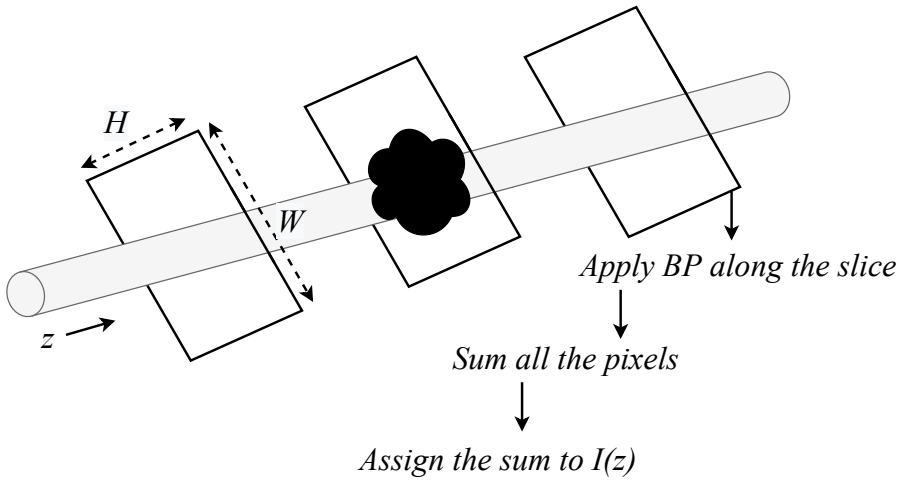


Figure 5.3: Steps followed in applying BP algorithm and obtaining the leak indicator.

is chosen to be 2 meters while H is fixed at 0.7 meters. Fig. 5.3 provides a visual illustration of the steps followed to obtain the leak indicator. Mathematically, the leak indicator $I(z)$ at the point z along the pipe axis is found by:

$$\begin{aligned} & I(z) \\ & = \iint_{Slice} \sum_{n=1}^{N} \sum_{m=1}^{M} \left(V_{nm}^{GPOF} - \tilde{V}_{mn}^{Pipe} \right) e^{jk_m R_n(x,y)} \, dx \, dy \\ & \approx \sum_{p=1}^{P} \sum_{n=1}^{N} \sum_{m=1}^{M} \left(V_{nm}^{GPOF} - \tilde{V}_{mn}^{Pipe} \right) e^{jk_m R_{np}} \end{aligned} \tag{5.11}$$

where V_{nm}^{GPOF} is the GPOF reconstructed signal at the n^{th} Rx and m^{th} frequency and R_{np} is the total signal path from the Tx to the p^{th} pixel located at (x_p, y_p) in the transverse slice cutting the pipe at location z, and from that to the n^{th} Rx. Here, $e^{jk_m R_{np}}$ compensates for the propagation phase between the Tx and the Rx, thus the term back-projection (BP). This $I(z)$ is calculated for a specific scan where the Tx is fixed and the Rx is moved around it. To further enhance the detection, $I(z)$ is better calculated using multiple scans by fixing the Tx in a new position relative to the pipe for each new scan. After that, the overall $I(z)$ is found by multiplying the indicators

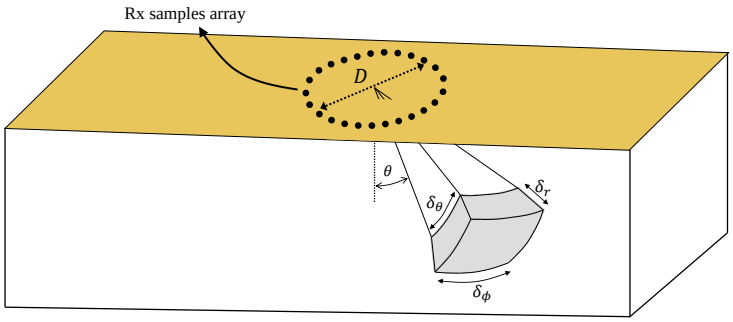


Figure 5.4: Rx array configuration with the volumetric resolution cell along the three orthogonal directions.

from each scan:

$$I(z)^{Overall} = \prod_{j=1}^{J} I(z)^{Scan_j} \tag{5.12}$$

The product enhances the true peak that corresponds to an actual leak compared to the noisy peaks that move randomly as the Tx is moved in each scan which leads to a more robust leak detection.

5.2.4 Radar Resolution and Rx Array Configuration

The formulation in the preceding subsections is a general one that works for any Rx position configuration. To determine the optimal Rx position configuration, the 3D radar image resolution is taken as the objective. The radar resolution can be defined along three orthogonal directions as indicated in Fig. 5.4. The proportionality of the resolution in the three directions is given by:

$$\delta_r \propto \frac{c_{soil}}{BW}, \qquad \delta_\theta \propto \frac{\lambda}{D \times cos\theta} \qquad \delta_\phi \propto \frac{\lambda}{D} \tag{5.13}$$

where the range resolution δ_r is governed by the wave speed inside the soil c_{soil} and the signal bandwidth BW which is determined by the radar antenna. The resolution

along the elevation and azimuthal directions $\delta_{\theta,\phi}$ is governed by the maximum Rx position's separation D and the wavelength λ. If there is apriori information about the approximate shape of the leak, then the Rx samples can be arranged along a line parallel to the leak spread to maximize D in the leak direction and get the best results. However, in the general case where the leak spread is not known, it is better to use a circular arrangement since it gives a uniform D (hence a uniform beamwidth) along all directions. For the Rx samples spacing, too wide a spacing generates grating lobes along undesired directions which may worsen the detection. To ensure the suppression of grating lobes, the separation between Rx samples should be $\frac{\lambda_{min}}{2}$ or less, where λ_{min} is the minimum wavelength inside the soil. This criterion may be relaxed if there are not many scatteres under the ground, in which case grating lobes may not affect the detection since they will not coincide with other scatterers.

5.3 Oil leak Model

To test the performance of the algorithm, the oil leak needs to be modeled in a realistic way that captures its spread through the pores in the soil as well as its electrical properties (i.e., its permittivity). In the following subsections, a physics-based leak spread model in a soil medium is introduced and a semi-empirical permittivity model for the oil leak mixed with soil is presented.

5.3.1 Modeling Leak Spread

The soil pore structure is modeled as a 3D arrangement of cylindrical tubes varying in their radii according to the semi-empirical pore radii distribution provided in [93]. This is a typical practice employed for the flow in porous media literature (see [94, 95]). At the point where the pipeline is cracked, the liquid exiting the pipe flows through the soil via the cylindrical tubes due to the pressure in the pipe. Generally speaking, fluid

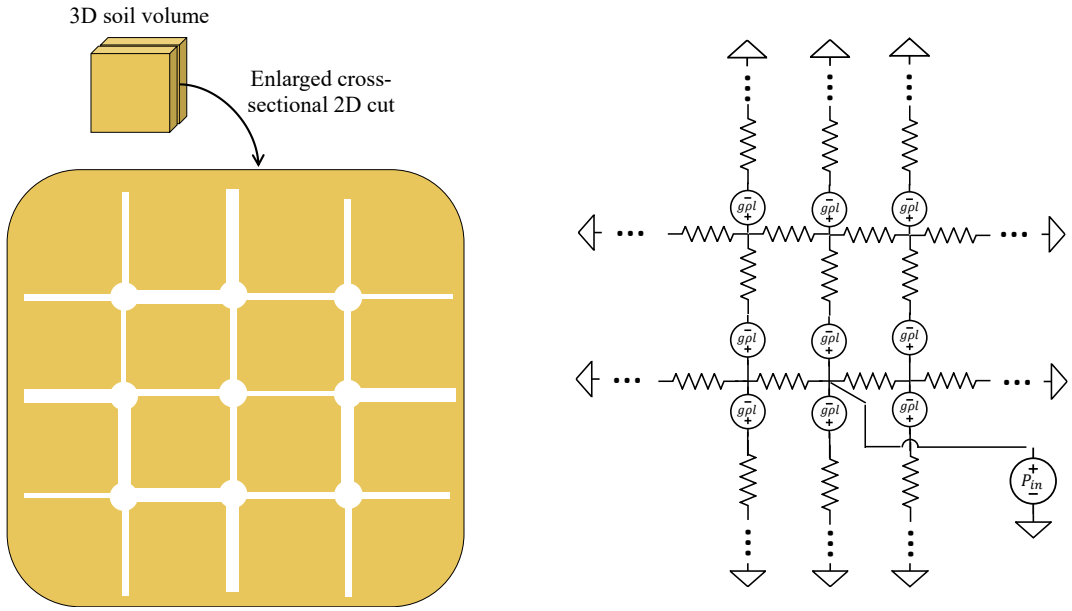
flow is categorized into laminar and turbulent flows depending on the fluid velocity direction with respect to the axis of the tube it is passing through. Laminar flow refers to the case where the velocity is aligned with the tube axis while turbulent flow contains movements in other directions. What determines the flow type is the ratio between the inertial forces the tube exerts on the fluid and the viscous forces exerted among the fluid molecules, and this ratio is called Reynolds number [96]. Using a typical soil pore scale ($\sim 10^{-4}\, m$) and oil velocity ($\sim 2\, m/s$) [97] along with oil density ($\sim 850\, kg/m$) and viscosity ($\sim 0.0025\, Ns/m^2$), the Reynolds number for leaking oil is calculated to be around 200, which is well within the laminar flow range (i.e. $<$ 2000), as discussed in [96]. For laminar flow, the total oil flow (in m^3/s) through the soil pores is related to the leak pressure by Hagen-Poiseuille equation as derived in [98]:

$$\Delta p = \left(\frac{8\, \mu\, l}{\pi r^4} \right)\, Q \tag{5.14}$$

where Δp is the pressure difference, μ is the oil dynamic viscosity, l is the tube length, r is the tube radius and Q is the total flow. Furthermore, when the tube branches out, the total flow is conserved:

$$Q_{in} = Q_{out} \tag{5.15}$$

Equations (5.14) and (5.15) have the same form as Ohm's law and Kirchhoff's current law, respectively which suggests that the oil leak spread through soil pores can be modeled as an electrical current flow in a 3D lattice of resistors where the pressure corresponds to the voltage, the total flow to the current and resistance to the quantity in parentheses in (5.14). In addition to the pressure at the leak location, additional pressure is exerted by gravity, which can be modeled as additional voltage sources in the network, each with the value of $(g\, \rho\, l)$ where g is the gravitation acceleration, ρ



(a) Soil Pores (b) The Equivalent Circuit

Figure 5.5: A cross-sectional 2D cut visual illustration for the actual 3D structure of soil pores model. The equivalent circuit extends in 3D but only a side view of the circuit is shown for better visibility.

is oil density and l is the tube length. As a visual illustration for this 3D soil pores model, Fig. 5.5 provides an enlarged cross-sectional 2D cut out of the 3D soil volume as well as the equivalent circuit model. It is worth mentioning that modeling fluid spread through soil by an electrical circuit is not new and similar approaches were considered in [95] and [94]. With the electric circuit model, the following procedure is used to generate the leak in our model.

1. Construct the pores model in Fig. 5.5a by drawing the radii values from the statistical distributions in [93] depending on the desired soil particles mix (sand, clay, slit).

2. Fix the length of the tubes (l) to $5\,r_{md}$, where r_{md} is the median value of the drawn radii.

3. Transform the model into a Netlist circuit model as illustrated in Fig. 5.5b

where the resistances are calculated from (5.14) and P_{in} is fixed to ($P_{Leak} - P_{atm} - P_{Soil}$), where P_{Leak} is the pressure at pipeline crack, P_{atm} is the atmospheric pressure and P_{Soil} is the pressure due to the soil above the pipe.

4. Simulate the Netlist using LTspice® software.

5. Determine the leak spread boundaries as the voltage nodes that have a value less than a threshold V_{th}.

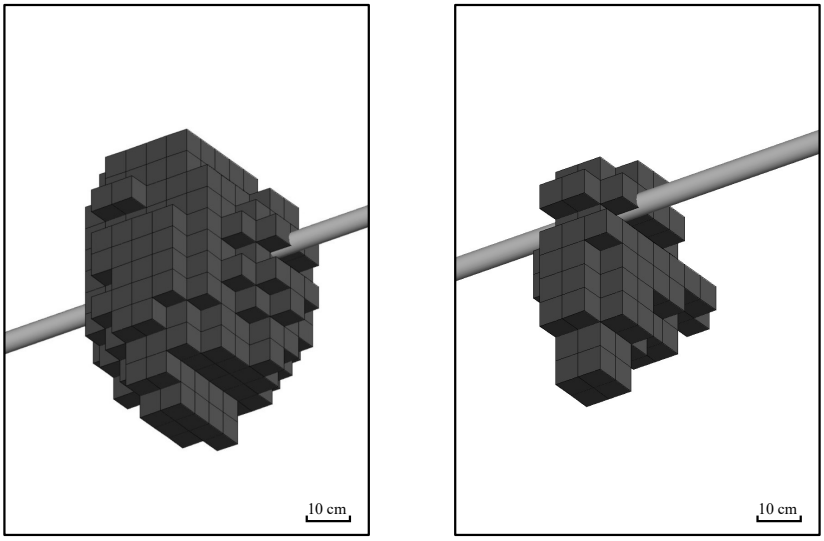
6. Transform the voltage nodes into a spatial boundary using the values of the drawn radii.

7. Construct the leak in FEKO full-wave simulation software by filling the inside of the leak boundary with adjacent small enough ($< \lambda_{min}/10$) dielectric cubes.

Ideally, the circuit network should be large enough so that converting the resistors back to their equivalent soil bores leads to a realistically sized leak. However, doing that is rather impractical since it requires billions of resistors. Instead, a manageable number of resistors is simulated in the circuit simulator and the resulting shape is scaled up to a realistic size. In this work, a $17 \times 17 \times 17$ resistor circuit is simulated then scaled up to a 3D cube with 1-m edges in a size to represent the leak. Moreover, P_{Leak} is fixed at a typical value of 1 MPa following [99]. Two contrasting examples of a leak generated using sand and clay pore distributions is shown in Fig. 5.6 where V_{th} is taken to be 10% of the initial voltage value P_{in}. More leak spread is observed for sand due to its relatively large pores compared to clay's small pores that resist pressure strongly.

5.3.2 Oil Contaminated Soil Permittivity

The leaked oil is mixed with surrounding soil by replacing the air-filled pores among soil particles with oil-filled pores. The higher dipole moment of oil compared to



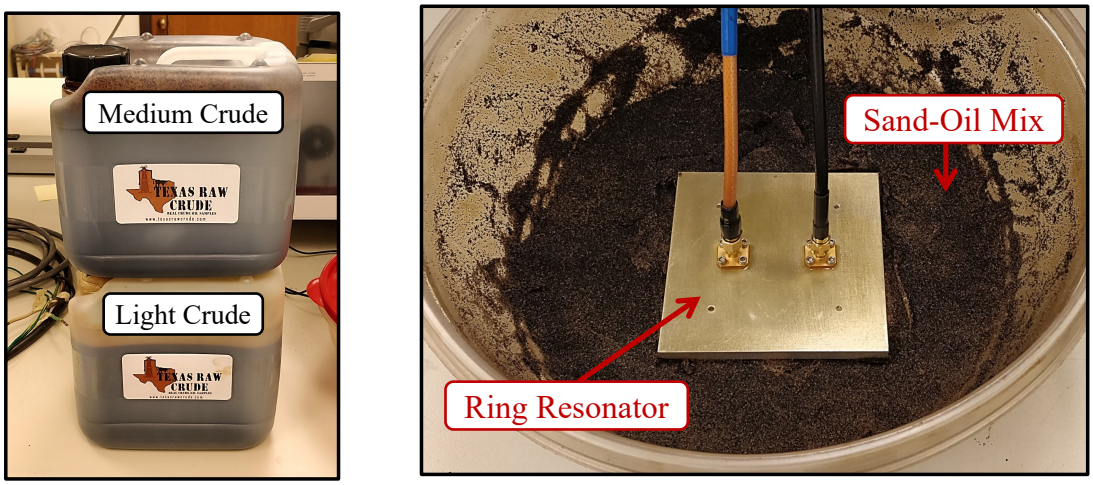
(a) Sand (b) Clay

Figure 5.6: Leak samples generated using the outlined procedure.

Table 5.1: Oil Samples Used in Dielectric Measurements.

Sample Name	**Flash Point [F]**	**API Gravity**	**Measured ϵ_r**
North Well (light)	74	34.1	$3.15 - j0.058$
Scott Well (medium)	158	24.3	$3.29 - j0.054$

that of air makes the oil-soil mixture have a higher dielectric constant value than soil alone. To investigate this increase, the dielectric constant of a mixture of sand and oil with varying percentages is measured experimentally and fitted to a semi-empirical dielectric mixing formula. After that, the formula is used to predict the dielectric constant of an oil leak in any soil mixture other than sand. Two crude oil samples ordered from Texas Raw Crude [100] Texas, USA (Fig. 5.7a) are used in the measurements and their properties are summarized in Table 5.1. The crude oil is mixed with sand in a container (Fig. 5.7b) and the ring resonator dielectric probe proposed in [87] is used to measure the mixture dielectric constant. After that, the



(a) (b)

Figure 5.7: (a) Oil samples used (b) ring resonator probe mounted on sand-oil mixture for dielectric measurements.

following mixing formula [101] is fitted to the measured dielectric values:

$$\epsilon_{mix} = \left(\sum_{i=1}^{N} \phi_i \, \epsilon_i^{\alpha} \right)^{\frac{1}{\alpha}} \tag{5.16}$$

where ϕ_i and ϵ_i are the volume fraction of the i^{th} material and its dielectric value respectively, and α is a fitting parameter. Fig. 5.8a shows the results for a "light oil" mixture while Fig. 5.8b shows the results for "medium oil". The dielectric profiles are almost identical, suggesting a weak dependence on oil density. An additional measurement was done using "light oil" mixed with wet sand with 10% volumetric moisture and the results are shown in Fig. 5.9. As shown in all the dielectric results, the mixing formula works well for any mixture of sand, water and oil, which validates its use in full-wave simulations of different soil textures to test the leak detection technique performance in the next section.

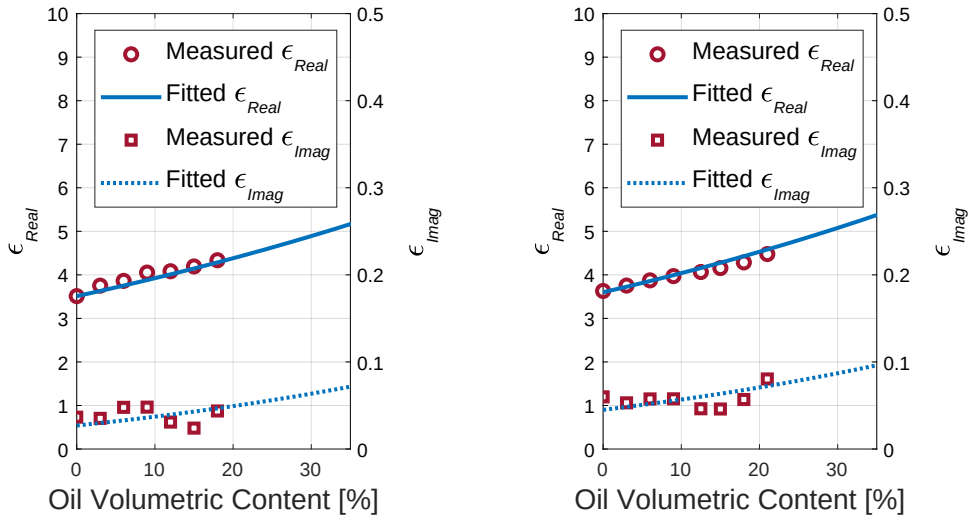


Figure 5.8: Measured and fitted ($\alpha = 0.045$) dielectric constant for sand mixed with (a) light and (b) medium oil.

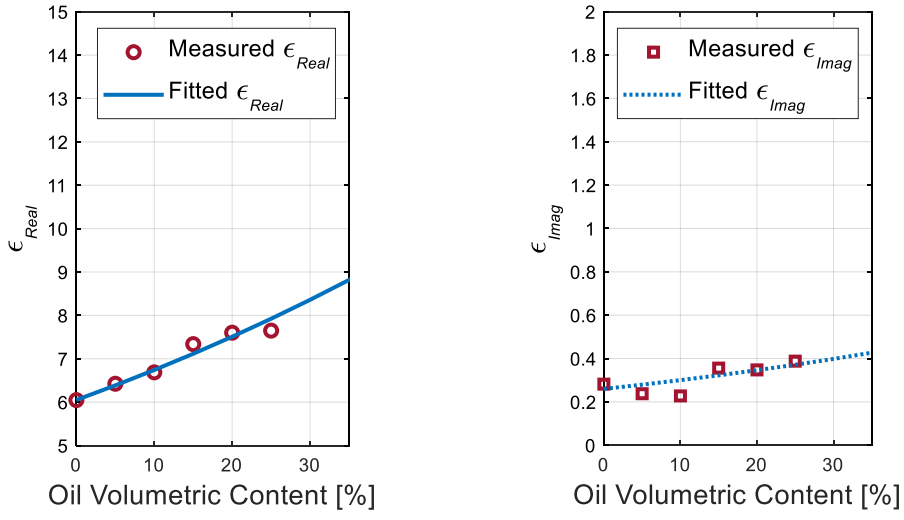


Figure 5.9: Real (a) and imaginary (b) parts of measured and fitted ($\alpha = 0.045$) dielectric constant for 10% wet sand mixed with light oil.

5.4 Simulation and Measurement Results

Using the oil leak model described above, this section provides a comprehensive examination of the proposed leak detection technique performance on a variety of leaking pipes (metallic and dielectric) buried in different backgrounds using full-wave simulation data. In addition, experimental measurements using wet-sand-filled containers as a leak with metallic as well as dielectric pipes are provided for further validation for the proposed technique performance.

5.4.1 Simulation

Full-wave analysis based on FEKO software is used to generate scattered field data for various soil backgrounds, pipeline materials and sizes. The frequency range considered is 200-500 MHz, in 6-MHz steps. Both Tx and Rx antennas are Hertzian dipoles oriented towards the direction of the pipe axis (exciting TM mode in the pipe scattered field). To cover most soil conditions, three soil types, shown in Table 5.2, are used where the permittivity values are obtained using Code 4.7 provided in [86] and the effective porosity is obtained from the soil survey in [89]. With each soil type, the leak is generated using the steps described in the previous section and the cubes representing the leak in FEKO are assigned an oil-soil dielectric based on (5.16) and the effective porosity of the material (the available volume to be occupied by oil). This makes a leak in sand the easiest to detect since it has the largest pores and the largest effective porosity, as opposed to clay. The results of two contrasting cases are considered in more detail and the rest of the results are summarized at the end. One case is a 10-cm diameter PEC pipe in sand while the other is a 5-cm PVC oil-filled pipe in clay. The adopted scans arrangement for all simulations is shown in Fig. 5.10. The pipe is buried at 0.5-m depth right below the Tx, while the leak is centred in the middle of the three scans. To test the pipeline signal estimation, simulations are

Table 5.2: Soil Samples Used in All Simulations

Soil Type	**Composition (Sand, Slit, Clay)**	**Relative Permittivity**	**Water Content**	**Effective Porosity**
Sand	(96%,2%,2%)	$4.35 - j0.3$	1%	42.7%
Loam	(12%,44%,44%)	$6.1 - j2.1$	10%	36.3%
Clay	(2%,41%,57%)	$15.5 - j6$	30%	17.5%

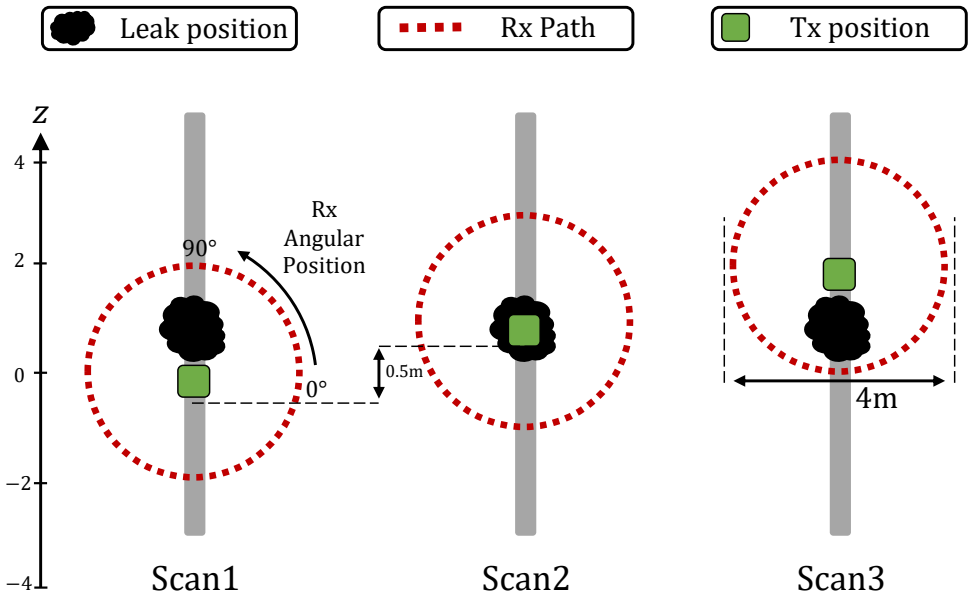


Figure 5.10: Tx-Rx scans arrangement used in all simulations, three scans are obtained where the Tx is advanced by 0.5 m relative the the previous scan while the Rx path is a circle centered around the Tx.

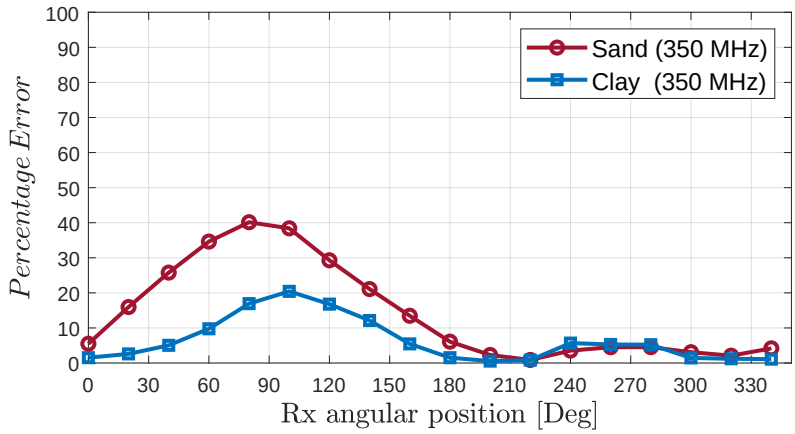


Figure 5.11: Percentage error between pipe signal obtained by simulating pipe alone and GPOF estimated pipe signal obtained from the pipe simulation in the presence of the leak, the frequency is fixed at 350 MHz and the Tx-Rx arrangement is that of the Scan1 in Fig 5.10.

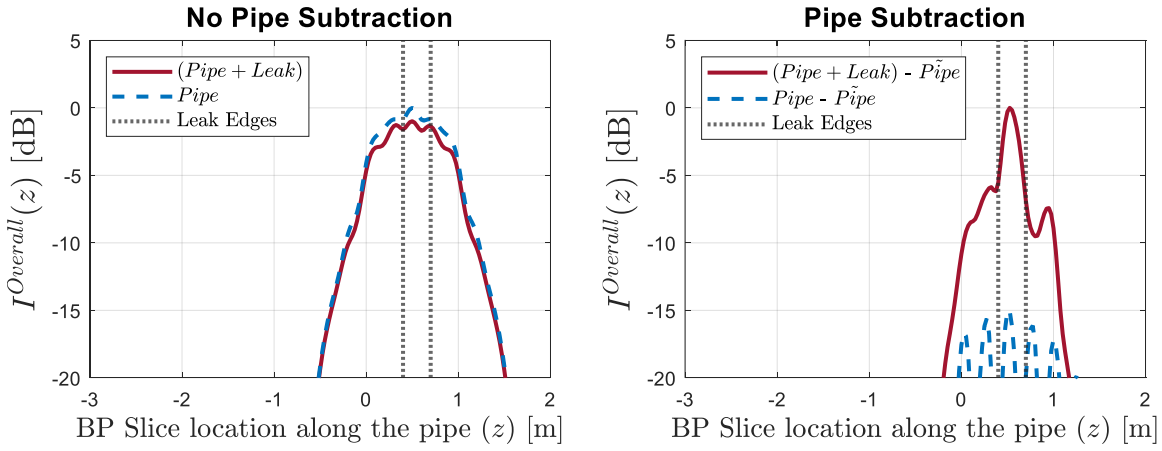
carried out for the pipe in the presence and absence of the leak. After that, the pipe signal is estimated by applying (5.7)-(5.10) to the simulation data in the presence of the leak and compared with the pipe signal obtained by simulating the pipe alone. The percentage error in pipe signal estimation is defined mathematically as follows:

$$Percentage\,Error = \frac{|V_{Pipe} - \tilde{V_{Pipe}}|}{|V_{Pipe}|} \times 100\% \tag{5.17}$$

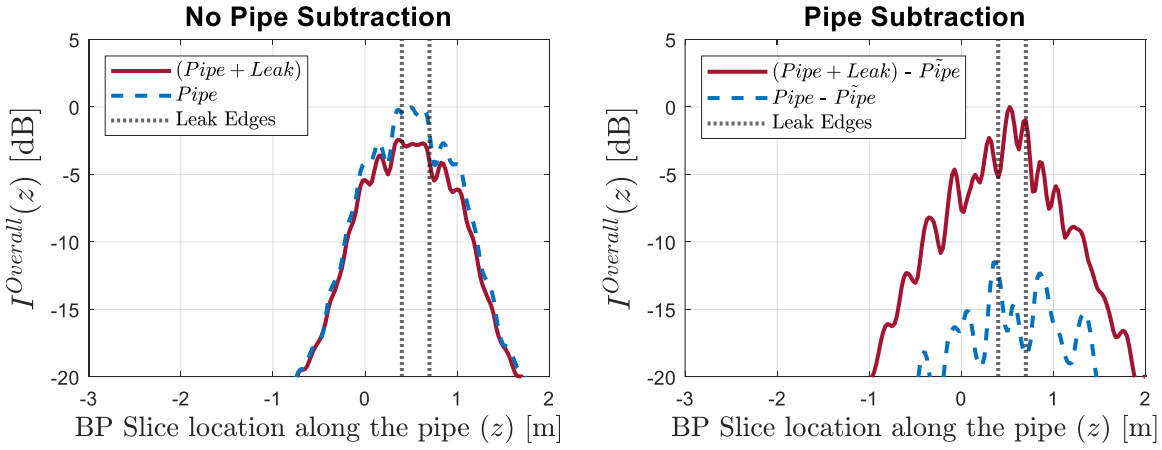
where V_{Pipe} is the pipe signal obtained by simulating the pipe without the leak and $\tilde{V_{Pipe}}$ is the estimated pipe signal obtained from the simulation of the pipe and the leak. Fig. 5.11 shows the percentage error at the center frequency for the Scan1 arrangement in Fig. 5.10. A relatively large error is observed near the direction of the leak (i.e., around the 90° angular position in Scan1) which is expected because the pipe and the leak scattering phase centers are expected to coincide along that direction, making it difficult for GPOF to separate them as two different scatterers. Moreover, the error is larger in sand since the leak spreads more in sand compared to

its spread in clay. The large error at the places where the pipe and the leak scattering phase centers coincide should not be of great concern. This is because the dominance of the pipe signal is problematic only when the pipe scattering phase centers are different from those of the leak's which leads to bright pixels in the BP image at places other than the leak. When the pipe and the leak scattering phase centers coincide, then the bright pixels will be at the leak location as desired. After confirming that the pipe signal estimation procedure works well for the cases of different pipe and leak scattering phase centers, (5.11) is applied for each scan in Fig. 5.10. Then, (5.12) is used to get the overall leak indicator from individual leak indicators, leading to leak detection. Fig. 5.12 shows the overall leak indicator for the sand and the clay with and without subtracting the pipe response for simulation data of the pipe in the presence and absence of the leak. For both sand and clay cases, there is a substantial suppression of the pipe response, indicated by the large difference between the solid and dashed lines after the subtraction. For leak localization, the results for sand show a sharp peak within the leak edges compared to the clay case whose leak is not as sharp, which is explained by the fact that the leak in clay is smaller than the leak in sand (see Fig. 5.6), giving a relatively weak response that results in a relatively less-sharp peak within the leak edges. It is worth commenting on the computational resources needed for processing the 3 scans leading to Fig. 5.12. Each trace in Fig. 5.12 is composed of 201 BP slices with each slice containing 615 pixels, the trace generation required about 5 minutes to process with a peak memory use of 6 Megabytes using Intel(R) Core(TM) i7-4702MQ CPU @ 2.20 GHz processor.

In addition to the clay and sand cases in Fig. 5.12, more cases were considered in the simulation so as to evaluate the performance in a comprehensive way. Various combinations of leak sizes (controlled by V_{th}) and pipe sizes were used. The cases are summarized in Table 5.3 where the mean power difference between the pipe and the leak signals is provided to give an idea of how apparent the leak signal is compared



(a) PEC in Sand



(b) Oil filled PVC in Clay

Figure 5.12: Overall leak indicator for (a) oil leak out of a 10 cm diameter PEC pipe in sand and (b) oil leak out of a 5 cm diameter oil-filled PVC pipe in clay. The leak detection technique is applied to simulation data for the pipe alone (dashed) and the pipe in addition to the leak (solid) to provide proper comparison.

Table 5.3: The Various Cases Considered in Simulation

Case Number	**Soil Type**	**Pipeline Material**	**Pipeline Diameter**	**Mean Power Ratio** $\frac{P_{Leak}}{P_{Pipe}}$ [dB]
1	Sand	PEC	10 cm	-13.3
2	Clay	PVC	5 cm	-11.1
3	Clay	PEC	5 cm	-28.2
4	Loam	PVC	10 cm	-12
5	Loam	PEC	5 cm	-22.9
6	Loam	PVC	7 cm	-5.1
7	Sand	PEC	13 cm	-15.6
8	Loam	PEC	8 cm	-25.2

* For all cases V_{th} is fixed to 10% of the initial value voltage value P_{in}.

to that of the pipe. To shows the performance across cases, the following figure of merit is adopted:

$$FOM = \frac{\int_{Leak} I(z)_{Pipe+Leak}^{Overall} dz}{\int_{Leak} I(z)_{Pipe}^{Overall} dz} \tag{5.18}$$

where $I(z)_{Pipe+Leak}^{Overall}$ and $I(z)_{Pipe}^{Overall}$ are the overall leak indicators calculated from the three scans in Fig. 5.10 in the presence and absence of the leak, respectively. This FOM gives an indication as to how much the peak corresponding to an actual leak (calculated by integrating the overall leak indicator over the leak region) is improved after removing the pipe response, compared to the case where there is no leak (but the pipe subtraction is still used). Fig. 5.13 shows the FOM versus the cases in Table 5.3. Without subtracting the pipe response, FOM values are very close to unity, indicating the dominance of the pipe response. In nearly all the cases, a substantial improvement in leak detection is shown after subtracting the pipe response, with the only exception being case number 3 which is as expected because it is the case with the lowest leak signal power, being more than 28 dB below the pipe signal power, according to Table 5.3.

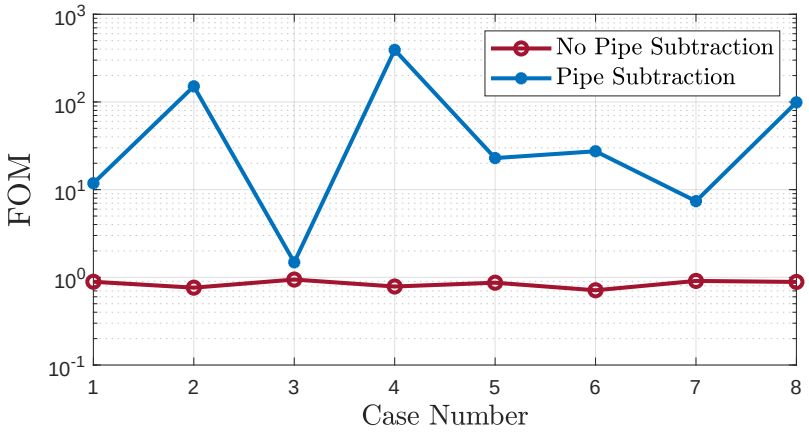


Figure 5.13: Log scale plot of FOM versus different cases of simulation.

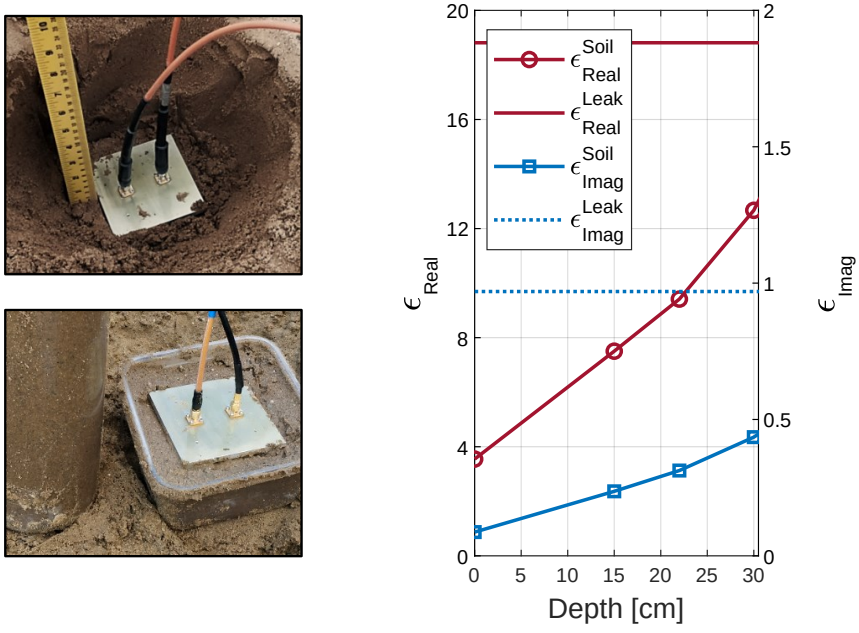
5.4.2 Measurements

To verify the proposed method experimentally, a realistic sandy environment is chosen at Silver Lake Recreation Area in Pinckney, Michigan, USA (see Fig. 5.14a). To represent the leak, several plastic containers are filled with sand from the same place and saturated with water as shown in Fig. 5.14b. With the help of a portable vector network analyzer (VNA) and the same ring resonator used to characterize the oil-sand dielectric, the dielectric profile of the sand versus depth as well as the dielectric constant for the leak are measured on site and displayed in Fig. 5.15. The sand dielectric profile increases with depth due to higher concentration of water in the deeper layers. After characterizing the sand dielectric profile, four experiments were carried out. Two experiments used a metallic as well as water-filled PVC pipes with the leak (Fig. 5.16), and the other two use the same pipes without the leak, to provide a reference for comparison. We used water leak as opposed to oil leak for environmental safety. However, a very small volume for the leak region is chosen to compensate for the higher water-sand dielectric mixture compared to that of the oil-sand mixture. All experiments have an identical setup, which is shown in Fig. 5.17. There is a moving Rx that collects the scattered signal samples for each bistatic measurement (scan) during which the Tx is fixed. As discussed earlier, the best arrangement for the Rx



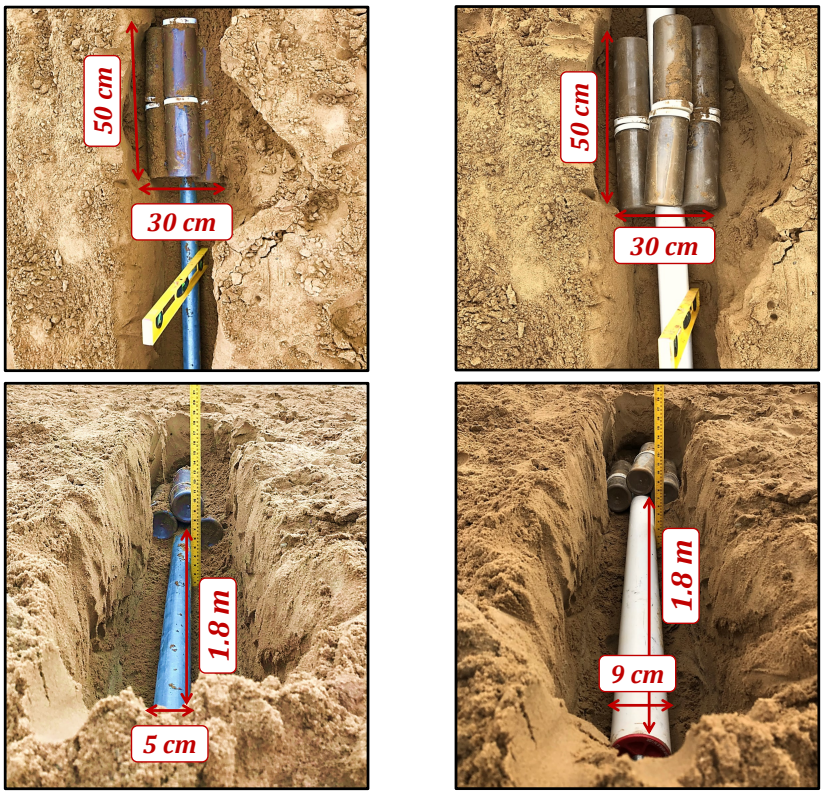
(a) (b)

Figure 5.14: (a) Experiments location near Silver Lake (b) plastic containers filled with water saturated sand to represent the leak.



(a) (b)

Figure 5.15: (a) Ring resonator measuring sand and leak dielectric (b) dielectric profile of sand along with the leak.



(a) Metallic (b) Water filled PVC

Figure 5.16: The buried pipes and the leak used in the experiments.

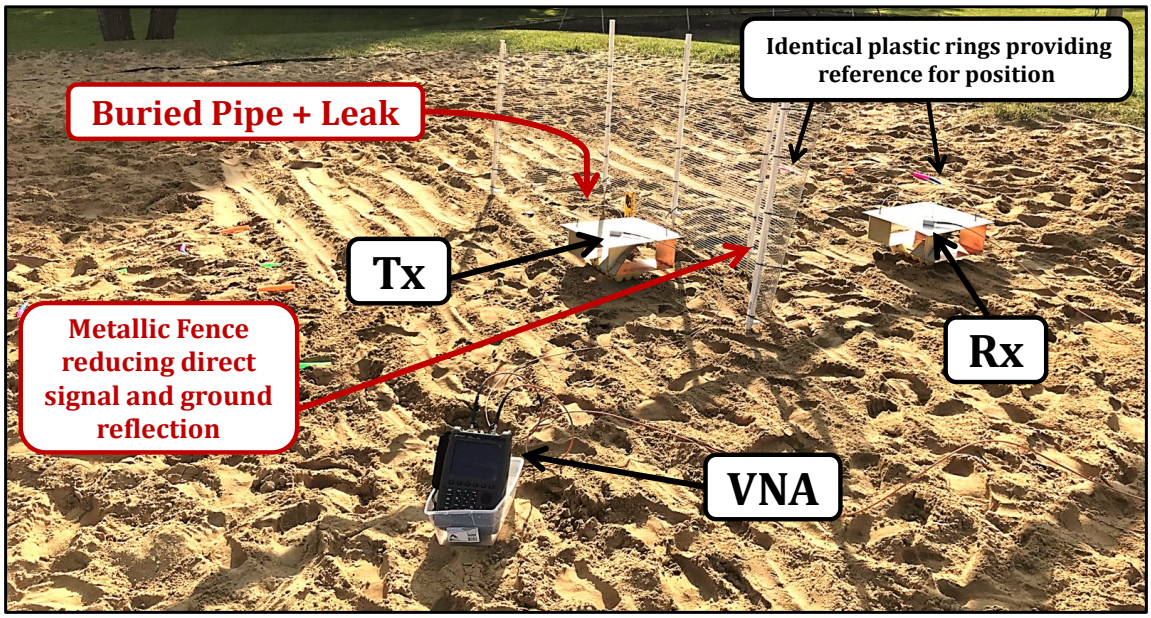


Figure 5.17: Experimental setup for VNA based bi-static subsurface SAR used in all experiments.

samples is on a circle so as to provide a uniform azimuthal cross-sectional resolution. However, due to the difficulty of manually arranging Rx samples on a perfect circle, a more practical arrangement was adopted in the experiments. Moreover, the limited space in the experiment site made it difficult to move the Rx samples along with the Tx in each scan like what was done in the simulation. As a result, three sets of bistatic measurements (scans) were performed where the Tx is fixed at different locations while the Rx samples are collected on the same configuration as illustrated in Fig. 5.18. It should be noted that this new arrangement may not be optimal if the leak is spread laterally instead of along the pipe, but it works fine for our situation in which the leak is spread along the pipe. Furthermore, as discussed in Chapter 3, a metallic fence is placed in-between the Tx and the Rx to reduce the direct signal from the Tx and the ground reflection signal that are much stronger than the signals from the pipe and the leak. The Tx and Rx have identical out-of-phase fed ENVELOPE antennas designed for subsurface radars and discussed in [78]. All the pipes are buried at 35 cm depth and displaced 30 cm horizontally from the Tx positions. For each Rx position, the VNA collects S_{21} data over the range 200-500 MHz in 1-MHz increments to give enough data points for applying the GPOF procedure. The collected S_{21} data at each Rx is calibrated by the following three steps. At first, the delay and attenuation caused by the cables is compensated for by dividing the measured data by S_{21}^{cable}, which is the measured response of the cables when they are connected together. After that, the signal is transformed into the time domain and time gating is applied to eliminate any signal outside the expected range. Finally, the signal is transformed back to the frequency domain to apply the leak detection procedure. Mathematically, the steps are expressed by:

$$S_{21}^{Cal}(\omega, Rx_n) = \mathit{fft}\left(\mathit{ifft}\left(\frac{S_{21}(\omega, Rx_n)}{S_{21}^{Cable}(\omega)}\right) \times W(t - t_n)\right) \tag{5.19}$$

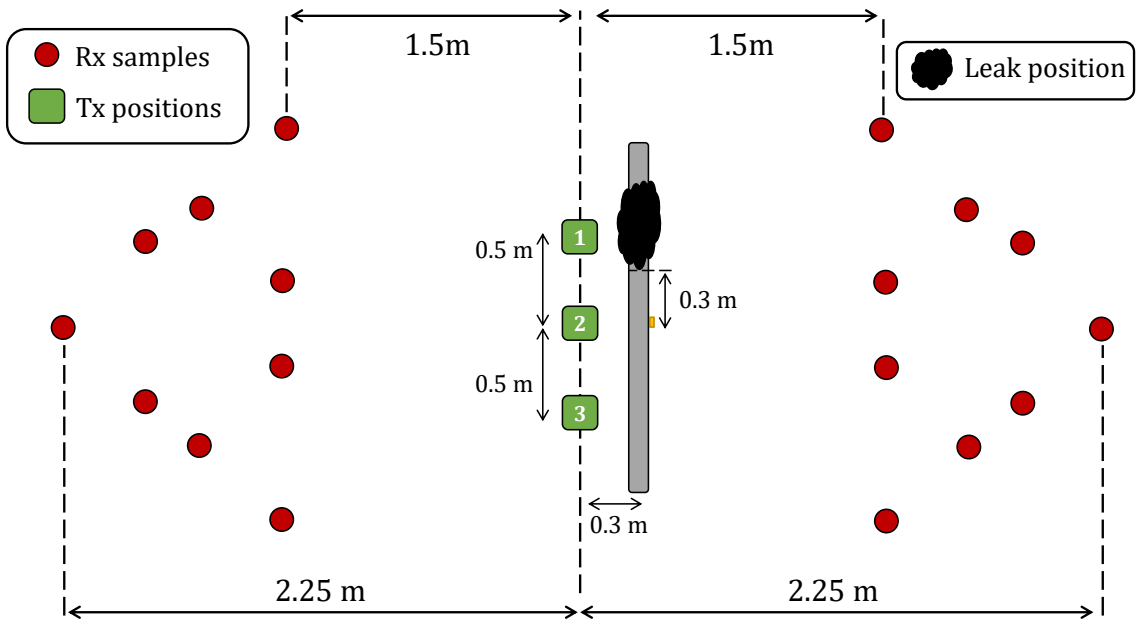
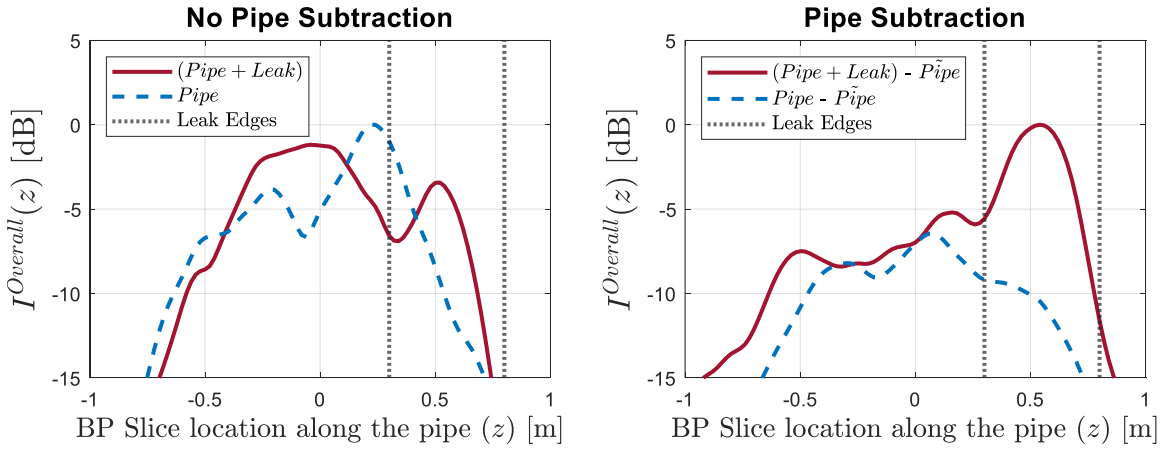
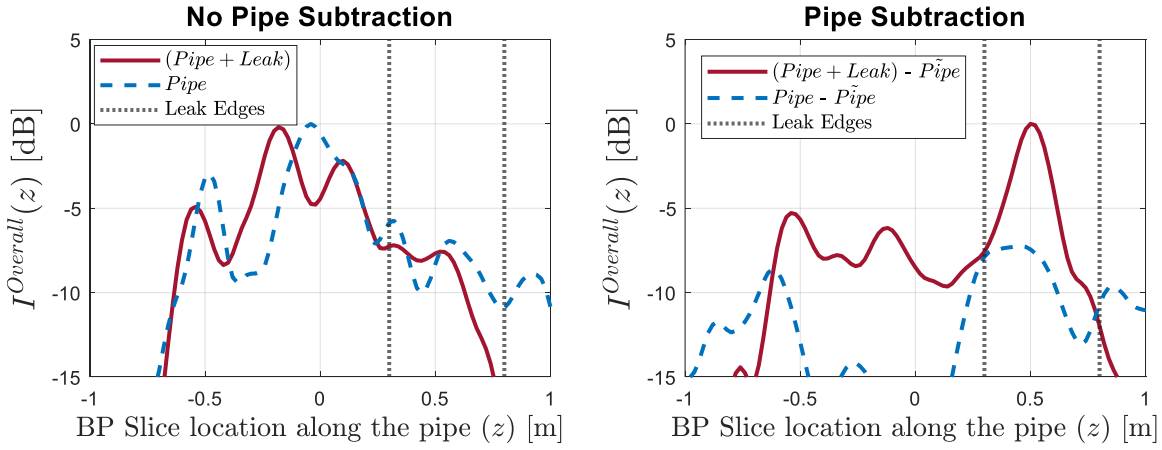


Figure 5.18: Tx-Rx scans arrangement used in all experiments. The Tx is fixed in positions 1,2 and 3 for scans 1,2 and 3 respectively while Rx samples are on the same position for each scan.

where $W(t-t_n)$ is a Gaussian window of 25-ns width and t_n is the time delay caused by the pipe phase obtained from (5.4). After calibration, S_{21}^{Cal} is used in (5.7)-(5.12) to calculate the overall leak indicator of the three bistatic SAR measurements (scans). Fig. 5.19 shows the overall leak indicators calculated with and without subtracting the estimated pipe response for the metallic as well as the PVC pipes. In both cases, a clear peak of more than 6 dB is shown within the leak edges for the overall leak indicator constructed from the experiments conducted on the pipe in addition to the leak, compared to the experiments conducted on the pipe alone.



(a) Metallic pipe



(b) Water filled PVC pipe

Figure 5.19: Overall leak indicator obtain from Scans 1, 2 and 3 for (a) the metallic pipe and (b) the water filled PVC pipe. The leak detection technique is applied to measured data for the pipe alone (dashed) and the pipe in addition to the leak (solid) to provide proper comparison.

5.5 Conclusion

In this Chapter, a novel technique to improve leak detection and localization using multi-static wideband subsurface 3D imaging radar is proposed. The technique is based on decomposing the radar response into a set of exponential terms using the generalized pencil of function procedure. After that, the unique way a pipeline scatteres EM waves for the multistatic SAR configuration is utilized to identify the pipeline contribution among the exponential terms and eliminate it from the overall radar response. A back-projection algorithm is applied to the remaining radar response to detect and localize the leak. To test the performance of the technique, a physics-based soil-leak model, in combination with a semi-empirical oil-soil dielectric model, are used in a full-wave simulator to get a realistic scattered-leak signal. Extensive simulations were carried out for various types of soils using metallic as well as PVC pipes of different sizes. The simulation results show the technique's ability to detect a leak even in cases where the leak's signal is lower than the pipe's signal by more than 20 dB. Finally, the technique is further validated by carrying out a field experiment for a water leak out of PVC as well as metallic pipes, showing that small leaks can easily be detected.

CHAPTER 6

A Method for Signal Leakage Cancellation in Multistatic SAR

6.1 Introduction

One of the challenges arising from the use of multistatic subsurface SAR is signal leakage. When the Tx illuminates the underground, it sends at the same time a direct signal to the Rx as well as a signal that reflects from the ground and reaches the Rx. The direct and ground reflection signals are referred to as signal leakage and they are undesirable because they convey no information about the buried targets. Furthermore, as opposed to the buried-targets signals that travel through lossy soil, the signal leakage travels through air and suffers less attenuation, making it much stronger than target signals, thereby saturating the Rx and preventing buried-targets detection. Adopting the multistatic subsurface SAR system shown in Fig. 6.1, this chapter presents a null-synthesis signal leakage cancellation technique. Utilizing the knowledge of the Tx and Rx sampling locations, the received signals at each two adjacent Rx positions are processed together so as to form a two-element receiving array that has a null in the direction of the Tx do as to eliminate such signal leakage before SAR processing. In the following, Section 6.2 provides the signal model and explains the array null-steering procedure, and Section 6.3 provides the imaging algorithm tailored to the designed two-element arrays. Finally, simulation and measurements

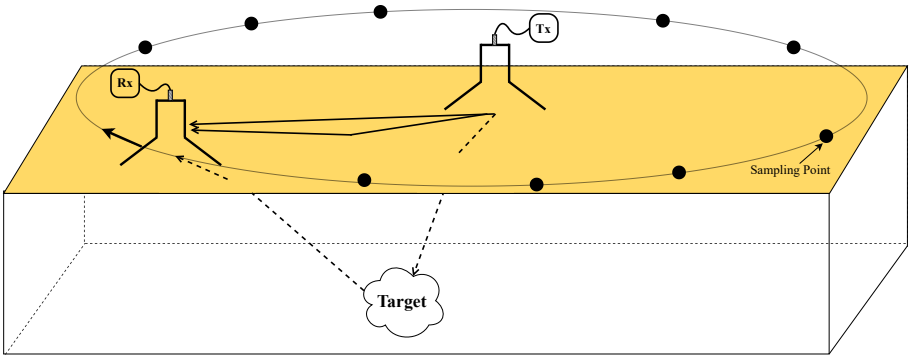


Figure 6.1: Multi-static subsurface SAR used in this work. The direct and ground reflections (solid lines) have similar paths compared to the target signal (dashed) since the Tx and Rx are very close to ground.

results demonstrating the effectiveness of the technique are provided in Section 6.4.

6.2 Signal Leakage Elimination

To model the soil medium in a realistic way, the air-soil interface is considered relatively smooth with an rms height on the order of few centimeters. Since the free-space wavelength at the center frequency of the radar is about 1 meter, such a surface can be considered flat. To permit a tractable solution, the soil medium is considered homogeneous. The layered nature of some soil media can also be considered in the forward model but it makes the formulation somewhat lengthier. With these simplifications, the geometry of the problem becomes the one shown in Fig. 6.1. There is a fixed transmitter (Tx) and a moving receiver (Rx) that samples the received signal around the Tx. Assuming point scatteres with no mutual interactions with the transmitter and the receiver as well as $e^{j\omega t}$ time dependence, the received voltage across the n^{th} Rx terminals at the m^{th} frequency is given by:

$$V_{mn} = \frac{A_m^{dg}}{(R_n^{dg})^2} e^{-jk_m^{Air} R_n^{dg}} + \sum_s A_{mn}^s e^{-jk_m^{Soil} R_n^s} \tag{6.1}$$

where k^{Air} and k^{Soil} are the propagation constants in air and soil, A^i_{mn} and R^i_n are the amplitude and the signal path, respectively, for the direct and ground signal ($i = dg$) and the signals from the arbitrary number of scatterers (targets) under the ground ($i = s$). Because the Tx and Rx are assumed to be very close to the ground surface, two assumptions are implicit in (6.1). First, the phase from the targets' scattered signals is assumed to be resulting from propagation in the soil medium only. Second, the ground signal and the direct signal interfere destructively and as a result, the propagation decay is on the order of $\frac{1}{R^2}$, as discussed in [102, 88]. Furthermore, the radiation patterns of the Rx and Tx antennas are embedded in the amplitude coefficients. Also, the propagation decay for the targets' signals is subsumed in the amplitude coefficient A^s_{mn} for brevity. To eliminate the direct and ground reflection signals, the signals from two adjacent Rx positions are processed together as a two-element receiving array with a proper phase to create a null in the direction of the Tx. Mathematically, the voltage across the array's terminals is calculated as:

$$V^{Array}_{mn} = a_{mn}\, V_{m(n+1)} - V_{mn} \tag{6.2}$$

where a_{mn} is a complex weighing factor given by:

$$a_{mn} = \left(\frac{R^{dg}_{n+1}}{R^{dg}_n}\right)^2 e^{-jk^{Air}_m (R^{dg}_n - R^{dg}_{n+1})} \tag{6.3}$$

Basically, this factor adjusts the amplitude and the phase of $V_{m(n+1)}$ to make the direct and ground reflection signal term in $V_{m(n+1)}$ and V_{mn} the same so that subtracting the two cancels the term but doe not impact the scattered signals from buried targets. Note that the location of the Tx and the Rx points are known within a fraction of the wavelength, which is a crucial aspect of the cancellation since inaccurate positioning

will cause imperfect leakage cancellation. Keeping such cancellation in mind and expanding the terms in (6.2) using (6.1) leads to:

$$V_{mn}^{Array} \approx \sum_{s} A_{mn}^{s}(a_{mn}\, e^{-jk_m^{Soil}R_{n+1}^{s}} - e^{-jk_m^{Soil}R_n^{s}}) \tag{6.4}$$

Here, it is assumed that the amplitude variation in A_{mn}^{s} is very small and thus we can use $A_{m(n+1)}^{s} \approx A_{mn}^{s}$. To simplify (6.4) into a more readable form, Euler and sum-to-product trigonometric identities can be used to show that:

$$e^{-jA} - e^{-jB} = \frac{2}{j} sin(\frac{A-B}{2})\, e^{-j\frac{A+B}{2}} \tag{6.5}$$

and considering that $|a_{mn}| \approx 1$ (for closely spaced sampling points), and with the use of (6.5), the final form of (6.4) becomes:

$$V_{mn}^{Array} \approx (\frac{2}{j}) \sum_{s} sin(\Delta_{mn}^{s-}) A_{mn}^{s} e^{-j\Delta_{mn}^{s+}} \tag{6.6}$$

where,

$$\Delta_{mn}^{s\pm} = \frac{1}{2}\left(k_m^{Soil}(R_{n+1}^{s} \pm R_n^{s}) + k_m^{Air}(R_n^{dg} - R_{n+1}^{dg})\right) \tag{6.7}$$

This form shows that the received signal at the array's terminals will contain only the scattered signals from the targets, modified by a sinusoidal factor. Such a factor causes two minor issues in imaging. First, any target for which $\Delta_{mn}^{s-} = 0$ will be in the blind spot of the array but that can only happen to a small fraction of the receiver points, unless the target is located exactly below the Tx. To avoid such a

scenario, multiple Tx-Rx configurations should be considered where the Tx is moved to a new location for each configuration, then the results of all configurations should be processed coherently at the end. The second issue caused by the sinusoidal term is the sign flip that occurs when $\Delta_{mn}^{s-} > 0$ for some values of n and $\Delta_{mn}^{s-} < 0$ for other values, leading to additional 180 degree phase that needs to be accounted for by the imaging algorithm. Taking these issues into consideration, the following section describes the imaging algorithm, which is a modified version of the well-known back projection (BP) algorithm.

6.3 Imaging Algorithm

Given the receiver data at each Rx location and frequency $\{V_{mn}\}$, as well as accurate knowledge of the Rx and the Tx locations, the aim of the imaging algorithm is to form a 3D image of the underground targets while eliminating the contribution of the direct and ground reflection signals. To accomplish this, the following steps are taken:

1. Define a global Cartesian coordinate system in which (x, y, z) represent the coordinates of a point in the 3D image space.

2. Choose a pair of synchronized transmitter and receiver where the Tx is fixed and the Rx collects data around the Tx with high spatial resolution. Then form a large number of two-element arrays and calculate their received voltages V_{mn}^{Array} using (6.2).

3. Pick an imaging point $p = (x, y, z)$ in the image space and form the image by assuming there is a target at this point using:

$$I^i(p) = \sum_{m=1}^{M} \sum_{n=1}^{N-1} sgn(sin(\Delta_{mn}^{p-}))V_{mn}^{Array} e^{j\Delta_{mn}^{p+}} \quad (6.8)$$
$$\Delta_{mn}^{p\pm} = \frac{1}{2}\left(k_m^{Soil}(R_{n+1}^p \pm R_n^p) + k_m^{Air}(R_n^{dg} - R_{n+1}^{dg})\right)$$

where $I^i(p)$ is the image at point p for the i^{th} Tx location (for each Tx location a new image is formed) and R_n^p is the total signal path from the Tx to the imaging point p and from that to the n^{th} Rx location. Here, the signum function (sgn) is used to correct for the sign flip introduced by the sinusoidal factor in (6.6).

4. Repeat step (3) for all possible imaging points.

5. Save the 3D image for that particular Tx location.

6. Move to another Tx location and repeat steps (2) to (5).

7. Sum the constructed 3D images formed by all Tx locations to from the final image:

$$I(p) = \sum_{i=1}^{N_i} I^i(p) \quad (6.9)$$

In the final image, bright spots will appear at the locations of actual targets due to the coherent addition of phase-compensated signals.

6.4 Simulation and Measurement Results

Using the direct and ground reflection signal elimination method, the following subsections present the performance evaluation for the method using simulation data for buried metallic spheres and actual measurement data for a buried metallic pipeline.

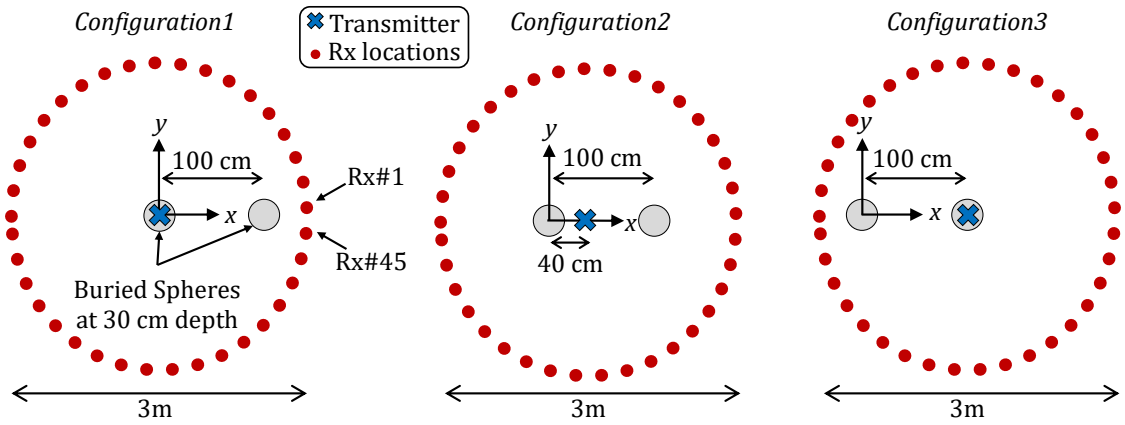


Figure 6.2: Top view of the three configurations used in simulation along with the buried spheres, configuration 1 is at the center of the coordinates while configuration 2 and 3 are shifted 40 and 100 cm respectively along the x direction. It should be noted that the spheres are fixed with respect to the coordinates.

6.4.1 Simulation

Full-wave simulation software FEKO is used to generate the field data for a bistatic subsurface imaging system. The scenario considered is for two metallic spheres of 10 cm diameter buried at 0.3-m depth inside a sand medium with a relative dielectric constant of 6. Simple Tx and Rx antennas (Hertzian dipoles) are used in this simulation and are located 5 cm above the sand-air interface. To avoid the problem of the blind spot for objects located right below the Tx, the data are acquired for three different Tx-Rx configurations. In each case, for a fixed Tx location, 45 equally spaced Rx samples are collected along a 3m diameter circle centred at the Tx location. Fig. 6.2 provides a top view of the different Tx-Rx configurations and the buried spheres. The frequency range considered is 100-500 MHz with 10 MHz frequency increments. Before applying the imaging algorithm, the time-domain signals for two adjacent Rx locations as well as the time-domain signal for the array formed using (6.2) are plotted in Fig. 6.3. A substantial suppression for the direct and ground reflection signals is shown while the spheres' signals are enhanced after the removal of the large Tx signal leakage. After confirming the unwanted signal cancellation, the imaging algorithm

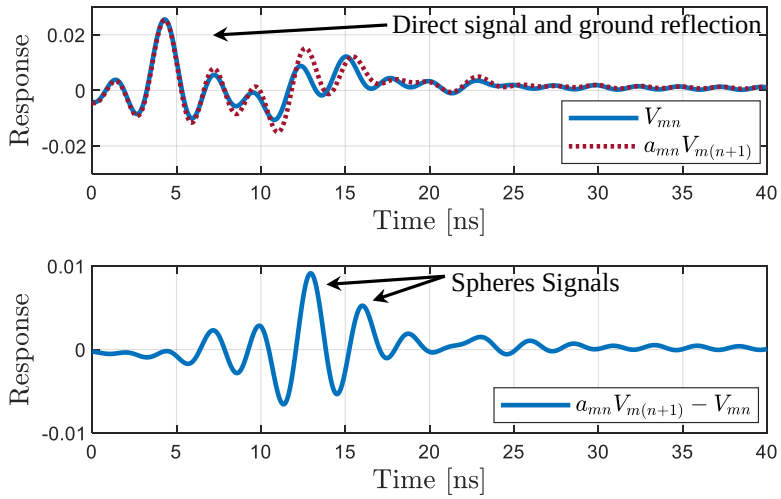


Figure 6.3: Time domain signals for Rx location numbers 26 and 27 in Configuration 1 in Fig. 6.2 along with the time signal for the array constructed using (6.2). Direct and ground reflections signals are cancelled while the spheres signals are enhanced.

is used to reconstruct the buried spheres. At first, the algorithm is performed using Configuration1 in Fig. 6.2 only. To demonstrate image improvement using leakage cancellation, two images are reconstructed, one is reconstructed from processing the collected data directly using the BP algorithm and the other is reconstructed using the proposed leakage cancellation technique. Fig. 6.4 shows an X-Y cut of the reconstructed 3D images. The effect of eliminating the direct and ground signals using array null-steering is very clear, which has led to a much better image for the sphere located at x=1. However, the sphere located below the Tx (x=0) is not imaged well since it is located along the blind spot of the two-element arrays. As suggested above, using the data from multiple Tx-Rx configurations mitigates this problem since the blind spot is changing with each configuration, allowing the object that is on the blind spot of one configuration to be imaged by the other configurations. Fig. 6.5 shows the reconstructed image using all three configurations in Fig. 6.2. Here, it is shown that both spheres are clearly imaged at their proper locations. It should be noted that the geometry of the spheres in the image appears to be more extended along the

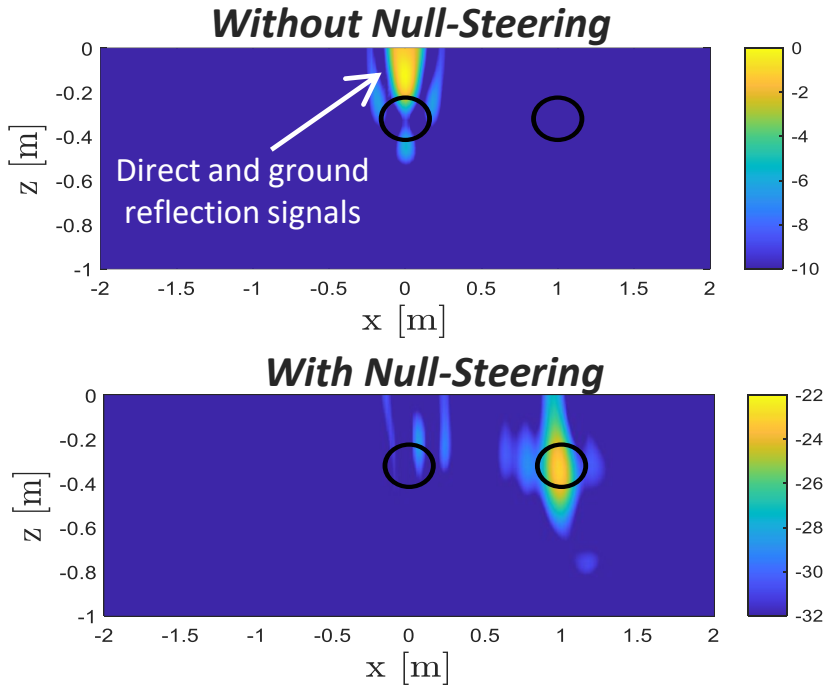


Figure 6.4: An X-Z (Y=0) cut of the reconstructed 3D image with and without null-steering using Configuration1 in Fig. 6.2 only. The actual spheres locations are indicated by black circles. dB scale is used and both images are normalized to the same maximum.

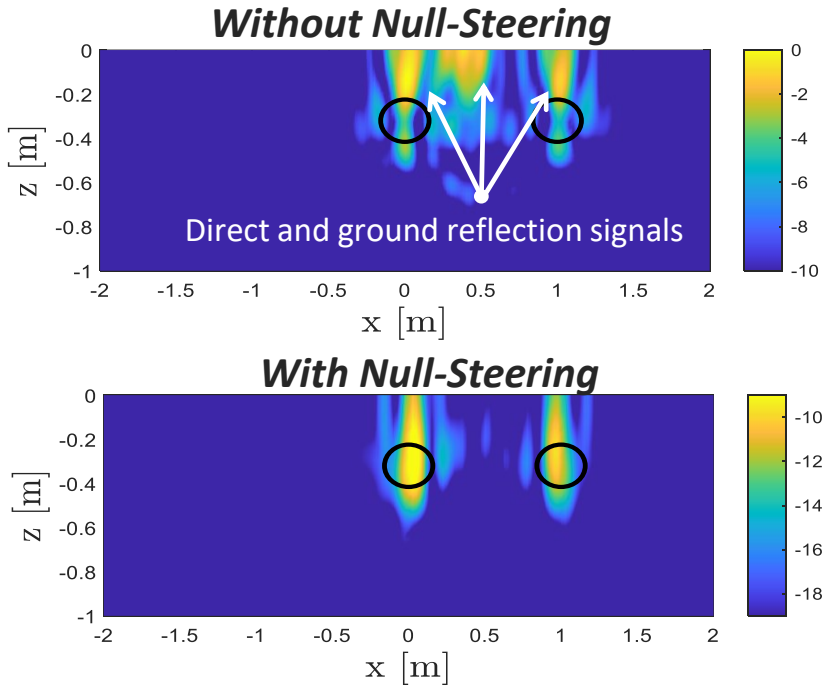


Figure 6.5: An X-Z (Y=0) cut of the reconstructed 3D image with and without null-steering using all the configurations in Fig. 6.2. The actual spheres locations are indicated by black circles. dB scale is used and both images are normalized to the same maximum.

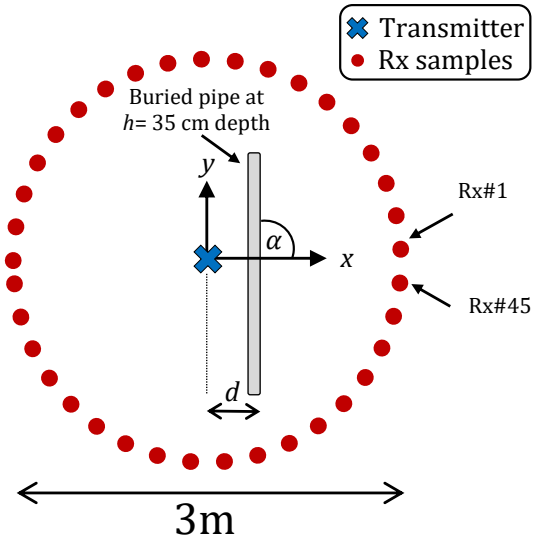
range direction (z) compared to the cross-range direction (x). This is expected as the resolution along the range direction is controlled by the radar bandwidth which is quite restricted, compared to the cross-range resolution which is controlled by the effective length of the synthetic aperture, which can be made larger by choosing the Rx samples locations appropriately.

6.4.2 Measurements

To test the performance of the proposed method experimentally, a realistic sandy environment is chosen at Silver Lake Recreation Area in Pinckney, Michigan, USA (see Fig. 6.6a). The experiment was conducted using a 5-cm diameter metallic pipeline with the experimental setup shown in Fig. 6.7. There is a fixed Tx in the middle and an Rx that is moved along a circular path of 3-m diameter, centered at



(a)



(b)

Figure 6.6: Experiments location near Silver Lake (a) and the Tx-Rx arrangement used in the experiment along with the buried pipe (b).

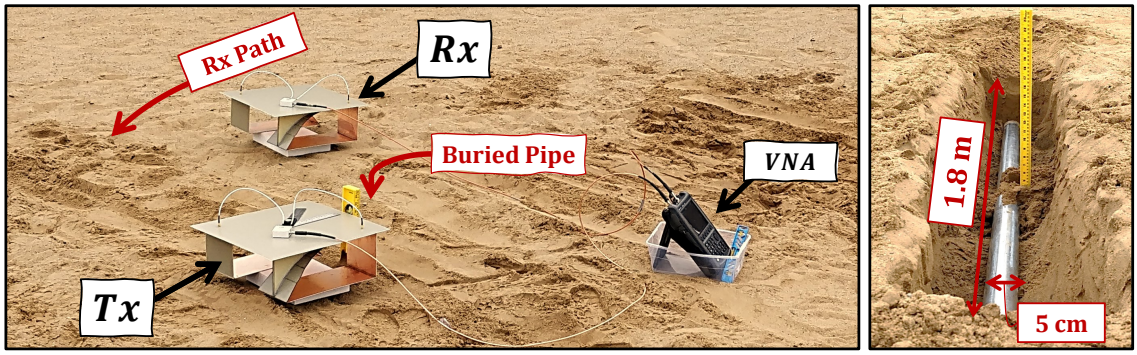


Figure 6.7: The VNA based subsurface bistatic SAR setup used in the experiment along with the buried metallic pipeline.

the Tx location. In the experiment, 45 equally spaced samples are collected as shown in Fig. 6.6b. The Tx and Rx are located 5 cm above the ground and the system used ENVELOP antennas designed specifically for subsurface radars as discussed in [78]. As the Rx is moved around the circle, a portable vector network analyzer (VNA) is used to collect S_{21} data over the frequency range 100-500 MHz in 2-MHz increments. The measured S_{21} at each Rx location is processed to remove the delay and attenuation caused by the cables, providing the data for imaging. Here, as in the simulation, the time-domain signal for two adjacent Rx locations, along with the time-domain signal for the array formed by (6.2), are plotted in Fig. 6.8. The plots clearly indicate that the subtraction leads to much better enhancement for the pipe signal and can significantly suppress the direct and ground reflection signals. For imaging the pipe, there is a slight change in the algorithm that needs to be done. Since the pipeline is an extended object, applying the BP-based imaging formula (6.8) does not work well as it is designed for point scatterers. Instead, the pipeline detection algorithm proposed in Chapter 3 is used. Basically, instead of forming an image at each point $p = (x, y, z)$ in the image search space, the search is conducted for each point $q = (\alpha, d, h)$ in the pipeline parameters search space, where α, d, h represent the pipeline orientation, displacement, and depth ,respectively, as indicated in Fig. 6.6b. Mathematically:

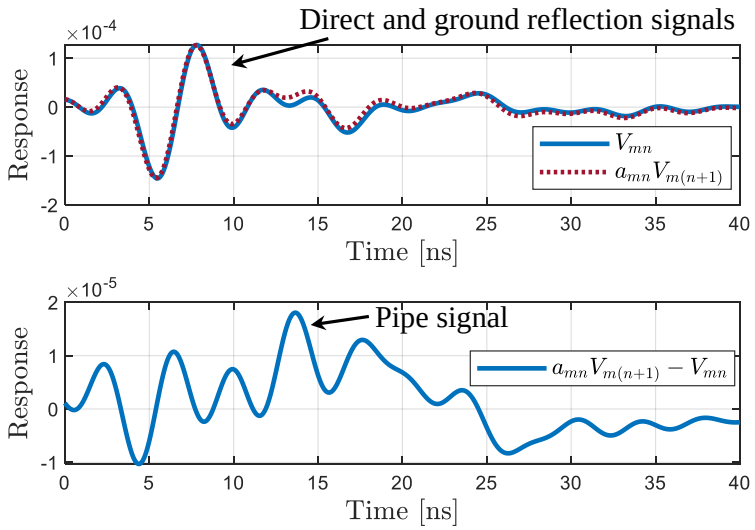


Figure 6.8: Time domain signals for Rx location numbers 11 and 12 in Fig. 6.6b along with the time signal for the array constructed using (6.2). Direct and ground reflections signals are cancelled while the pipe signal is enhanced.

$$I(q) = \sum_{m=1}^{M} \sum_{n=1}^{N-1} sgn(sin(\Delta_{mn}^{q-}))V_{mn}^{Array} e^{j\Delta_{mn}^{q+}} \tag{6.10}$$
$$\Delta_{mn}^{q\pm} = \frac{1}{2}\left(k_m^{Soil}(R_{n+1}^q \pm R_n^q) + k_m^{Air}(R_n^{dg} - R_{n+1}^{dg})\right)$$

where $I(q)$ is the value of the search at point q in the pipeline parameters search space and R_n^q is the total signal path from the Tx to the scattering phase center due to a pipeline with parameters q and from that to the n^{th} Rx location as detailed in Chapter 3. Using this modified search, Fig. 6.9 shows an $h - d$ cut from the 3D pipeline parameters search space where α is fixed to 90, the actual pipeline orientation. The figure shows the results when applying the search to the data directly without the array null-steering as well as the search after applying the array null-steering. Without the array null-steering, a peak is shown at the top around zero depth which results from the direct and ground reflection signals. After the array null-steering, the peak associated with the direct and ground reflection signals is partially suppressed

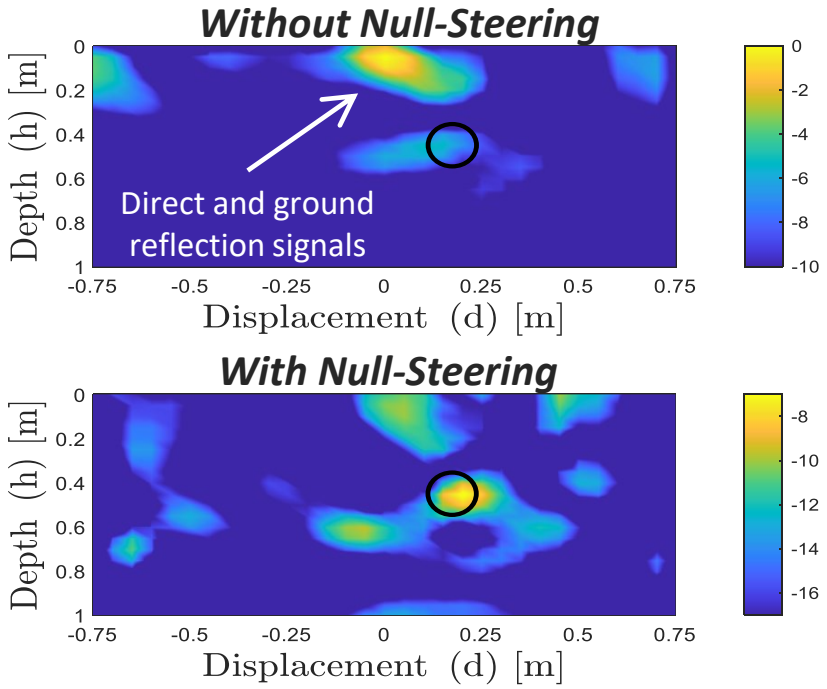


Figure 6.9: An h-d cut out of the 3D pipeline parameters search space where α is fixed at 90 degrees. The actual pipe parameters are indicated by a black circle. dB scale is used and both searches are normalized to the same maximum.

making the peak associated with the actual pipeline parameters the global maximum of the search space, and hence, detection and localization are achieved. The partial but not complete suppression of the leakage signal is largely attributable to errors in measuring the Tx and Rx locations.

6.5 Conclusion

In this Chapter, an effective technique to eliminate the adverse effects of the signal leakage in multistatic subsurface SAR is presented. The technique works by combining the received signals in adjacent sampling points to form a two-element receiving array that has a null in the direction of the Tx. A signal model is described, the details of the algorithm and the potential problems that could arise from array null-steering are discussed. Furthermore, a modified BP-based imaging algorithm suited for the array is provided. Finally, the technique's effectiveness is tested against simulation data for buried metallic spheres as well as measurement data for a buried metallic pipeline. Both simulation and measurement results show significant suppression of the direct and ground reflection signals and an enhanced image quality.

CHAPTER 7

Conclusions and Future Work

7.1 Summary and Conclusions

The work in this dissertation deals with developing algorithms and techniques that enable the detection and localization of buried pipelines and their leaks using a 3D multistatic subsurface synthetic aperture radar (SAR) configuration. To accomplish this goal, the dissertation starts with introducing a novel fast full-wave simulation method that the utilizes reciprocity theorem to allow for time-efficient computation of the induced voltage across the radar receiver's terminals due to an arbitrary number of buried targets that can be either metallic or dielectric objects. The data generated by the fast method was validated by comparing it to the results obtained from a conventional full-wave simulation and the results showed excellent agreement between the two methods. It is shown that the fast method achieves a factor of $\frac{N}{2}$ increase in speed over the conventional approach, where N is the number of SAR receivers. This is followed by developing an algorithm for detection and localization of widely-spaced buried pipelines. The algorithm tracks the scattering phase centers along the pipelines and focuses the SAR received signals, leading to detection and localization of the buried pipelines. The algorithm was validated by applying it to a full-wave simulation dataset as well as to measured data. Knowledge of the scattering phase center locations is then utilized to devise another algorithm for detection

and localization of closely-spaced buried pipelines. The new algorithm uses the scattering phase centers to develop a 3D forward-scattering model, predicting the phase and amplitude of the scattered fields due to multiple buried pipelines in multistatic SAR. The forward model is used to define an objective function that is minimized by a dynamic-grid search-based procedure leading to the detection and localization of buried pipelines that fall below the range and cross-range SAR resolutions. The new algorithm is validated by comparing its performance with the earlier phase compensation (focusing)-based algorithm using simulations and measured data showing the new algorithm's ability to resolve closely spaced pipelines. An important point to emphasize is that due to the high SAR processing gain, the probability of detection of buried pipelines using the two novel algorithms is far superior to the standard GPR systems that read the scattered signal directly without processing. Building on the pipelines focusing algorithm, the dissertation proposes a technique for detection and localization of buried pipeline leaks. The technique utilizes knowledge of the scattering phase center's locations along the pipeline to estimate its contribution to the radar response. After that, the pipeline contribution is eliminated leading to leak detection. The technique is validated by applying it to both full-wave simulation and measured data. Lastly, the dissertation addresses the direct Tx-Rx signal leakage challenge in multistatic SAR configuration. The challenge is addressed by proposing an array null-synthesis procedure that nulls out the signal leakage, allowing for better detection of buried targets signals. The procedures is tested on full-wave simulation data in addition to measured data.

7.2 Dissertation Contributions

The following is a detailed account of the dissertation's contributions:

7.2.1 Development of Fast Full-Wave Simulation Method for Deeply Buried Targets in 3D Multistatic SAR

The fast full-wave simulation method proposed in the dissertation is meant to address the time-consuming aspect of simulating multistatic SAR. Most of the time consumption happens because of the need to perform a new simulation each time the SAR Rx moves to a new position with respect to the Tx. The dissertation dealt with the problem by decomposing the full-wave simulation into two steps. In the first step, the Tx illuminates the underground targets, inducing a current distribution within the targets spatial extent or on their surfaces. In the second step, the induced current distribution radiates the scattered field, causing an open-circuit voltage across the Rx terminals. Following this reasoning, the proposed method showed that it was sufficient to perform a full-wave simulation for the Tx and the buried targets to calculate the induced current distribution once and save the resulting data. After that, another simulation is performed by using the Rx as a transmitter above the soil surface and the resulting field is calculated everywhere inside the soil medium. Then, the reciprocity theorem is used to link the targets current distribution to the Rx's field, leading to a time-efficient formula for calculating the Rx open-circuit voltage due to the buried targets at any Rx position. Using this method, the overall full-wave simulation time for multistatic subsurface SAR is reduced by a factor of $\frac{N}{2}$, where N stands for the number of voltage samples needed to perform SAR imaging.

7.2.2 Development of a Dynamic Focusing Algorithm for Buried Pipelines Detection and Localization in 3D Multistatic SAR

A major contribution of this dissertation is the development of an algorithm tailored to the dynamic nature of pipeline's scattering phase centers (SPCs) . Because pipelines

are extended targets, they don't have a fixed SPC for all Rx and Tx positions. Instead, their SPCs keep moving along the pipelines depending on the relative Tx and Rx positions to ensure phase propagation along the specular scattering direction as dictated by the analytical solution of the pipelines' scattered field. To address this dynamic SPCs phenomena that makes pipelines incompatible with traditional point-target based SAR focusing algorithms, the dissertation proposes a novel algorithm that tracks the SPC for all Tx and Rx positions, leading to successful SAR focusing. The algorithm starts by describing the phase propagation path geometrically leading to a closed-form solution to the pipeline SPC location for each Rx position. After that, the algorithm utilizes the knowledge of the SPC locations to calculate the total bistatic pathlength from the Tx to the SPC and from the SPC to the Rx. The pathlength is then used to calculate the resulting propagation phase and to focus the pipelines scattered field signals across all Rx positions. The focusing leads to revealing the buried pipelines depth, and lateral displacement as well as orientation.

7.2.3 Development of an Optimization-Based Inversion Algorithm for Closely-Spaced Buried Pipelines Detection and Localization in 3D Multistatic SAR

The phase compensation (focusing)-based pipeline detection and localization algorithm developed in this dissertation suffers from finite range and cross-range resolutions. To overcome this limitation, the dissertation proposes a 3D forward scattering model and a new inversion algorithm for detection and localization of closely-spaced buried pipelines. The forward scattering model calculates the locations of the pipelines SPCs for all Rx positions. After that, the model accounts for propagation phase and amplitude attenuation, leading to the calculation of the resulting complex Rx voltage due to the scattered field from the buried pipelines. The forward model

is then used to define an objective function, which is the misfit between the forward model and the measured Rx voltages. The objective function is then minimized by a dynamic grid search-based procedure and the minimization leads to the detection and localization of closely-spaced pipelines. Because of the utilization of both amplitude and phase of the scattered field, this new inversion algorithm is shown to be superior in performance to the basic focusing-based algorithm that relies solely on the phase information.

7.2.4 Development of Buried Pipelines Leaks Detection and Localization Technique in 3D Multistatic SAR

Another contribution of this dissertation is the development of a technique for detection and localization of buried pipeline leaks. Because the pipelines are extended targets with multiple SPCs, compared to pipeline leaks that tend to be localized, the pipeline contribution to the radar response tends to be larger, preventing leak detection. To overcome this issue, the technique uses the generalized-pencil-of-function (GPOF) procedure to decompose the radar response into a collection of exponential terms with varying phases. Using the pipelines focusing algorithm, the exponent related to the pipeline in the radar response is identified and eliminated. After the elimination, a BP projection algorithm is used to define a 1D leak indicator function that is easy to interpret. The leak indicator function is shown to lead to successful leak detection and localization after the elimination of the pipeline contribution to the radar response. The technique was tested on numerous full-wave simulations of crude oil leaks as well as measured data for a water leak out of PVC as well as metallic pipelines, demonstrating the technique's effectiveness.

7.2.5 Development of Array Null-synthesis Based Tx-Rx Signal Leakage Suppression Technique for 3D Multistatic SAR

The last contribution of this dissertation is the development of a technique to reduce the Tx-Rx signal leakage which tends to be very strong, thereby hindering the radar's ability to detect weak buried-target signals. The technique takes advantage of the multiple Rx samples obtained for SAR to create two-element arrays using adjacent Rx samples in the processing stage. The two elements phases and amplitudes are adjusted to create a null along the Tx direction, leading to the suppression of the signal leakage. Along with the technique, the dissertation proposes a modified version of the BP imaging algorithm that is suitable to the two-elements arrays data. The leakage suppression and imaging performance are tested using full-wave simulation data and measurements, demonstrating their effectiveness.

7.3 Future Work

Based on this dissertation work, the following are suggestions for future studies:

7.3.1 Applying Machine Learning Based Classifiers to the Fast Full-Wave Simulation Data

The proposed fast full-wave simulation method can be used to generate large data sets of scattered fields for various buried targets in various soil media. The generated data can then be used to train machine learning based classifiers, such as neural networks, to provide automatic, robust and fast detection and identification of buried targets in 3D multistatic subsurface SAR configuration.

7.3.2 Generalizing the Pipelines Detection and Localization Algorithm for Stratified Media

In the present study, the derivation of the phase compensation (focusing) based pipelines detection and localization algorithm approximates the soil as a homogeneous medium. This approximation leads to a quick closed-form analytical formula for finding the scattering phase centers of the pipeline. Soil media in reality are better modeled as stratified media where the dielectric constant changes as a function of depth. The pipelines' conic propagation phenomena that is the base for finding the scattering phase centers is expected to be the same for stratified media, but the propagation cone will undergo refraction at each layer, making it challenging to find a closed-form solution to the location of the scattering phase center. Instead, a ray tracing procedure may be adopted to find the scattering phase center, which leads to specular reflection and satisfies Snell's law at each layer interface. When the SPCs are found, the phase can be computed based on the rays path to focus the collected signals by the SAR, leading to detection and localization of buried pipelines in stratified media.

7.3.3 Detection and Localization of Closely-Spaced Pipelines Leaks

Lastly, the leak detection technique discussed in Chapter 5 assumed a single pipeline when estimating and eliminating the pipeline contribution to the radar response. In some scenarios, there might be multiple closely-spaced buried pipelines. In such a situation, the GPOF procedure may not work well in estimating the pipelines' contributions. Instead, the forward-scattering model developed in Chapter 4 for multiple closely-spaced pipelines can be used to estimate and eliminate the pipelines' contribution to the radar response, leading to better performance in leak detection.

APPENDIX A

MATLAB Code for Focusing Based Pipelines Detection and Localization Algorithm

The main code and the function that calculates the propagation pathlength are shown in Fig. A.1.

```
clc;clear all;

load V_Data.mat
% Load measured voltage Vmn data where V is an M x N matrix
% where M is # of frequencies and N # of Rx samples
load Rx_Locations_Data.mat
% load Rx coordinates RX where RX is an N x 3 matrix
% whose columns are the (z,y,x) Rx samples coordinates
% and rows are the Rx samples
Freq = [150:10:450] * 10^6; % Define Frequencies
C_Soil = 3 * 10^8 / sqrt(4.35 - 1i * 0.3); % Define wave speed indie soil
Lambda = C_Soil./Freq; % Find wavelength
K = 2*pi ./ Lambda; % calculate K vector which has 1 x M dimensions
D = -2:0.1:2; % Define all possible displacements and its spacing
H = -2:0.1:0; % Define all possible depths its spacing
ALPHA = 0:5:170; % Define all possible orientations its angular spacing
for alpha_i = 1 : length(ALPHA) % Loop over all possible orientations
    for d_i = 1 : length(D) % Loop over all possible displacements
        for h_i = 1 :length(H) % Loop over all possible depths
            [PATH_LENGTH] = Get_Path(RX,H(h_i),D(d_i),ALPHA(alpha_i));
            % Get the total bistatic pathlength for all Rx samples
            To_Sum = V .* exp(1i * K.' * PATH_LENGTH );
            % Compensate for the phase at all frequencies and Rx samples % (focusing)
            SEARCH(h_i,d_i,alpha_i) = abs( sum(To_Sum,'all') );
            % Do a coherent sum and Save the result in SEARCH
        end
    end
end
[M , Index] = max( SEARCH(:) ); % Find maximum value
[h_op,d_op,alpha_op] = ind2sub( size(SEARCH) ,Index);
% Get the pipeline parameters indices
[ALPHA(alpha_op),D(d_op),H(h_op)] % Display the pipeline parameters

function [PATH_LENGTH] = Get_Path(RX,h,d,alpha)
ROT_Y = [ cosd(alpha),0      ,sind(alpha); ...
    0      ,   1   ,0; ...
    -sind(alpha),     0    ,cosd(alpha)] ; % Define rotation matrix
RX_p = RX*ROT_Y; % Rotate the Rx coordinate to align them with the primed coordinates
X0 = RX_p(:,1)-d; % Shift the Rx coordinate to align them with the primed coordinates
Z0 = RX_p(:,3);
R = sqrt( h*h + d*d);
TAN = [sqrt(h^2+X0.^2)+R]./[Z0];
THETA_i = atand(TAN); % Find cone generating angle for each Rx sample
for rr=1:length(RX(:,1)) % Loop over Rx sample
    theta = THETA_i(rr);
    x0 = X0(rr);
    z0 = Z0(rr);
    Rts = sqrt( (R*cotd(theta))^2 + R^2 ); % Calculate path from the Tx to the SPC
    Rsr = sqrt( (R*cotd(theta)-z0)^2 + x0^2 + h^2 );
    % Calculate path from the SPC to the Rx
    PATH_LENGTH(rr) = Rts + Rsr ; % Sum the two paths defining the total path length
end
end
```

Figure A.1: Main MATLAB code for focusing based pipelines detection and localisation algorithm where Get-Path function is defined at the end.

APPENDIX B

MATLAB Code for Optimization Based Closely-Spaced Pipelines Detection and Localization Algorithm

The main code and is shown in Fig. B.1 and the associated functions are shown in Fig. B.2 and Fig. B.3.

```
clc;clear all;
load V_Data.mat
% Load measured voltage Vmn data where V is an M x N matrix
% where M is # of frequencies and N # of Rx samples
load Rx_Locations_Data.mat
% load Rx coordinates RX where RX is an N x 3 matrix
% whose columns are the (z,y,x) Rx samples coordinates
% and rows are the Rx samples
Freq = [150:10:450] * 10^6; % Define Frequencies
C_Soil = 3 * 10^8 / sqrt(4.35 - 1i * 0.3);% Define wave speed indie soil
Lambda = C_Soil./Freq; % Find wavelength
K = 2*pi ./ Lambda; % calculate K vector which has 1 x M dimensions
[h00,d00] = Do_Search(RX,real(K),V); dcc=round(d00,1); hcc=round(h00,1);
% Apply Basic search (focusing based) algorithm to get an initial estimate
% of pipes centroid depth and displacement
DEL = [0.01:0.05:0.4]; % Define all the spacings to loop over
best_cost = inf; % Initilize best cost
for Np=1:6 % Loop over pipelines number
    for orientation = 1 :2 % Loop over pipelines orientation
        for dl_i = 1 : length(DEL) % Loop over pipelines displacement
            if orientation==1
                D_Extent = round(0.5*(Np) * DEL(dl_i),1);
                DC = [-D_Extent:0.1:D_Extent]+dcc;
                % Define the dynamic window for the pipelines centroid search
                HC = [-DEL(dl_i):0.1:DEL(dl_i)]+hcc;
                % Define the dynamic window for the pipelines centroid search
            else
                H_Extent = round(0.5*(Np) * DEL(dl_i),1);
                HC = [-H_Extent:0.1:H_Extent]+hcc;
                % Define the dynamic window for the pipelines centroid search
                DC = [-DEL(dl_i):0.1:DEL(dl_i)]+dcc;
                % Define the dynamic window for the pipelines centroid search
            end
            for h_i = 1:length(HC)  % Loop over pipelines centroid depth
                for d_i = 1:length(DC)
                    % Loop over pipelines centroid lateral displacement
                    [D00c,H00c] = Find_DH(orientation,Np,DC(d_i),HC(h_i),  DEL(dl_i) );
                    % Find the piplines depth and displacement
                    current_cost = COST_FUNCTION(RX,V,K,D00c,H00c);
                    % Calculate the cost function
                    if current_cost<best_cost
                        best_cost = current_cost; % Save the best cost so far
                        H00=H00c; % Save the best depths
                        D00=D00c; % Save the best lateral displacements
                    end
                end
            end
        end
    end
end
D00 % Diplay piplines lateral displacemnt
H00 % Diplay piplines lateral dpths
```

Figure B.1: Main function for optimization based closely-Spaced pipelines detection and localization algorithm.

```
function [h00,d00] = Do_Search(RX,K,V)
D_S = -1:0.01:1; H_S = 0.1:0.01:2; ALPHA_S = 0;% Define Search Grid
for alpha_i = 1 : length(ALPHA_S)
    for d_i = 1 : length(D_S)
        for h_i = 1 :length(H_S)
            % Loop pver seach grid
            [PATH0,THETA_i,PATH] = ...
                Get_Paths_and_Angles( RX , D_S(d_i) , H_S(h_i) , ALPHA_S(alpha_i) );
            % Get pathlength
            To_Sum = V .* exp(1i * K.' * PATH ) ;
            % Compensate for pathlength
            SEARCH(h_i,d_i,alpha_i) = abs( sum(To_Sum,'all') );
            % Do a coherent sum and save in search

        end
    end
end
[M , xiii] = max( SEARCH(:) ); % Get maximum
[row,col,page] = ind2sub( size(SEARCH) ,xiii); % convert index
h00 = H_S(row); d00 = D_S(col); % Save initial estimate
end
%%%%%%%%%%%%%%%%%%%%%%%%%%%%%%%%%%%%%%%%%%%%%%%%%%%%%%%%%%%%%%%%%%%%%%%%%%%%%%%
function [Cost] = COST_FUNCTION(RX,VALL,K,D,H)
for fii=1:length(K) % Loop over frequencies
    V = VALL(fii,:); % choose volatge at specific frequency
    k = K(fii); % choose wavenumber
    VV = 0 * V;
    for ii = 1 : length(D) % loop over all pipes
        d0 = D(ii);
        h0 = H(ii);
        [PATH0,THETA_i,PATH] = Get_Paths_and_Angles(RX,d0,h0,0);
        P_Tx = 1i * sind(THETA_i'); % find Tx rad pattern (for a H dipole)
        P_Rx = 1i * sind(THETA_i'); % find Rx rad pattern (for a H dipole)
        V0 = P_Tx .* P_Rx .* (1./PATH0) .* exp(-1i*k*PATH) ; % Obtain forward model
        VV = VV + V0 ; % sum across piplines
    end
    VV = VV * max(abs(V(:))) /max(abs(VV(:)));
    % Normlization to bring signlas to the same level
    RES0(fii) = sum(abs(VV-V));
    % Take the differance between forward model and voltage data
    % and sum across frequencies
end
Cost = ( sum(RES0) ); % summ the cost over frequncies
end
```

Figure B.2: Associated functions to the main function for optimization based closely-Spaced pipelines detection and localization algorithm.

```
function [PATH0,THETA_i,PATH] = Get_Paths_and_Angles(RX,D,H,PHI)
for pp = 1:length(PHI)
    phi = PHI(pp)+0;
    for hh = 1:length(H)
        for dd = 1:length(D)
            h = H(hh);
            d0 = D(dd);
            search = 0 ;
            ROT_Y = [ cosd(phi),0      ,sind(phi); ...
                0      ,   1   ,0; ...
                -sind(phi),     0    ,cosd(phi)] ; % Define rotation matrix
            RX_p = RX*ROT_Y;
            % Rotate the Rx coordinate to align them with the primed coordinates
            X0 = RX_p(:,1)-d0;
            % Shift the Rx coordinate to align them with the primed coordinates
            Z0 = RX_p(:,3) ;
            R = sqrt( h*h + d0*d0);
            TAN = [sqrt(h^2+X0.^2)+R]./[Z0];
            THETA_i = atand(TAN);
            % Find cone generating angle for each Rx sample
            for rr=1:length(RX(:,1)) % Loop over Rx sample
                theta = THETA_i(rr);
                x0 = X0(rr);
                z0 = Z0(rr);
                Rts = sqrt( (R*cotd(theta))^2 + R^2 );
                % Calculate path from the Tx to the SPC
                Rsr = sqrt( (R*cotd(theta)-z0)^2 + x0^2 + h^2 );
                % Calculate path from the SPC to the Rx
                PATH(rr) = Rts + Rsr ; % Calculate propagation path
                PATH0(rr) = Rts * Rsr ; % Calculate attenuation path
            end
        end
    end
end
end

%%%%%%%%%%%%%%%%%%%%%%%%%%%%%%%%%%%%%%%%%%%%%%%%%%%%%%%%%%%%%%%%%%%%%%%%%%%%%%%

function [D0,H0] = Find_DH(ORIENT_i,Np,D_Center,H_Center,Delta)
% This function onverts from a collection of pipelines parameters to
% individual pipelines parameters
if ORIENT_i==1
    D0 = linspace( (-(Np-1)/2 )*Delta , ((Np-1)/2 )*Delta , Np ) + D_Center;
    H0 = H_Center * ones(1,Np);
else
    H0 = linspace( (-(Np-1)/2 )*Delta , ((Np-1)/2 )*Delta , Np ) + H_Center;
    D0 = D_Center * ones(1,Np);
end
end
```

Figure B.3: Associated functions to the main function for optimization based closely-Spaced pipelines detection and localization algorithm.

APPENDIX C

MATLAB Code for Signal Leakage Cancellation

The main code and is shown in Fig. C.1 and the associated array imaging function is shown in Fig. C.2

```
clc;clear all
load V1_Data.mat
% Load measured voltage for Scan1 Vmn data where V is an M x N matrix
% where M is # of frequencies and N # of Rx samples
load Rx_Locations_Data.mat
% load Rx coordinates RX where RX is an N x 3 matrix
% whose columns are the (z,y,x) Rx samples coordinates
% and rows are the Rx samples
dd=0; % Define the location of the Tx w.r.t the global coordinates
S1=IMAGING_Array(VOC,RX,dd,1); % Do imaging for Scan1 without null-steering
S10=IMAGING_Array(VOC,RX,dd,0);%Do imaging for Scan1 with null-steering
% Do the same for Scan2
load V2_Data.mat
load Rx_Locations_Data.mat
dd=0.4;
S2 = IMAGING_Array(VOC,RX,dd,1);
S20 = IMAGING_Array(VOC,RX,dd,0);
% Do the same for Scan3
load V3_Data.mat
load Rx_Locations_Data.mat
dd=1;
S3 = IMAGING_Array(VOC,RX,dd,1);
S30 = IMAGING_Array(VOC,RX,dd,0);

S = abs(S1)/max(abs(S1(:))) +... % combine the 3 Scans images
    abs(S2)/max(abs(S2(:)))+ abs(S3)/max(abs(S3(:)));
S0 = abs(S10)/max(abs(S1(:)))+ ... % combine the 3 Scans images
    abs(S20)/max(abs(S2(:)))+ abs(S30)/max(abs(S3(:)));
Sm = S / max(abs(S(:)));Sm0 = S0 / max(abs(S(:))); % normlize image
SS = 20*log10(abs(Sm) );SS0 = 20*log10(abs(Sm0) ); % convert to dB
% Plot No null-steering imaging results
[X, Z]=meshgrid(-2:0.025:2,0:-0.025:-1);
h = figure('Renderer', 'painters', 'Position', [0 0 500 200])
surf(X,Z,SS,SS);nameX = xlabel('{x [m]}','fontsize',16)
set(nameX,'Interpreter','latex');title('Without Null-Steering')
nameY = ylabel('{z [m]}','fontsize',16)
set(nameY,'Interpreter','latex');
view(0,90)
shading interp
colormap(parula);colorbar('EastOutside');xlim([X(1), X(end)])
ylim([Z(end), Z(1)]);caxis([-10 -0]);set(gca,'YTick',-1:0.2:0)
set(gca,'XTick',-2:0.5:2);box on;grid off;hold on
plot3(0,-0.32,1,'ok','MarkerSize',20,'linewidth',2)
plot3(1,-0.32,1,'ok','MarkerSize',20,'linewidth',2)

% Plot null-steering imaging results
h = figure('Renderer', 'painters', 'Position', [0 0 500 200])
surf(X,Z,SS0,SS0);nameX = xlabel('{x [m]}','fontsize',16)
set(nameX,'Interpreter','latex');;title('With Null-Steering')
nameY = ylabel('{z [m]}','fontsize',16)
set(nameY,'Interpreter','latex');view(0,90);shading interp;colormap(parula)
colorbar('EastOutside');xlim([X(1), X(end)]);ylim([Z(end), Z(1)])
caxis([-19 -9]);set(gca,'YTick',-1:0.2:0);set(gca,'XTick',-2:0.5:2)
box on;grid off;hold on;plot3(0,-0.32,1,'ok','MarkerSize',20,'linewidth',2)
plot3(1,-0.32,1,'ok','MarkerSize',20,'linewidth',2)
```

Figure C.1: Main function for signal leakage cancellation and imaging algorithm, the array imaging function is shown in Fig. C.2.

```
function S = IMAGING_Array(VOC,RX,dd,NoARRAY)
er = 6 ; % define soil relative dielectric
RX(:,1) = RX(:,1) + dd ;indx=1; % convert Rx positions to global coord
for ii=1:1:length(RX)-1 %Loop over RXs to form two-element arrays
    V(:,indx) = -VOC(:,ii+1) + VOC(:,ii); % Form the two-element array
    R1(indx,:) = RX(ii,:); % save first array element location
    R2(indx,:) = RX(ii+1,:); % save second array element location
    indx = indx + 1;
end
if NoARRAY VOC = VOC; RX1 = RX; RX2 = RX;
    % if no array, use individual Rx positions
else    VOC = V; RX1 = R1;  RX2 = R2;end
% if array, use array Rx positions
[X, Z]=meshgrid(-2:0.025:2,0:-0.025:-1); Y = 0 * ones(size(X)) ;
% Define imaging grid
S=zeros(size(X)); Freq = [100:10:500] * 10^6 ; f=[]; data=[];
TX=[dd, 0, 0.05]; % define frequncies and Tx position

RXxs1 = RX1(:,1);RXys1 = RX1(:,2);RXzs1 = RX1(:,3);
RXxs2 = RX2(:,1);RXys2 = RX2(:,2);RXzs2 = RX2(:,3);
RXx1=[];RXy1=[];RXz1=[];
RXx2=[];RXy2=[];RXz2=[];
for nn=1:1:length(RXxs1) % Fill Rx data for imaging
    temp = Freq;temp = temp';f=[f; temp];data=[data; ( VOC(:,nn))];
    RXx1=[RXx1; RXxs1(nn)*ones(length(temp),1)];
    RXy1=[RXy1; RXys1(nn)*ones(length(temp),1)];
    RXz1=[RXz1; RXzs1(nn)*ones(length(temp),1)];
    RXx2=[RXx2; RXxs2(nn)*ones(length(temp),1)];
    RXy2=[RXy2; RXys2(nn)*ones(length(temp),1)];
    RXz2=[RXz2; RXzs2(nn)*ones(length(temp),1)];
end
Permittivity = 8.854187817e-12;Permeability = 1.256637061e-6;
lambda0=3e8./f;
for m=1:1:length(data)
    for n=1:1:numel(X)
        k1= 2*pi*f(m)*sqrt(er*Permittivity*Permeability);% find wavenumber
        Rti=sqrt((TX(1)-X(n)).^2+(TX(2)-Y(n)).^2+(TX(3)-Z(n)).^2);
        %Find path from Tx to  immaging point
        Rpi1=sqrt((X(n)-RXx1(m)).^2+(Y(n)-RXy1(m)).^2+(Z(n)-RXz1(m)).^2);
        %Find path from immaging point to to first array element
        Rpi2=sqrt((X(n)-RXx2(m)).^2+(Y(n)-RXy2(m)).^2+(Z(n)-RXz2(m)).^2);
        %Find path from immaging point to to second array element

        if (Rpi1-Rpi2)>0 %Keep track of sign flip in imaging
            S(n)=S(n)+data(m)*exp(j*k1*(Rti+ 0.5*[Rpi1+Rpi2] ));% Apply BP
        else
            S(n)=S(n)-data(m)*exp(j*k1*(Rti+ 0.5*[Rpi1+Rpi2] ));% Apply BP
        end
    end
end
end
```

Figure C.2: Imaging function for signal leakage cancellation and imaging algorithm. The BP imaging code is adopted from [5] and modified to incorporate array null-steering.

BIBLIOGRAPHY

[1] María García Fernández, Yuri Álvarez López, Ana Arboleya Arboleya, Borja González Valdés, Yolanda Rodríguez Vaqueiro, Fernando Las-Heras Andrés, and Antonio Pino García. Synthetic aperture radar imaging system for landmine detection using a ground penetrating radar on board a unmanned aerial vehicle. *IEEE Access*, 6:45100–45112, 2018.

[2] What you can uncover with ground penetrating radar. https://www.smeinc.com/news-events/article/what-you-can-uncover-with-ground-penetrating-radar-gpr. Accessed: 2022-09-8.

[3] Gpr technology aids in uncovering early jamestown features and burial. https://popular-archaeology.com/article/gpr-technology-aids-in-uncovering-early-jamestown-features-and-burial/. Accessed: 2022-09-8.

[4] Georadar (ground penetrating radar)l. https://www.geotech.hr/en/georadar-geotech/. Accessed: 2022-09-9.

[5] Behzad Yektakhah. *High Resolution Through-the-Wall and Subsurface Imaging Using Small Number of Transceivers on Moving Robotic Platforms*. PhD thesis, University of Michigan, 2019.

[6] AP Annan. Gpr—history, trends, and future developments. *Subsurface sensing technologies and applications*, 3(4):253–270, 2002.

[7] MAH El-Said. Geophysical prospection of underground water in the desert by means of electromagnetic interference fringes. *Proceedings of the IRE*, 44(1):24–30, 1956.

[8] Andrea Benedetto, Fabio Tosti, Luca Bianchini Ciampoli, and Fabrizio D'Amico. Gpr applications across engineering and geosciences disciplines in italy: A review. *IEEE Journal of Selected Topics in Applied Earth Observations and Remote Sensing*, 9(7):2952–2965, 2016.

[9] Fabrizio Terenzio Gizzi and Giovanni Leucci. Global research patterns on ground penetrating radar (gpr). *Surveys in Geophysics*, 39(6):1039–1068, 2018.

[10] Fikadu T. Dagefu and Kamal Sarabandi. High-resolution subsurface imaging of deeply submerged targets based on distributed near-ground sensors. *IEEE Transactions on Geoscience and Remote Sensing*, 52(2):1089–1098, 2014.

[11] David J Daniels. *Ground penetrating radar*, volume 1. Iet, 2004.

[12] LP Peters, Jeffrey J Daniels, and Jonathan D Young. Ground penetrating radar as a subsurface environmental sensing tool. *Proceedings of the IEEE*, 82(12):1802–1822, 1994.

[13] Paul D Gader, Miroslaw Mystkowski, and Yunxin Zhao. Landmine detection with ground penetrating radar using hidden markov models. *IEEE Transactions on Geoscience and Remote Sensing*, 39(6):1231–1244, 2001.

[14] Ying Liu and Li-Xin Guo. Fdtd investigation on gpr detecting of underground subsurface layers and buried objects. In *2016 IEEE MTT-S International Conference on Numerical Electromagnetic and Multiphysics Modeling and Optimization (NEMO)*, pages 1–2. IEEE, 2016.

[15] Angel Ribalta. Time-domain reconstruction algorithms for fmcw-sar. *IEEE Geoscience and Remote Sensing Letters*, 8(3):396–400, 2010.

[16] Behzad Yektakhah and Kamal Sarabandi. All-directions through-the-wall radar imaging using a small number of moving transceivers. *IEEE Transactions on Geoscience and Remote Sensing*, 54(11):6415–6428, 2016.

[17] Jose Angel Martinez-Lorenzo, Carey M Rappaport, and Fernando Quivira. Physical limitations on detecting tunnels using underground-focusing spotlight synthetic aperture radar. *IEEE Transactions on Geoscience and Remote Sensing*, 49(1):65–70, 2010.

[18] Behzad Yektakhah, Kamal Sarabandi, and Hussein Nasser Shaman. High resolution subsurface 3d sar imaging using robotic bi-static transceivers. In *2019 IEEE International Symposium on Antennas and Propagation and USNC-URSI Radio Science Meeting*, pages 825–826. IEEE, 2019.

[19] Tao Zeng, Cheng Hu, Hanwei Sun, and Erxue Chen. A novel rapid sar simulator based on equivalent scatterers for three-dimensional forest canopies. *IEEE Transactions on Geoscience and Remote Sensing*, 52(9):5243–5255, 2013.

[20] Krzysztof S Kulpa, Piotr Samczyński, Mateusz Malanowski, Artur Gromek, Damian Gromek, Wojciech Gwarek, B Salski, and Grzegorz Tański. An advanced sar simulator of three-dimensional structures combining geometrical optics and full-wave electromagnetic methods. *IEEE Transactions on Geoscience and Remote Sensing*, 52(1):776–784, 2013.

[21] Fan Zhang, Chen Hu, Wei Li, Wei Hu, and Heng-Chao Li. Accelerating time-domain sar raw data simulation for large areas using multi-gpus. *IEEE*

Journal of Selected Topics in Applied earth Observations and Remote Sensing, 7(9):3956–3966, 2014.

[22] Fan Zhang, Xiaojie Yao, Hanyuan Tang, Qiang Yin, Yuxin Hu, and Bin Lei. Multiple mode sar raw data simulation and parallel acceleration for gaofen-3 mission. *IEEE Journal of Selected Topics in Applied Earth Observations and Remote Sensing*, 11(6):2115–2126, 2018.

[23] Kamal Sarabandi, Jihun Choi, Ali Sabet, and Kazem Sabet. Pattern and gain characterization using nonintrusive very-near-field electro-optical measurements over arbitrary closed surfaces. *IEEE Transactions on Antennas and Propagation*, 65(2):489–497, 2016.

[24] R Wang, SR Chai, YW Wei, and LX Guo. A hybrid method for the study of the mono-static scattering from the rough surface and the target above it. In *2013 Proceedings of the International Symposium on Antennas & Propagation*, volume 2, pages 1284–1287. IEEE, 2013.

[25] Dai Hao, Wang Ruilan, Jia Xichun, Zhang Wei, Li Zhiwei, and Cong Peitong. Numerical simulation method of ground-penetrating radar identification of piping based on finite-difference-time-domain method. In *2017 International Symposium on Intelligent Signal Processing and Communication Systems (ISPACS)*, pages 535–539. IEEE, 2017.

[26] Jianwei Lei, Binghan Xue, Hongyuan Fang, Yinping Li, and Man Yang. Forward analysis of gpr for underground pipes using cuda-implemented conformal symplectic euler algorithm. *IEEE Access*, 8:205590–205599, 2020.

[27] Jean Kyle Alvarez, Sheila Sutjipto, and Sarath Kodagoda. Validated ground penetrating radar simulation model for estimating rebar location in infrastructure monitoring. In *2017 12th IEEE Conference on Industrial Electronics and Applications (ICIEA)*, pages 1460–1465. IEEE, 2017.

[28] LA Varyanitza-Roshchupkina and GP Pochanin. Strategy of gpr searching for low radar contrast plastic pipes in ground. *IEEE Aerospace and Electronic Systems Magazine*, 21(12):23–26, 2006.

[29] Aleksandar Vaso Ristic, Dusan Petrovacki, and Miro Govedarica. A new method to simultaneously estimate the radius of a cylindrical object and the wave propagation velocity from gpr data. *Computers & Geosciences*, 35(8):1620–1630, 2009.

[30] Xiren Zhou, Huanhuan Chen, and Tong Hao. Efficient detection of buried plastic pipes by combining gpr and electric field methods. *IEEE Transactions on Geoscience and Remote Sensing*, 57(6):3967–3979, 2019.

[31] Giovanni Borgioli, Lorenzo Capineri, PierLuigi Falorni, Serena Matucci, and Colin G Windsor. The detection of buried pipes from time-of-flight radar data. *IEEE Transactions on Geoscience and Remote Sensing*, 46(8):2254–2266, 2008.

[32] Colin G Windsor, Lorenzo Capineri, P Falorni, et al. The estimation of buried pipe diameters by generalized hough transform of radar data. In *Proceedings Progress In Electromagnetics Research Symposium (PIERS)*, pages 22–26, 2005.

[33] Qingxu Dou, Lijun Wei, Derek R Magee, and Anthony G Cohn. Real-time hyperbola recognition and fitting in gpr data. *IEEE Transactions on Geoscience and Remote Sensing*, 55(1):51–62, 2016.

[34] Chenxi Yuan, Shuai Li, Hubo Cai, and Vineet R Kamat. Gpr signature detection and decomposition for mapping buried utilities with complex spatial configuration. *Journal of Computing in Civil Engineering*, 32(4):04018026, 2018.

[35] Hyoung-sun Youn and Chi-Chih Chen. Neural detection for buried pipes using fully-polarimetric ground penetrating radar system. In *IEEE Antennas and Propagation Society International Symposium. Digest. Held in conjunction with: USNC/CNC/URSI North American Radio Sci. Meeting (Cat. No. 03CH37450)*, volume 2, pages 231–234. IEEE, 2003.

[36] Paolo Gamba and Simone Lossani. Neural detection of pipe signatures in ground penetrating radar images. *IEEE Transactions on Geoscience and Remote Sensing*, 38(2):790–797, 2000.

[37] Minh-Tan Pham and Sébastien Lefèvre. Buried object detection from b-scan ground penetrating radar data using faster-rcnn. In *IGARSS 2018-2018 IEEE International Geoscience and Remote Sensing Symposium*, pages 6804–6807. IEEE, 2018.

[38] W Al-Nuaimy, Y Huang, M Nakhkash, MTC Fang, VT Nguyen, and A Eriksen. Automatic detection of buried utilities and solid objects with gpr using neural networks and pattern recognition. *Journal of applied Geophysics*, 43(2-4):157–165, 2000.

[39] Edoardo Pasolli, Farid Melgani, and Massimo Donelli. Automatic analysis of gpr images: A pattern-recognition approach. *IEEE Transactions on Geoscience and Remote Sensing*, 47(7):2206–2217, 2009.

[40] S Delbo, Paolo Gamba, and D Roccato. A fuzzy shell clustering approach to recognize hyperbolic signatures in subsurface radar images. *IEEE Transactions on Geoscience and Remote Sensing*, 38(3):1447–1451, 2000.

[41] Elena Pettinelli, Andrea Di Matteo, Elisabetta Mattei, Lorenzo Crocco, Francesco Soldovieri, J David Redman, and A Peter Annan. Gpr response from buried pipes: Measurement on field site and tomographic reconstructions. *IEEE Transactions on Geoscience and Remote Sensing*, 47(8):2639–2645, 2009.

[42] Francesco Soldovieri, Adriana Brancaccio, Giancarlo Prisco, Giovanni Leone, and Rocco Pierri. A kirchhoff-based shape reconstruction algorithm for the multimonostatic configuration: The realistic case of buried pipes. *IEEE Transactions on Geoscience and Remote Sensing*, 46(10):3031–3038, 2008.

[43] Rocco Pierri, Angelo Liseno, Raffaele Solimene, and Francesco Soldovieri. Beyond physical optics svd shape reconstruction of metallic cylinders. *IEEE Transactions on Antennas and Propagation*, 54(2):655–665, 2006.

[44] Marco Salucci, Lorenzo Poli, Nicola Anselmi, and Andrea Massa. Multifrequency particle swarm optimization for enhanced multiresolution gpr microwave imaging. *IEEE Transactions on Geoscience and Remote Sensing*, 55(3):1305–1317, 2016.

[45] Maryam Hajebi and Ahmad Hoorfar. A multiscale optimization technique for large-scale subsurface profiling. *IEEE Geoscience and Remote Sensing Letters*, 18(10):1706–1710, 2020.

[46] Francesco Soldovieri, Raffaele Solimene, Lorenzo Lo Monte, Massimo Bavusi, and Antonio Loperte. Sparse reconstruction from gpr data with applications to rebar detection. *IEEE transactions on instrumentation and measurement*, 60(3):1070–1079, 2010.

[47] Sebastian Hantscher and Christian G Diskus. Pulse-based radar imaging using a genetic optimization approach for echo separation. *IEEE Sensors Journal*, 9(3):271–276, 2009.

[48] Deshan Feng, Siyuan Ding, Xun Wang, and Xiangyu Wang. Wavefield reconstruction inversion of gpr data for permittivity and conductivity models in the frequency domain based on modified total variation regularization. *IEEE Transactions on Geoscience and Remote Sensing*, 60:1–14, 2021.

[49] Xun Wang and Deshan Feng. Multiparameter full-waveform inversion of 3-d on-ground gpr with a modified total variation regularization scheme. *IEEE Geoscience and Remote Sensing Letters*, 18(3):466–470, 2020.

[50] Francois Lavoué, Romain Brossier, Ludovic Métivier, Stéphane Garambois, and Jean Virieux. Two-dimensional permittivity and conductivity imaging by full waveform inversion of multioffset gpr data: A frequency-domain quasi-newton approach. *Geophysical Journal International*, 197(1):248–268, 2014.

[51] Enhedelihai Nilot, Xuan Feng, Yan Zhang, Minghe Zhang, Zejun Dong, Haoqiu Zhou, and Xuebing Zhang. Multiparameter full-waveform inversion of on-ground gpr using memoryless quasi-newton (mlqn) method. In *2018 17th International Conference on Ground Penetrating Radar (GPR)*, pages 1–4. IEEE, 2018.

[52] John H Bradford, David F Dickins, and Per Johan Brandvik. Assessing the potential to detect oil spills in and under snow using airborne ground-penetrating radar. *Geophysics*, 75(2):G1–G12, 2010.

[53] Maurizio Migliaccio, Ferdinando Nunziata, and Attilio Gambardella. On the co-polarized phase difference for oil spill observation. *International Journal of Remote Sensing*, 30(6):1587–1602, 2009.

[54] Ferdinando Nunziata, Xiaofeng Li, Maurizio Migliaccio, Antonio Montuori, and William Pichel. Metallic objects and oil spill detection with multi-polarization sar. In *2010 IEEE International Geoscience and Remote Sensing Symposium*, pages 2765–2768. IEEE, 2010.

[55] Maurizio Migliaccio, Ferdinando Nunziata, Antonio Montuori, Xiaofeng Li, and William G Pichel. A multifrequency polarimetric sar processing chain to observe oil fields in the gulf of mexico. *IEEE Transactions on Geoscience and Remote Sensing*, 49(12):4729–4737, 2011.

[56] Mansor Nakhkash and Mohammad R Mahmood-Zadeh. Water leak detection using ground penetrating radar. In *Proceedings of the Tenth International Conference on Grounds Penetrating Radar, 2004. GPR 2004.*, pages 525–528. IEEE, 2004.

[57] Wallace WL Lai, Ray KW Chang, Janet FC Sham, and K Pang. Perturbation mapping of water leak in buried water pipes via laboratory validation experiments with high-frequency ground penetrating radar (gpr). *Tunnelling and Underground Space Technology*, 52:157–167, 2016.

[58] Seung-Yeup Hyun, Yu-Sun Jo, Heon-Cheol Oh, Se-Yun Kim, and Young-Sik Kim. The laboratory scaled-down model of a ground-penetrating radar for leak detection of water pipes. *Measurement Science and Technology*, 18(9):2791, 2007.

[59] Sang-Wook Kim and Se-Yun Kim. Comparison of fmcw and pulse type ground-penetrating radar (gpr) for water leakage detection. In *Proceedings. 2005 IEEE International Geoscience and Remote Sensing Symposium, 2005. IGARSS'05.*, volume 7, pages 4596–4599. IEEE, 2005.

[60] Andrea Cataldo, Egidio De Benedetto, Giuseppe Cannazza, Giovanni Leucci, Lara De Giorgi, and Christian Demitri. Enhancement of leak detection in pipelines through time-domain reflectometry/ground penetrating radar measurements. *IET Science, Measurement & Technology*, 11(6):696–702, 2017.

[61] Lorenzo Crocco, Francesco Soldovieri, Tim Millington, and Nigel J Cassidy. Bistatic tomographic gpr imaging for incipient pipeline leakage evaluation. *Progress In Electromagnetics Research*, 101:307–321, 2010.

[62] L Crocco, G Prisco, F Soldovieri, and NJ Cassidy. Advanced forward modeling and tomographic inversion for leaking water pipes monitoring. In *2007 4th International Workshop on, Advanced Ground Penetrating Radar*, pages 127–131. IEEE, 2007.

[63] L Crocco, G Prisco, F Soldovieri, and NJ Cassidy. Early-stage leaking pipes gpr monitoring via microwave tomographic inversion. *Journal of Applied Geophysics*, 67(4):270–277, 2009.

[64] Josep Jordana, Manel Gasulla, and Ramon Pallàs-Areny. Electrical resistance tomography to detect leaks from buried pipes. *Measurement Science and Technology*, 12(8):1061, 2001.

[65] Sevket Demirci, Enes Yigit, Ismail H Eskidemir, and Caner Ozdemir. Ground penetrating radar imaging of water leaks from buried pipes based on back-projection method. *Ndt & E International*, 47:35–42, 2012.

[66] Hakan Brunzell. Detection of shallowly buried objects using impulse radar. *IEEE Transactions on Geoscience and Remote sensing*, 37(2):875–886, 1999.

[67] Lele Qu and Tianhong Yang. Investigation of air/ground reflection and antenna beamwidth for compressive sensing sfcw gpr migration imaging. *IEEE transactions on geoscience and remote sensing*, 50(8):3143–3149, 2012.

[68] Naoki Hayashi and Motoyuki Sato. f–k filter designs to suppress direct waves for bistatic ground penetrating radar. *IEEE transactions on geoscience and remote sensing*, 48(3):1433–1444, 2009.

[69] Xiangmin Wei and Ying Zhang. Interference removal for autofocusing of gpr data from rc bridge decks. *IEEE Journal of Selected Topics in Applied Earth Observations and Remote Sensing*, 8(3):1145–1151, 2015.

[70] Xiaoji Song, Deliang Xiang, Kai Zhou, and Yi Su. Improving rpca-based clutter suppression in gpr detection of antipersonnel mines. *IEEE Geoscience and Remote Sensing Letters*, 14(8):1338–1342, 2017.

[71] Li Liu, Zezhou Wu, Hang Xu, Bingjie Wang, and Jingxia Li. Gpr clutter removal based on factor group-sparse regularization. *IEEE Geoscience and Remote Sensing Letters*, 2021.

[72] Raffaele Persico and Francesco Soldovieri. A microwave tomography approach for a differential configuration in gpr prospecting. *IEEE transactions on antennas and propagation*, 54(11):3541–3548, 2006.

[73] Levent Gurel and Ugur Oguz. Optimization of the transmitter-receiver separation in the ground-penetrating radar. *IEEE Transactions on Antennas and Propagation*, 51(3):362–370, 2003.

[74] Mojtaba Dehmollaian, Michael Thiel, and Kamal Sarabandi. Through-the-wall imaging using differential sar. *IEEE transactions on geoscience and remote sensing*, 47(5):1289–1296, 2009.

[75] Behzad Yektakhah, Kamal Sarabandi, and Hatim Bukhari. High resolution subsurface imaging of buried targets using distributed robotic sensors. In *2018 IEEE International Symposium on Antennas and Propagation & USNC/URSI National Radio Science Meeting*, pages 1965–1966. IEEE, 2018.

[76] Roger F. Harrington. *Time-Harmonic Electromagnetic Fields*. McGraw-Hill, New York, NY, USA, frist edition, 1961.

[77] D.M. Pozar. *Microwave Engineering*. Wiley, fourth edition, 2011.

[78] Behzad Yektakhah, Jeffrey Chiu, Faisal Alsallum, and Kamal Sarabandi. Low-profile, low-frequency, uwb antenna for imaging of deeply buried targets. *IEEE Geoscience and Remote Sensing Letters*, 17(7):1168–1172, 2019.

[79] Constantine A Balanis. *Advanced engineering electromagnetics*. John Wiley & Sons, 1999. p.614-626.

[80] HA Ragheb and M Hamid. Scattering by n parallel conducting circular cylinders. *International Journal of Electronics Theoretical and Experimental*, 59(4):407–421, 1985.

[81] James R Wait. Scattering of a plane wave from a circular dielectric cylinder at oblique incidence. *Canadian journal of physics*, 33(5):189–195, 1955.

[82] Hashim A Yousif, Ronald E Mattis, and Kirk Kozminski. Light scattering at oblique incidence on two coaxial cylinders. *Applied optics*, 33(18):4013–4024, 1994.

[83] Hashim A Yousif and Sigurd Köhler. Scattering by two penetrable cylinders at oblique incidence. i. the analytical solution. *JOSA A*, 5(7):1085–1096, 1988.

[84] Milton Abramowitz and Irene A Stegun. *Handbook of mathematical functions with formulas, graphs, and mathematical tables*, volume 55. p.364. US Government printing office, 1964.

[85] Gian Guido Gentili and Umberto Spagnolini. Electromagnetic inversion in monostatic ground penetrating radar: Tem horn calibration and application. *IEEE Transactions on Geoscience and Remote Sensing*, 38(4):1936–1946, 2000.

[86] F.T. Ulaby and D.G. Long. *Microwave and radar and radiometric remote sensing*. University of Michigan Press, 2014.

[87] Kamal Sarabandi and Eric S Li. Microstrip ring resonator for soil moisture measurements. *IEEE Transactions on Geoscience and Remote Sensing*, 35(5):1223–1231, 1997.

[88] DaHan Liao and Kamal Sarabandi. Near-earth wave propagation characteristics of electric dipole in presence of vegetation or snow layer. *IEEE Transactions on Antennas and Propagation*, 53(11):3747–3756, 2005.

[89] Walter J Rawls, Donald L Brakensiek, and Norman Miller. Green-ampt infiltration parameters from soils data. *Journal of hydraulic engineering*, 109(1):62–70, 1983.

[90] Constantine A Balanis. *Antenna theory: analysis and design*. John wiley & sons, 2005. p.154.

[91] Standard pipe dimensions - archtoolbox. https://www.archtoolbox.com/standard-pipe-dimensions/. Accessed: 2022-08-28.

[92] Yingbo Hua and Tapan K Sarkar. Generalized pencil-of-function method for extracting poles of an em system from its transient response. *IEEE transactions on antennas and propagation*, 37(2):229–234, 1989.

[93] Wenjuan Zheng, Chongyang Shen, Lian-Ping Wang, and Yan Jin. An empirical soil water retention model based on probability laws for pore-size distribution. *Vadose Zone Journal*, 19(1):e20065, 2020.

[94] Joel Koplik. Creeping flow in two-dimensional networks. *Journal of Fluid Mechanics*, 119:219–247, 1982.

[95] J Koplik and TJ Lasseter. Two-phase flow in random network models of porous media. *Society of Petroleum Engineers Journal*, 25(01):89–100, 1985.

[96] Kerstin Avila, David Moxey, Alberto De Lozar, Marc Avila, Dwight Barkley, and Björn Hof. The onset of turbulence in pipe flow. *Science*, 333(6039):192–196, 2011.

[97] Cheryl J Trench. How pipelines make the oil market work–their networks, operation and regulation. *Allegro Energy Group, New York*, 2001.

[98] Steven Vogel. *Life in Moving Fluids: The Physical Biology of Flow*. Princeton University Press, p.163-172, 1981.

[99] Guoxi He, Yongtu Liang, Yansong Li, Mengyu Wu, Liying Sun, Cheng Xie, and Feng Li. A method for simulating the entire leaking process and calculating the liquid leakage volume of a damaged pressurized pipeline. *Journal of hazardous materials*, 332:19–32, 2017.

[100] Texas raw crude. https://www.texasrawcrude.com/. Accessed: 2021-08-21.

[101] Tarik Zakri, Jean-Paul Laurent, and Michel Vauclin. Theoretical evidence for-lichtenecker's mixture formulae'based on the effective medium theory. *Journal of Physics D: Applied Physics*, 31(13):1589, 1998.

[102] Kamal Sarabandi, Mark D Casciato, and Il-Suek Koh. Efficient calculation of the fields of a dipole radiating above an impedance surface. *IEEE Transactions on Antennas and Propagation*, 50(9):1222–1235, 2002.